STUDY OF THE RADIATIVE PROPERTIES OF ALIGNED CARBON NANOTUBES AND SILVER NANORODS

A Dissertation
Presented to
The Academic Faculty

by

Xiaojia Wang

In Partial Fulfillment
of the Requirements for the Degree of
Doctor of Philosophy in the
George W. Woodruff School of Mechanical Engineering

Georgia Institute of Technology
December 2011

STUDY OF THE RADIATIVE PROPERTIES OF ALIGNED CARBON NANOTUBES AND SILVER NANORODS

Approved by:

Dr. Zhuomin Zhang, Advisor
George W. Woodruff School of Mechanical Engineering
Georgia Institute of Technology

Dr. Thomas K. Gaylord
School of Electrical and Computer Engineering
Georgia Institute of Technology

Dr. Baratunde A. Cola
George W. Woodruff School of Mechanical Engineering
Georgia Institute of Technology

Dr. Yiping Zhao
Department of Physics and Astronomy, Nanoscale Science and Engineering Center
University of Georgia

Dr. Peter J. Hesketh
George W. Woodruff School of Mechanical Engineering
Georgia Institute of Technology

Date Approved: October 24, 2011

ACKNOWLEDGEMENTS

I would like to express my sincere appreciation to Dr. Zhuomin Zhang, my advisor for his support, guidance and encouragement during the entire research. This dissertation and relevant progress would not have been possible without his insightful instruction and constant help. I am also deeply grateful to all my dissertation committee members for their valuable help and support. Dr. Zhao provides AgNR samples for this study and helps me improve the modeling. The knowledge that I have learnt from Dr. Gaylord is crucial for the theoretical foundation of this dissertation. Dr. Cola has always been available for discussions of the CNT project that we collaborated. The class that I have taken with Dr. Hesketh provides constructive understanding of MEMS. In addition, I want to thank Dr. Jud Ready and Dr. Jack Flicker at GTRI for collaborating on CNT projects; Justin Abell in Dr. Zhao's group for preparing the AgNR samples; Dr. Sheng Xu for help obtain some SEM images of the samples. Also, I appreciate the financial support from the National Science Foundation and Department of Energy.

I want to thank all my group members for their kind help and support. I would like to acknowledge Drs. Bong Jae Lee, Soumyadipta Basu, and Qinghe Li for their assistance and support. I appreciate the encouragement and help from Drs. Yu-Bin Chen and Hong Ye. I enjoyed working with Liping Wang, Andrew McNamara, Trevor Bright, Jesse Watjen, and all other new coming and former group members. Besides, I am indebted to all my friends at GaTech for their friendship and support.

Finally, I want to extend my deepest appreciation to my parents. I am so grateful to possess their love, support, and patience through all these years.

TABLE OF CONTENTS

	Page
ACKNOWLEDGEMENTS	iii
LIST OF TABLES	vii
LIST OF FIGURES	viii
NOMENCLATURE	xiii
ACRONMYS	xvii
SUMMARY	xix
CHAPTER	
1 INTRODUCTION	1
1.1 Highly Absorbing Arrays of Carbon Nanotubes	2
1.2 Anisotropic Arrays of Inclined Silver Nanorods	4
1.3 Motivations and Objectives	7
2 THEORETICAL BACKGROUND	10
2.1 Radiative Property Definitions	10
2.2 Effective Medium Theory	13
2.3 Wave Propagation inside Uniaxial Media	17
2.4 Reflectance and Transmittance Coefficients at Anisotropic Interfaces	21
2.5 Thin-Film Optics for Anisotropic-Layer Structures	25
3 MEASUREMENT INSTRUMENTATION	29
3.1 Optical Laser Scatterometer	29
3.2 Integrating Sphere for DHR Measurement	33

4 HIGHLY ABSORBING CARBON NANOTUBE ARRAYS: TIP GROWTH VS. BASE GROWTH 39

4.1 Sample Fabrication and Characterization 39

4.2 Measurement Results and Discussions 46

4.2.1 Directional-Hemispherical Reflectance 46

4.2.2 Bidirectional Reflectance Distribution Function 49

4.3 Theoretical Modeling 53

4.4 Conclusion 57

5 HIGHLY ABSORBING CARBON NANOTUBE ARRAYS: SPECULAR VS. DIFFUSE 59

5.1 Sample Fabrication and Characterization 59

5.2 Measurement Results and Discussions 63

5.2.1 BRDF for Comparison of Surface Features 63

5.2.2 Directional-Hemispherical Reflectance 68

5.2.3 Angle-Resolved Specular Reflectance 71

5.3 Theoretical Modeling for Effective Optical Constants 73

5.4 Conclusion 77

6 ANGLE-RESOLVED PROPERTIES OF INCLINED SILVER NANORODS ON SILVER FILM 78

6.1 Sample Preparation and Characterization 79

6.2 Angle-Resolved Reflectance, BRDF, and DHR Measurements 82

6.3 Measurement Results and Discussion 84

6.3.1 BRDF Measurement 84

6.3.2 Specular Reflectance and DHR 87

6.4 Theoretical Modeling 89

6.4.1 Three-Layer Model for AgNR-on-Ag Film Samples 90

6.4.2 Determination of Effective Optical Constants with Fitting 93
6.4.3 Determination of Effective Optical Constants with the EMT 97
6.4 Conclusion 99
7 DIFFRACTION OF INCLINED SILVER NANORODS ON CD 100
7.1 Sample Fabrication and Characterization 100
7.1.1 Sample Fabrication by Oblique Angle Deposition 100
7.1.2 Morphology Characterization Based on SEM Images 102
7.2 Sample Loading Orientations for Measurements 105
7.3 Theoretical Modeling 107
7.3.1 Determination of the Effective Optical Constants 107
7.3.2 Rigorous Coupled-Wave Analysis 109
7.4 Results and Discussion 113
7.4.1 Diffraction Measurement 113
7.4.2 Beam Elongation Effect 115
7.4.3 Reflectance of Diffraction Peaks 118
7.4.4 DHR and the Scattering Effect 123
7.5 Conclusion 127
8 CONCLUSIONS AND FUTURE RECOMMENDATIONS 129
REFERENCES 134
VITA 146

LIST OF TABLES

		Page
Table 4.1:	Parameters of the VACNT samples used in the present study.	44
Table 4.2:	Comparison of the absorptance $\alpha = 1 - R_{dh}$ from integration of BRDF at normal incidence and from the integrating sphere measurement at λ = 635 nm.	52
Table 5.1:	Growth conditions and measured parameters for the CNT samples.	61
Table 5.2:	R_{dh} and absorptance of three samples obtained using different methods at the wavelength of 635 nm.	69
Table 6.1:	Comparison of the optical constants of the inclined AgNR array obtained from specular reflectance fitting and the EMT predictions at λ = 635 and 977 nm. The optical constants of bulk silver are taken from Palik [87]. For λ = 635 nm, the values are n = 0.135 and κ =4.01; for λ = 977 nm, the values are n = 0.206 and κ = 6.59.	96
Table 7.1:	Summary of the effective refractive indices predicted from the EMT (to be used in the RCWA modeling) for both Samples 1 and 2 with different polarizations.	113
Table 7.2:	Reflectance of diffraction peaks from TAAS measurements for both Samples 1 and 2 with different polarizations and diffraction orders.	122
Table 7.3:	Comparison of reflectance obtained from measurements and model prediction. The generalized specularity and effective roughness of Samples 1 and 2 are also listed.	124

LIST OF FIGURES

Page

Figure 2.1: Geometry for the definition of BRDF. 12

Figure 2.2: (a) Coordinate transform from global to local coordinates; (b) Directions associated with wave propagation in a uniaxial medium. The black vertical lines correspond to the constant phase front. 19

Figure 2.3: (a) Schematic of an anisotropic interface between two uniaxial media; (b) Optical axis orientation, local coordinates along principal crystal directions and global coordinates of medium 1; (c) Optical axis orientation, local coordinates along principal crystal directions and global coordinates of medium 2. 23

Figure 2.4: Configuration of the three-layer model of a uniaxial thin film on an optically semi-infinite substrate: (a) Isotropic propagation of ordinary waves corresponding to TE polarization; (b) Anisotropic propagation of extraordinary waves corresponding to TM polarization. 26

Figure 3.1: Schematic showing the experimental arrangement of the TAAS. The dashed circle represents the projection of the upper hemisphere on the goniometric table, which also indicates the sample detector movement for in-plane measurement. 31

Figure 3.2: Two photos of the TAAS for easier visualization: (a) Three movable stages; (b) The light source assembling. 32

Figure 3.3: Schematic of the IS setup for spectral and directional-hemispherical reflectance measurement with the center-mount configuration. The light source is a tungsten-halogen lamp with a broad spectrum from visible to NIR. Monochromatic light is produced by a filter wheel and monochromator. 34

Figure 3.4: A photo of the IS system showing the light source, filter wheel, monochromator, chopper, focus lenses, and the sphere. 35

Figure 3.5: Calibration of IS by comparing the measurements with theoretical calculation of the spectral and directional-hemispherical radiative properties of a bare silicon wafer. 37

Figure 4.1: Illustrations of fabrication systems: (a) A schematic of the synthesis setup; (b) A photo of the TCVD chamber, gas supply, and programmable computer controller. 41

Figure 4.2: Two growth mechanisms: (a) Root growth with metal catalyst on bottom; (b) Tip growth with metal catalyst on top. 42

Figure 4.3: SEM images: (a) Sample 5, which is tip-growth dominant with catalyst nanoparticles at VACNT tips; (b) Sample 2, which is base-growth dominant. 43

Figure 4.4: TEM image of the MWCNTs under the same growth conditions as those of the measured samples. 45

Figure 4.5: R_{dh} of six CNT samples measured with the IS in the spectral ranges from 400 to 1000 nm and from 1100 to 1800 nm. The usage of different grating and detector combinations results in the discontinuities of the curves from 1000 to 1100 nm. 48

Figure 4.6: BRDF measurements of Sample 1 (a,b) and Sample 4 (c,d) at different incidence angles for both *s* polarization (left) and *p* polarization (right). The inset of Fig. 4.6(b) shows the geometry of bidirectional reflection. 50

Figure 4.7: Schematic showing the polarization-dependent dielectric functions of (a) Single graphene sheet; (b) VACNT array. 57

Figure 4.8: Effective optical constants calculated from EMT as a function of *f* for different combination factors at λ = 536 nm: (a) Refractive index; (b) Extinction coefficient. 55

Figure 4.9: Spectral reflectance calculated from thin-film optics using the effective optical constants calculated from EMT for different *f* and *x*. 56

Figure 5.1: (a) Schematic of the VACNT sample fabrication procedures; (b) A photo of the Axitron Black Magic system. 60

Figure 5.2: Representative SEM images: (a) Side view of Sample 1 for top region; (b) Side view of Sample 1 for middle region; (c) Side view of Sample 1 for the entire region; (d) Inclined view of Sample 1 whose side is well aligned and top is relatively smooth; (e) Inclined view of Sample 2 whose surface is less smooth. The scale bars correspond to different magnifications. The lower right corner shows two photos of Samples 1 and 2, respectively. 62

Figure 5.3: BRDFs measured at the 635-nm wavelength for all three samples at incidence angles of 0^o, 30^o, and 60^o. In the plots, "s-pol" and "p-pol" represent *s* polarization and *p* polarization, respectively. The specular peaks at normal incidence are obtained by shifting the measured BRDF at 4^o incidence angle. 66

Figure 5.4: Comparison of specular blacks: (a) Lord/Z302 from Snail's work (highlighted with blue curves); (b) Specular CNT array of Sample 1 (blue curves with hollow circle markers). The BRDF plots are for *s* polarization. The incident wavelengths are 632.8 nm and 635 nm for

Lord/Z302 and Sample 1, respectively; and the incidence angles are $\theta_i = 5^o$ and normal incidence for Lord/Z302 and Sample 1, respectively. 67

Figure 5.5: Spectral DHR measured using the integrating sphere with center-mount configuration (curves) and back-mount configuration (markers). The sample was cut to about 18×18 mm^2 in size to compensate the difference in the sample signal and background signal. The error bars represent an expended uncertainty of 30%. 70

Figure 5.6: Specular reflectance measurements with the TAAS at the wavelength of 635 nm and at various incidence angles: (a) Sample 1 with the most specular surface; (b) Sample 2 with a less specular surface. 72

Figure 5.7: Measured and calculated (with best fitted parameters) specular reflectance versus incidence angle for both polarizations. The Brewster angle is around 44^o, which is less than 45^o as the lower limit of incidence from air to an optically isotropic medium. 75

Figure 6.1: Schematic of the OAD setup. 80

Figure 6.2: SEM images of the AgNRs: (a) Top view; (b) Side view showing the oblique alignment. The tilting angle is estimated to be $\beta = 70 \pm 6°$ from substrate surface normal. The average length and diameter are L = 1550 ± 350 nm and D = 100 ± 30 nm, respectively. 81

Figure 6.3: Schematic of the sample loading orientations: (a) Orientation 1 corresponds to the case when the optical axis of AgNR array lies in plane of incidence; (b) Orientation 2 corresponds to the case when the sample loaded with Orientation 1 is counterclockwise rotated along the z-axis by 90^o. 83

Figure 6.4: Measured BRDFs of the AgNR array at the wavelengths of 635 and 977 nm for both polarizations. AgNRs tilt to the negative x-axis for Orientation 1 and are projected to the positive y-axis for Orientation 2. 85

Figure 6.5: Angle-resolved specular reflectance measured for both polarizations with Orientation 1: (a) λ = 635 nm; (b) λ = 977 nm. Note that s or p polarization corresponds to ordinary or extraordinary wave propagation in the AgNR layer. 88

Figure 6.6: Schematic of wave propagation inside a three-layer system with the middle layer being uniaxial: (a) A three-layer system; (b) A prolate-spheroid-shaped AgNR; (c) Wave propagation in the three-layer system, showing the wavevector in each layer, and the reflectance and transmittance coefficients at each interface. 91

Figure 6.7: Comparison of the specular reflectance measured from TAAS and that calculated with the best fitted parameters. In the calculation, the thickness of AgNR array is fixed at 530 nm based on L = 1550 nm and $\beta = 70^{o}$. The best fitted optical constants for both polarizations and wavelengths are summarized in Table 6.1. 94

Figure 7.1: (a) Locations of Samples 1 and 2 with respect to the CD substrate (not to scale); cartoons showing the cross-sectional profiles of the effective grating formed by AgNRs: (b) Sample 1; (c) Sample 2. 100

Figure 7.2: SEM images presenting the sample morphologies for sample characterization: (a) Bare CD gratings with a period around 1.5 μm; (b)–(d) Sample 1 with AgNRs perpendicular to CD gratings; (e)–(g) Sample 2 with AgNRs parallel to CD gratings. Images (b), (c), and (d) are rotated by 90 degrees (counterclockwise with respect to the original position). The red triangle in Fig. 6.2(g) indicates the directions of incoming vapor, its normal component, and the CD gratings. 104

Figure 7.3: Sample loading orientations for both the diffraction and diffuse component measurements with TAAS. The CD gratings are along *y*-axis for both samples and incident light is along negative *z*-axis. The POI is the *x*-*z* plane. 105

Figure 7.4: IS setup with back-mount configuration for DHR measurements of the AgNR-on-CD samples. 106

Figure 7.5: (a) Division of the triangular grating into multiple rectangular slices parallel to the substrate surface for implementation of RCWA; (b) Effective grating Sample 1; (c) Effective grating of Sample 2. Geometric parameters are L = 1200 nm, a = 900 nm, b = 600 nm, h_{Au} = 50 nm, h_{CD} = 100 nm, $\beta = 70^{o}$, and $h_{\mathrm{AgNR}} = L \times \cos\beta$ = 410 nm. 111

Figure 7.6: (a) Schematic of sample loading orientation: AgNRs tilting towards positive *x*-axis for Sample 1 and tilting towards negative *y*-axis for Sample 2. Incident beam is along the negative *z*-axis. TE (or TM) incidence corresponds to **E** or **H** being perpendicular to the POI (*x*-*z* plane). CD gratings are curved and along the *y*-axis; (b) The diffraction order is positive for negative *x*-axis and negative for positive *x*-axis. m = 0 diffraction peak is in the retroreflection direction. 114

Figure 7.7: Photographs of diffraction peaks of Sample 1 with TM incidence indicating the elongation effect. The smallest dimension of the scale bar on the target plate is 5 mm. 116

Figure 7.8: Schematic showing the beam elongation effect: (a) Approximation of curved and continuous CD gratings as discretized sub-gratings with different orientations; (b) Geometric parameters indicating the relationship between the vertical dimensions of diffraction beam spots and the diffraction angles. 117

Figure 7.9: Illustration of the sample detector movement for the adding-up method. 118

Figure 7.10: Plots of diffraction peak measurements and theoretical calculation using RCWA of Sample 1 at the 635-nm wavelength: (a) TE incidence; (b) TM incidence. 120

Figure 7.11: Plots of diffraction peak measurements and theoretical calculation using RCWA of Sample 2 at the 635-nm wavelength: (a) TE incidence; (b) TM incidence. 121

Figure 7.12: (BRDF measurements with TAAS: (a) Sample 1, TE polarization; (b) Sample 1, TM polarization; (c) Sample 2, TE polarization; (d) Sample 2, TM polarization. Five azimuthal angles were measured with the polar angle varying from 3^{o} to 80^{o} for each φ value. Note the plots for $\varphi = 0^{o}$ (black solid dots) and 180^{o} (red hollow diamonds) are discontinuous at locations where θ_r is close to θ_m for $m = \pm 1$ and ± 2 due to the diffraction peaks. The measurements indicate a fairly isotropic distribution of the diffuse component (scattering). 127

NOMENCLATURE

B	magnetic induction, $\mathrm{Wb/m^2}$
C	compensation constant for BRDF measurement
C_{sp}	specularity
c	speed of light in vacuum, 2.998×10^8 m/s
c	(effective) optical axis
D	average diameter of carbon nanotubes, m
D	electric displacement, $\mathrm{C/m^2}$
d	layer thickness or laser spot diameter, m
dL_r	reflected radiance (intensity), $\mathrm{W/(m^2 \cdot sr)}$
E	electric field vector, V/m
e	eccentricity of the ellipsoid as an approximation of nanorods
f	volume filling fraction
f_r	bidirectional reflectance distribution function, 1/sr
g	depolarization factor
H	magnetic field vector, A/m
i	$\sqrt{-1}$
j	electric current density, $\mathrm{A/m^2}$
k	wavevector, 1/m
k	magnitude of wavevector, 1/m
k_x, k_y, or k_z	x, y, or z component of wavevector, 1/m
L	average length of nanorods/nanotubes, m
L_i	incident radiance, $\mathrm{W/(m^2 \cdot sr)}$

l_m	length of the elongated diffraction spot, m
m	diffraction order
N	total number of measurement data points
n	refractive index
$\hat{n}$	vector in the normal direction to surfaces, m
R	reflectance
R_0	distance from the laser spot to the target plate, m
r_0	radius of CD grooves at the center of the laser spot, m
r, t	anisotropic reflection and transmission coefficients
s	Poynting vector, W/m^2
S	detector signal, V
T	transmittance
t	time, s
x	combination factor of two dielectric function components
x, y, z	global Cartesian coordinates upon wave propagation direction
x', y', z'	local Cartesian coordinates upon principal crystal directions
Y	surface admittance, $1/\Omega$
Z	surface impedance, Ω

Greek Symbols

α	absorptance
β	inclination angle of nanorods, rad
γ	scattering rate, rad/s
$d\Omega$	element solid angle, sr
ε	relative electric permittivity or dielectric function

$\overline{\overline{\varepsilon}}$	relative electric permittivity in tensor form
ε_0	electric permittivity of vacuum, 8.854×10^{-12} F/m
ε_∞	relative electric permittivity at high frequency
κ	extinction coefficient
Λ	grating period, m
λ	wavelength in vacuum, m
ρ_{ij}	reflectivity at an interface between media *i* and *j*
ρ_λ	spectral reflectivity at an interface
ρ_e	charge density, C/m^3
μ	relative magnetic permeability
μ_0	magnetic permeability of vacuum, $4\pi\times10^{-7}$ N/A^2
ϕ	azimuthal angle or the phase angle, rad
σ_0	DC electric conductivity, A/(V-m)
σ	surface roughness, m
$\Delta\Omega_r$	detector solid angle, sr
ω	angular frequency, rad/s
ω_p	plasma frequency, rad/s

Subscripts

1,2,3	1st, 2nd, or 3rd layer
cal	calculated results
dh	directional-hemispherical properties
diff	diffuse properties

e	general extraordinary
eff	effective properties of the nanotube/rod array
E	primary extraordinary
h	host
i	incident
i, j, k	indices used in series
meas	measured results
O	primary ordinary identical to general ordinary
p	*p* polarization
peak	diffraction peak
r	reflected
rms	root mean square
s	*s* polarization
sp	specular
x, *y*, or *z*	*x*, *y*, or *z* direction in the global Cartesian coordinate
x′, *y′*, or *z′*	*x′*, *y′*, or *z′* direction in the local Cartesian coordinates
λ	spectrally dependent properties

Superscripts

p	*p* polarization
s	*s* polarization
+	forward propagating waves
–	backward propagating waves
||	dielectric component parallel to the nanotube/rod axial direction
$\perp$	dielectric component normal to the nanotube/rod axial direction

ACRONYMS

1D	one dimensional
2D	two dimensional
3D	three dimensional
AFM	atomic force microscope
AgNR	silver nanorod
AuNR	gold nanorod
BR	Bruggeman approximation
BRDF	bidirectional reflectance distribution function, 1/sr
BSDF	bidirectional scattering distribution function, 1/sr
BTDF	bidirectional transmittance distribution function, 1/sr
CD	compact disc
DHR	directional-hemispherical reflectance
DTSG	deuterated triglycine sulfate
EMT	effective medium theory
IR	infrared
IS	integrating sphere
MG	Maxwell-Garnett
MIR	mid-infrared
MWCNT	multi-walled carbon nanotubes
NIR	near-infrared
OAD	oblique angle deposition

POI	plane of incidence
PTFE	polytetrafluoroethylene
RCWA	Rigorous Coupled Wave Analysis
RMS	root mean square
RTP	rapid thermal processing
SEM	scanning electron microscopy
SERS	surface enhanced Raman spectroscopy
SPR	surface plasmon resonance
SWCNT	single-walled carbon nanotubes
TAAS	three-axis automated scatterometer
TE	transverse electric
TCVD	thermal chemical vapor deposition
TEM	transmission electron microscopy
TM	transverse magnetic
UV	ultraviolet
VACNT	vertically aligned carbon nanotubes

SUMMARY

Arrays of nanotubes/rods made of appropriate materials can yield unique radiative properties, such as large absorption and optical anisotropy, with broad applications from high-efficiency emitters and absorbers for energy conversion to the polarization conversion via anisotropic responses. The objective of this dissertation is to investigate the radiative properties (including reflection, absorption, and scattering) of arrays formed by aligned carbon nanotubes (CNTs) and silver nanorods (AgNRs).

The CNT arrays used in the present study consist of multi-walled CNTs synthesized vertically on silicon substrates using thermal chemical vapor deposition. Their close-to-unity absorptance is demonstrated by measuring the directional-hemispherical reflectance (DHR) within the visible and near-infrared spectral ranges using an integrating sphere (IS). The bidirectional reflectance distribution function (BRDF) and angle-resolved reflectance were measured with a three-axis automated scatterometer (TAAS) at the 635-nm wavelength. The results demonstrate that high-absorptance CNT arrays may be diffusely or specularly reflecting and have important applications in radiometry. Compared with the commercially available specular blacks, the specular CNT sample investigated in this dissertation has an even higher absorptance while maintaining similar specularity. By treating the vertically aligned CNT array as an effective homogenous and uniaxial medium, the effective medium theory (EMT) is used to elucidate the mechanism of the high absorption for this high-aspect-ratio configuration. The anisotropic reflectance and transmittance coefficients are developed from the basic Maxwell equation to explain the high absorption and polarization dependence. The

effective ordinary and extraordinary optical constants of the specular CNT sample are determined by fitting the angle-resolved reflectance from theoretical prediction with those obtained from measurements.

The AgNR array used in the present study was fabricated using oblique angle deposition, which results in inclined Ag nanorods that can be modeled as an effective homogenous and optically anisotropic thin film. This AgNR thin layer has either a dielectric or metallic response for a given polarization. The spectral and directional radiative properties of AgNRs grown on different substrates, including a glass slide with a silver film and compact disc gratings, were characterized with the IS and TAAS at the 635-nm and 977-nm wavelengths for different polarizations. The results are analyzed with theoretical modeling based on the EMT, rigorous coupled-wave analysis, and anisotropic thin-film optics. The theoretical investigation not only provides a better understanding of the optically anisotropic responses of nanostructures but also allows their effective properties to be quantitatively determined, which in turn can be used to optimize the parameters of material fabrication. The results of this dissertation help gain a better understanding of the radiative properties of anisotropic nanostructures for potential applications in high-efficiency energy conversion, radiometric devices, and optical system.

CHAPTER 1

INTRODUCTION

The worldwide efforts in research activities on micro/nanostructured materials have recently led to great collections of nanostructures with readily controllable geometries and compositions. Numerous nanostructured materials exhibit fascinating radiative and optical properties that could have significant impact on the future of energy conversion [1-7], plasmonic and photonic devices [8-10], and sensing and imaging [11-16]. Examples include three-dimensionally (3D) confined nanostructures, such as quantum dots for light imaging and biochemical diagnostics, and metallic nanoparticles for plasmon absorption enhancement [17-19]; as well as two-dimensionally (2D) confined nanostructures, i.e., nanowires, nanotubes, or nanorods with high aspect ratios. The latter kind of structures, which were studied extensively since 1990s, have unique properties: the 2D confinement of their exceptional structures with cross-sections of a few nanometers and length scales upwards of several micrometers, results in the free propagation of electrons, holes, or photons along the third dimension. Arrays formed by nanowires/tubes/rods have been extensively studied and many insights have been gained on tuning their optical and radiative properties. Such structures behave as effectively homogenous media (typically with the nanowires/tubes/rods as the intrusions and surrounding medium as the host) with tunable properties adjusted through the controlling of their size and dimensions [20,21].

1.1 Highly Absorbing Arrays of Carbon Nanotubes

Among this important class of 2D confined nanostructures, carbon nanotube (CNT) arrays belong to the so-called "black" materials with extremely low reflectivity or superb high absorption [22-25]. The discovery of hollow, nanometer-size CNTs was attributed to Iijima in 1991 [26,27]. The high absorption of CNTs is partially attributed to the π band's optical transition that results in strong absorption of visible light [1] and is a typical feature for conventional carbon-based black paints. On the other hand, it is well known that the reduction of an object's refractive index to unity can eliminate its optical reflection entirely. Hence, arrays comprised of vertically aligned CNT (VACNT) with a low packing density (or volume filling fraction) can have low effective refractive indices, which not only reflect light weakly but also absorb light significantly [28]. These combined features described above makes CNT arrays, with close-to-unity absorptance, good candidates for high-efficiency absorbers or emitters for energy conversion [1,4], radiometers or bolometers for space-borne infrared systems [29,30], solar cells [3], stray light shields and detector coatings for optical and photonic devices [24,31-34], and calibration standards and backing materials for radiation measurements [25]. According to Lehman et al. [31,32], CNTs may be used as thermal-absorption coatings on pyroelectric detectors in the near-infrared (NIR) with a higher damage threshold and larger thermal conductivity as compared with conventional gold black or carbon-based paints. Recently, inorganic solar cells based on patterned CNT arrays have been reported to exhibit high efficiency for photovoltaic systems [3,35]. In addition, some research groups have demonstrated the possibility of making absorbers from CNT bundles for cryogenic bolometers [30]. Moreover, the close-to-unity absorptance and emittance of

CNTs in the NIR region with good thermal stability in an inert environment may enable their applications as superior emitters or absorbers for thermophotovoltaic systems and absolute radiometry [36].

In order to facilitate these promising applications, knowledge of the optical and radiative properties of CNTs for thermal radiation in the visible and NIR spectral regions is required. Both single-walled CNT (SWCNT) and multi-walled CNT (MWCNT) arrays have been fabricated with various techniques and their properties have been extensively studied. Lehman et al. [2,31,32] has been working on the usage of CNTs as coatings for pyroelectric detectors and high-power laser radiometers. A reasonably uniform spectral responsivity of the CNT samples in Lehman's studies was achieved in the wavelength region from visible to infrared (IR). Later, de Heer et al. [37] synthesized CNTs with either vertical or parallel alignment and measured their optical and electronic properties using an ellipsometer in the spectral range from ultraviolet (UV) to visible. Subsequently, they further [38] characterized the effective refractive index of CNT carpets by fitting the measured reflectance in the visible and NIR ranges. However, the reflectance of CNTs in their study was relatively high due to the small thicknesses, which resulted in fluctuations in the spectra due to interference of the semi-transparent CNT carpets. Yang et al. [1] recently demonstrated the absorptance of low-density MWCNT arrays can be as high as 99.95% at the incident wavelength of 633 nm by measuring the directional-hemispherical reflectance (DHR, or R_{dh}) at four visible wavelengths (478 nm, 488 nm, 514 nm, and 633 nm) and the bidirectional reflectance distribution function (BRDF) for normal incidence at λ = 633 nm. Nevertheless, the polarization of the birefringent VACNT arrays and scattering effect were not discussed in their work. Later, they further studied the VACNT

sample with extremely low reflectance of 0.0003 over a broad infrared wavelength of 3 μm < λ < 13 μm ("bandwidth limit" of the ultralow reflectivity). And they attributed the low reflectance to the unique interlocking surface of the CNT array, consisting of both a global randomness which is on the order of several hundred nanometers and a short-range randomness due to the nanotube size [39]. Mizuno et al. [4] reported a SWCNT forest with a nearly constant and near-unity absorptance of 0.98 – 0.99 across a wide spectral range from UV (200 nm) to far IR (200 μm) and they attributed the high absorption of the SWCNT forest to its sparseness and good alignment of CNTs. Besides the experimental investigations, a variety of theoretical modeling studies have also been conducted focusing on the prediction of the dielectric function of VACNT arrays on the basis of the effective medium theory (EMT). García-Vidal et al. [28,40] calculated the effective dielectric function and optical absorption of aligned dilute CNT arrays using the EMT in the UV and visible spectral regions. Wu et al. [41] modeled the optical properties of CNT arrays by implementing the EMT and a Fourier expansion method. T de los Arcos et al. [38] fitted the measured reflectance interference fringes of thin CNT arrays (either aligned or randomly orientated) on TiN substrates with the EMT prediction.

1.2 Anisotropic Arrays of Inclined Silver Nanorods

Another important type of 2D confined nanostructure is an array comprised of obliquely aligned metallic nanorods with high aspect ratio (length-to-diameter). These kinds of metallic nanorod arrays with engineered dimensions, shapes, and surrounding media have been reported to have anisotropic radiative properties and hold promise for surface enhanced Raman spectroscopy (SERS) [42-44]. The array anisotropy arises from the high-aspect-ratio structure, which forms an effectively homogenous but anisotropic

medium. Therefore, the EMT described previously can be adopted to characterize the effective radiative properties of the array depending on the incidence polarizations. Furthermore, the effective optical and radiative properties of such structures can be easily tailored by varying the geometric dimensions, such as the rod diameter, length, spacing, shape, etc. [20,45]. On the other hand, the localized surface plasmonic resonance (LSPR) effect is responsible for the enhancement of SERS of metallic nanorod arrays. The mechanism has been ascribed to either a local plasmon mode in the gap between two metallic nanorods or a multimode plasmon resonance [46].

A number of theoretical and experimental investigations of the optical and radiative properties of metallic nanorod arrays have been performed and explained with different mechanisms. In addition to the EMT [47-49], finite-difference time-domain method [50], anisotropic wave propagation in uniaxial media [51-53], and negative refraction [54-57] have been applied for studies of the metallic nanorod arrays. Among various kinds of metals, silver and gold are unparalleled for their plasmonic properties, and have relatively stable features thus, arrays formed by silver or gold nanorods (AgNR or AuNR) are good candidates for plasmonic devices [58-63] and can be used in conjugation with various biomolecules for biorelated applications [12,13]. Byun et al. [62,63] experimentally demonstrated the enhancement of SPR biosensors with AuNR gratings. Smith [49,51] theoretically studied the anisotropic wave propagation inside the uniaxial medium formed by oblique columnar thin films containing metal and voids based on the EMT. Fu et al. [47] and Mendoza-Galván et al. [52] fabricated inclined AgNR arrays and applied the EMT simulation to analyze the anisotropic spectral

responses of the AgNR samples. Pietrobon et al. [60] produced pentagonal AgNRs with tunable plamonic properties for applications in optics and functional self-assembly.

In addition, integration of multiscale micro-nano structures has gained more and more attention, some researchers have exerted tremendous efforts on exploring the potential applications of multiscale hybrid structures in various fields [18,64,65]. Chen et al. [18] fabricated AuNR gratings that can excite SPR to create optical anisotropy and enhance the emission of CdSe quantum dots. Zengraf et al. [64] reported a hybridized plasmonic waveguide design with metallic nanowires. Guo et al. [65] demonstrated direct coupling between plasmonics and photonic nanowires for nanoplasmonic circuits with less loss and subwavelength confinement. Several researchers have recently demonstrated the possibility of fabricating materials with negative refractive index by embedding a metallic nanowire array in a dielectric medium [55-57]. Podolskiy et al. [66] applied coupled-dipole equations to metallic nanowire systems in seeking of their resonance and negative responses. Jen and his collaborators [55,56] deposited thin films comprising inclined AgNRs on fused silica substrate and measured the polarization-dependent reflection and transmission coefficients in the visible regime for normal-illumination conditions. Subsequently, they extracted the effective relative permittivity and permeability of the AgNR films based on the measurement results, and concluded this nanostructure can be used for negative refraction. Menon et al. [57] demonstrated the possibility of fabricating negative index metamaterials using metal-dielectric nanocomposites for imaging applications. However, most of the studies only factor the normal incidence cases when correlating the negative index to the AgNR array properties and do not include the scattering effect.

1.3 Motivations and Objectives

For the first 2D confined nanostructure of VACNTs, most of the CNT arrays involved in pertinent studies are diffuse like, presumably due to surface roughness and inhomogeneity in the arrays. Geohegan et al. [67] performed in situ laser measurements of VACNTs, and observed a reduction of specular reflectance as time evolves due to absorption and scattering. The extremely dark VACNT arrays reported by Yang et al. [1] was Lambertian like. However, in certain applications, such as blackbody cavities for absolute radiometry, radiation thermometry, and baffle design, specular black is often preferred over diffuse black [29,34,68]. Furthermore, to better understand the effective optical constants, samples with relatively smooth surfaces are desirable. Although some conventional black paints or appliqués exhibit specular reflection [22,23], detailed studies of highly absorbing CNT arrays with specular reflection are rarely seen. Therefore, investigations of the radiative properties of VACNT arrays with surface features from diffuse to specular, and the effects of growth mechanisms to the array radiative properties are two of the major topics in this dissertation [69-71].

As has been suggested, several unique aspects of the CNT and AgNR projects which are the main topics of this dissertation are presented here: first, unlike pertinent studies based on diffuse-like CNT arrays, a highly absorbing VACNT array with specular surface is investigated. Comparisons of the VACNT array and other black materials indicate this VACNT array is more specular than any other commercially available black materials. Such specular VACNT arrays allow the determination of their surface roughness and effective optical constants through measurements and modeling. Second, a novel hybrid micro-nanoscale structure was proposed and fabricated by depositing

inclined AgNRs on top of a commercial compact disc (CD). The anisotropic diffraction features were measured and analyzed with the Rigorous Coupled-Wave Analysis (RCWA) [72-74] in seeking of related potential applications in anisotropic grating and plasmonic devices with tunable properties. Third, the formulation of reflectance and transmittance coefficients at an anisotropic interface and thin-film optics for multi-layer structures with anisotropic layers are derived from the Maxwell equations and is further modified by considering the roughness effect. Finally, a direct fitting method is proposed to determine the optical constants of the nanorod array by matching those theoretically predicted values with measurement results. Reasonable agreements are obtained on the effective optical constants from the EMT prediction and direct fitting, both of which form a major portion of the theoretical modeling of this dissertation.

The objective of this dissertation is to characterize and investigate the radiative and optical properties of anisotropic arrays comprised of highly absorbing VACNTs or inclined AgNRs, including reflectance, absorptance, transmittance, diffraction, and scattering, through both measurement and theoretical modeling. Chapter 2 presents the theoretical background necessary for subsequent chapters, including BRDF, EMT, wave propagation in anisotropic (specifically uniaxial) media, thin-film optics, and surface plasmon. Chapter 3 provides details of the general instrumentation of major equipments and measurement setups used for the studies presented in subsequent chapters. Chapter 4 describes a detailed investigation of the reflection and scattering from VACNT arrays with two growth mechanisms: tip growth and base growth. The DHR and polarization-dependent BRDFs are measured and the EMT is used to elucidate the mechanisms of the close-to-unity absorptance of the VACNT samples. Chapter 5 elucidates the radiative

properties of three VACNT samples with surface features from highly specular to diffuse synthesized on silicon substrates with different growth conditions. Their spectral reflectance and angle-resolved reflectance are characterized by an integrating sphere (IS) and a laser scatterometer, respectively. The effective optical constants of the specular VACNT array are obtained with the direct fitting method. In Chapter 6, the inclined AgNRs are grown on top of a 500-nm-thick Ag film, which strongly absorbs the visible incident light. Hence, the three-layer anisotropic wave propagation model is used to analyze the measurement results of the angle-resolved reflectance and DHR at 635-nm wavelength. The anisotropic responses to the incident polarizations (dielectric and metallic) are clearly observed. Chapter 7 discusses the anisotropic diffraction, BRDF, and scattering of two samples consisting of AgNRs deposited on CD gratings with different orientations with respect to the CD grating direction. RCWA is applied to model the diffraction efficiency of AgNR-on-CD samples with effective grating profiles. Finally, Chapter 8 summarizes the results and provides several recommendations for future research.

CHAPTER 2

THEORETICAL BACKGROUND

This chapter provides a summary of the basic theoretical background relevant to the modeling in subsequent chapters of this dissertation. Some fundamental definitions typically used for characterization of the radiative properties of a real surface, including the BRDF, DHR, and scattering, are introduced first. Then the EMT is briefly discussed for clarification of the property homogenization of the nanorod array structure and how the effective optical constants and dielectric functions are obtained with this approach. After that, the anisotropic features of wave propagation in uniaxial media are explained followed by formulations of the reflectance and transmittance coefficients at an anisotropic interface and the thin-film optics for three-layer model. Furthermore, the fundamental concepts of surface plasmons are presented for better understanding of the potential applications of AgNR arrays in photonic and plasmonic devices.

2.1 Radiative Property Definitions

When light strikes a real surface with irregularities or surface roughness, the energy is partially transmitted through the surface, specularly reflected along the specular reflection direction, and scattered in the off-specular directions. Correspondingly, the radiation redistribution from a real surface consists of a peak around the direction of specular reflection, an off-specular lobe, and a diffuse component caused by scattering. The surface roughness is a relative concept varying with incident wavelengths and angles. A rough surface appears to be smoother when the incident wavelength becomes longer,

and for a fixed wavelength, the surface tends to be more specular at larger angles of incidence.

The BRDF is a fundamental radiative property which can fully describe the energy redistribution (reflection or scattering) from a real surface at a given wavelength and widely used in thermal science [75-78]. It depends on the surface characteristics and the material refractive index and is a function of the angles of incidence and reflection (or scattering). The derivation of BRDF notation was proposed by Nicodemus et al. [79] for defining and measuring the reflectance from a surface that was neither completely specular nor perfectly diffuse. It should be noted that a more generic form is the bidirectional scattering distribution function (BSDF) which has subsets of BRDF, BTDF, BVDF for reflective, transmissive, and volume (bulk scattering) samples. For simplicity, here we use BRDF as the combined term for both reflection and scattering associated with the angles of reflection or scattering to be used. The geometry to illustrate the definition of BRDF is shown in Fig. 2.1, where the surface lies in the *x*-*y* plane and its surface normal is along the *z*-axis. In radiometric terms, the BRDF can be defined as the ratio of reflected (or scattered) radiance (intensity) to the incident irradiance (flux in watts) at a surface [76,79,80], i.e.,

$$f_{\mathrm{r}}(\lambda,\theta_{\mathrm{i}},\phi_{\mathrm{i}},\theta_{\mathrm{r}},\phi_{\mathrm{r}})=\frac{dL_{\mathrm{r}}}{L_{\mathrm{i}}\cos\theta_{\mathrm{i}}d\Omega_{\mathrm{i}}}\ (\mathrm{sr}^{-1}) \tag{2.1}$$

In Eq. (2.1), $(\theta_{\mathrm{i}},\phi_{\mathrm{i}})$ and $(\theta_{\mathrm{r}},\phi_{\mathrm{r}})$ are the polar and azimuthal angles of the incident and reflected or scattered light, respectively. L_{i} is the incident radiance within an element solid angle $d\Omega_{\mathrm{i}}$ (power per unit solid angle per unit projected source area), $L_{\mathrm{i}}\cos\theta_{\mathrm{i}}d\Omega_{\mathrm{i}}$ is the incident irradiance (power per unit projected area), and dL_{r} is the reflected or

scattered radiance. Note that both radiance and irradiance are spectral properties thus the BRDF also depends on the incident wavelength of λ.

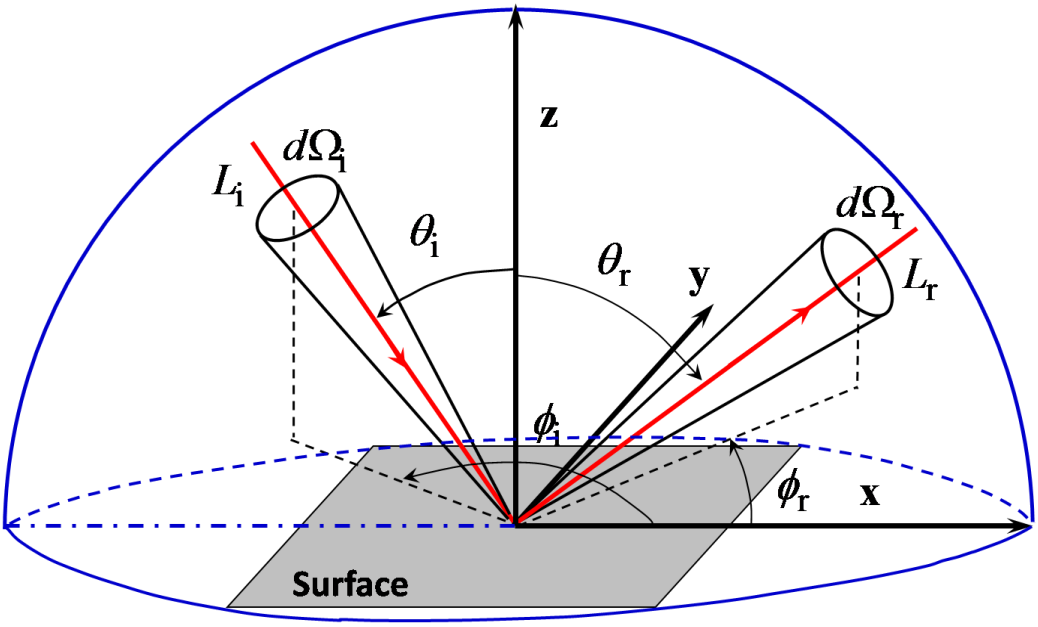

Figure 2.1 Geometry for the definition of BRDF

A special case is the BRDF in specular directions corresponding to $\theta_i = \theta_r$, which is related with specular reflectance (R_{sp}). Another important concept regarding the surface radiative properties is the directional-hemispherical reflectance (DHR or R_{dh}), which can be obtained theoretically by integrating the BRDF over the hemisphere in front of a surface, as indicated by the blue curves in Fig. 2.1. R_{dh} is the summation of R_{sp} and the diffuse component (R_{diff}) caused by scattering. In measurements, the characterization of R_{sp}, R_{dh}, and R_{diff} as the difference between the former two, are generally used to characterize the roughness. Here it should be noted that R_{diff} from a real surface might consist of both surface scattering due to surface roughness and volume (bulk) scattering due to the inhomogeneity of the material possessing that surface [81-83]. Depending on material features, R_{diff} might be dominated by either surface scattering or volume

scattering or both; for example, if the penetration depth of the material in consideration is small, then volume scattering will be less important.

2.2 Effective Medium Theory

The radiative features depend on the material properties, i.e., homogeneity versus inhomogeneity, and optical isotropy versus optical anisotropy. The VACNT arrays or inclined AgNR arrays studied in this thesis are essentially inhomogeneous since they are composites of air and nanorods. When the characteristic length of nanorod arrays is considerably small compared with the incident wavelength, the inhomogeneity effect can be neglected. Optically the material behaves as an effectively homogenous medium with the effective properties averaged over both air and nanorods. The EMT is a homogenization method widely used for characterizing the optical properties of an inhomogeneous medium with different material constituents based on the field average [84-86]. In general, two types of approximations are adopted for the EMT calculation, Maxwell Garnett (MG) and Bruggeman (BR) [85,86]. Both approximations provide expressions for the dielectric function of a homogeneous medium with properties effectively equivalent to those of the inhomogeneous medium but with different approaches. In the MG approximation, the effective properties of a composite medium are obtained by treating one constituent of the composite as the host and all other constituents as embedded grains which do not contact one another. The BR approximation equally treats all constituents as grains imbedded in an otherwise homogenous "effective" medium which is assumed to possess the average properties of the composite. The former is inherently asymmetric depending on which constituent is chosen as the host; hence it is valid for dilute systems (usually the constituent with the

highest concentration is chosen as the host). While the latter is symmetric since it treats all constituents in an equivalent way thus it is not restricted to a particular range of constituent concentrations. Following derivation based on the field average as presented in Carr et al. [84], the effective dielectric function of a multi-composite system can be expressed as

$$\frac{\varepsilon_{\text{eff}} - \varepsilon_{\text{h}}}{\varepsilon_{\text{h}} + g(\varepsilon_{\text{eff}} - \varepsilon_{\text{h}})} = \sum_{i=1}^{N} f_i \frac{\varepsilon_i - \varepsilon_{\text{h}}}{\varepsilon_{\text{h}} + g(\varepsilon_i - \varepsilon_{\text{h}})} \tag{2.2}$$

where ε_{h}, ε_i, and ε_{eff} are the dielectric functions of the host medium, the *i*-th constituent, and the effective dielectric function to be determined, respectively. g is a depolarization factor depending on the geometric and shape parameters of the composite, *N* is the number of constituents in the composite, and f_i is the volume filling ratio of the *i*-th constituent defined as the volume of the *i*-th constituent divided by the total composite volume. Note that f_i satisfies the summation rule with $\sum f_i = 1$. For the nanorod arrays with two constituents (*a* and *b*) considered in this thesis, Eq. (2.2) becomes

$$\frac{\varepsilon_{\text{eff}} - \varepsilon_{\text{h}}}{\varepsilon_{\text{h}} + g(\varepsilon_{\text{eff}} - \varepsilon_{\text{h}})} = f_a \frac{\varepsilon_a - \varepsilon_{\text{h}}}{\varepsilon_{\text{h}} + g(\varepsilon_a - \varepsilon_{\text{h}})} + (1 - f_a) \frac{\varepsilon_b - \varepsilon_{\text{h}}}{\varepsilon_{\text{h}} + g(\varepsilon_b - \varepsilon_{\text{h}})} \tag{2.3}$$

For the MG approximation, the host is one of the constituents, let us use *b* medium with $\varepsilon_{\text{h}} = \varepsilon_b$ which results in that the last term in Eq. (2.3) can be dropped

$$\frac{\varepsilon_{\text{eff}} - \varepsilon_b}{\varepsilon_b + g(\varepsilon_{\text{eff}} - \varepsilon_b)} = f_a \frac{\varepsilon_a - \varepsilon_{\text{h}}}{\varepsilon_{\text{h}} + g(\varepsilon_a - \varepsilon_{\text{h}})} \tag{2.4}$$

While for the BR approximation, the host is the effective medium with $\varepsilon_{\text{h}} = \varepsilon_b$, thus the left term drops and Eq. (2.3) can be simplified as

$$0 = f_a \frac{\varepsilon_a - \varepsilon_{\text{eff}}}{\varepsilon_{\text{eff}} + g(\varepsilon_a - \varepsilon_{\text{eff}})} + (1 - f_a) \frac{\varepsilon_b - \varepsilon_{\text{eff}}}{\varepsilon_{\text{eff}} + g(\varepsilon_b - \varepsilon_{\text{eff}})} \tag{2.5}$$

In Eqs. (2.4) and (2.5), the dielectric function of each constituent can be obtained from tabulated values in handbooks, i.e., "*Handbook of Optical Constants of Solids*" edited by Palik [87], or empirical models such as the Drude model for conductors and the Lorentz model for dielectrics. f_i can be determined by sample characterization using scanning electron microscopy (SEM) and weighing etc.. The depolarization factor g is a geometry-dependent parameter. In this study, both the CNTs and AgNRs can be treated as elongated ellipsoids with high aspect ratios, and g with the polarization along or perpendicular to the rod axial direction can be calculated as [83]:

$$g_{\text{E}} = \frac{1-e^2}{e^2}\left[\frac{1}{2e}\ln\left(\frac{1+e}{1-e}\right) - 1\right] \qquad \text{along} \tag{2.6}$$

and

$$g_{\text{O}} = \frac{1}{2}\left(1 - g_{\text{E}}\right) \qquad \text{perpendicular} \tag{2.7}$$

where $e = \sqrt{1-(D/L)^2}$ is the eccentricity determined by the average length (L) and diameter (D) of the rods. The subscripts "E" and "O" denote the extraordinary and ordinary waves propagating inside a uniaxial medium which will be discussed more in the next subsection.

The effect of the geometric depolarization factor to the radiative properties of the effective medium can be explicitly approved through a theoretical derivation of the effective dielectric function with the MG approximation. Here the BR approximation is not adopted since it is an implicit method with physically meaningful solutions to be determined through solving a quadratic equation (to be discussed more in Chapter 7). Assume that the EMT is applied to arrays formed by metallic nanorods, i.e., an effective

medium composed of air and AgNRs, whose dielectric function can be described by the Drude model

$$\varepsilon_{\mathrm{Ag}}(\omega) = \varepsilon_{\infty} - \frac{\omega_{\mathrm{p}}^2}{\omega^2 + i\omega\gamma} \tag{2.8}$$

In Eq. (2.8), ε_{∞} is the dielectric constant taking into account of the contributions other than those from the free electrons, which are significant at high frequencies. ω_{p} is the resonance frequency. The effective dielectric function predicted by the MG approximation for both ordinary and primary extraordinary waves with associated *g* is

$$\varepsilon_{\mathrm{eff}}(\omega) = 1 + \frac{f\left(\varepsilon_{\mathrm{Ag}} - 1\right)}{1 + g(1-f)(\varepsilon_{\mathrm{Ag}} - 1)} \tag{2.9}$$

Rearranging Eq. (2.9), it gives

$$\varepsilon_{\mathrm{eff}}(\omega) = \varepsilon_{\infty 1} + \frac{\omega_{\mathrm{p1}}^2}{\omega_{\mathrm{o}}^2 - \omega^2 - i\omega\gamma} \tag{2.10}$$

where

$$\varepsilon_{\infty 1} = 1 + \frac{f(\varepsilon_{\infty} - 1)}{1 + g(1-f)(\varepsilon_{\infty} - 1)} \tag{2.11}$$

and

$$\omega_{\mathrm{p1}}^2 = \frac{f}{\left(1 + g(1-f)(\varepsilon_{\infty} - 1)\right)^2}\,\omega_{\mathrm{p}}{}^2 \tag{2.12}$$

and

$$\omega_{\mathrm{o}}^2 = \frac{g(1-f)}{1 + g(1-f)(\varepsilon_{\infty} - 1)}\,\omega_{\mathrm{p}}^2 \tag{2.13}$$

Note that in the above set of equations, $\varepsilon_{\infty 1}$, ω_{p1} and ω_{o} are the effective dielectric constant, plasma frequency, and resonance frequency, respectively. Eq. (2.10) is a typical Lorentz model for dielectrics, and will be reduced to the Drude model for

metals with $\omega_0 = 0$. For infinite long nanorods, g_E = 0 and g_O = 0.5. Eq. (2.10) essentially predicts a metallic behavior of the effective medium with $\varepsilon_{\infty 1} = 1 - f + f\varepsilon_\infty$ and $\omega_{p1}^2 = f\omega_p^2$ for primary extraordinary waves and a dielectric behavior for ordinary waves as expressed by Eq. (2.10) with g_O = 0.5. However, for nanorods with finite length, even with small values of g_E, the dielectric function of metallic nanorod array with extraordinary waves is described by a Lorentz model, which predicts the metallic behavior with $\kappa \gg n$ near the resonance frequency.

2.3 Wave Propagation inside Uniaxial Media

The nanorod array can be treated as an effectively homogenous and uniaxial medium with its optical axis ($\mathbf{c}$) along the rod axial direction. Light traveling inside this medium has different responses depending on the polarization. To facilitate the understanding of wave propagation in a uniaxial medium, we present a derivation starting from the Maxwell equations to determine the wavevector magnitude inside the medium.

The Maxwell equations applicable for wave propagation inside both isotropic and anisotropic media are:

$$\nabla \bullet \mathbf{D} = \rho_e \tag{2.14a}$$

$$\nabla \bullet \mathbf{B} = 0 \tag{2.14b}$$

$$\nabla \times \mathbf{E} = -\frac{\partial \mathbf{B}}{\partial t} \tag{2.14c}$$

$$\nabla \times \mathbf{H} = \frac{\partial \mathbf{D}}{\partial t} + \mathbf{J} \tag{2.14d}$$

Related constitutive equations are:

$$\mathbf{D} = \varepsilon_0 \bar{\bar{\varepsilon}} \mathbf{E} \tag{2.15}$$

$$\mathbf{B} = \mu_0 \bar{\bar{\mu}} \mathbf{H} \tag{2.16}$$

$$\mathbf{J} = \sigma_0 \mathbf{E} \tag{2.17}$$

In those equations above, $\mathbf{E}$, $\mathbf{H}$, $\mathbf{D}$, $\mathbf{B}$, and $\mathbf{J}$ are the electric field in V/m, magnetic field in A/m, electric displacement in C/m^2, magnetic induction in Wb/m^2, and electric current density in A/m^2, respectively. ρ_e is the charge density in C/m^3 and σ_0 is the DC electric conductivity in A/(V-m). $\varepsilon_0 = 8.854\times10^{-12}$ F/m and $\mu_0 = 4\pi\times10^{-7}$ N/A^2 are the electric permittivity and magnetic permeability of free space, respectively. $\bar{\bar{\varepsilon}}$ is the relative permittivity (dielectric function) and $\bar{\bar{\mu}}$ is the relative permeability of the medium in tensor form. For a plane wave in a nonconducting, nonmagnetic, and source-free medium, $\bar{\bar{\mu}} = 1$ reduces to a scalar, and $\sigma_0 = \rho_e = 0$. Eqs. (2.14a) to (2.14d) become:

$$\mathbf{k} \times \mathbf{E} = \omega \mu_0 \mathbf{H} \tag{2.18a}$$

$$\mathbf{k} \times \mathbf{H} = -\omega \varepsilon_0 \bar{\bar{\varepsilon}} \mathbf{E} \tag{2.18b}$$

$$\mathbf{k} \bullet \bar{\bar{\varepsilon}} \mathbf{E} = 0 \tag{2.18c}$$

$$\mathbf{k} \bullet \mathbf{H} = 0 \tag{2.18d}$$

where $\mathbf{k}$ is the wavevector. The anisotropic dielectric function is a 2nd-rank tensor. The expression of $\bar{\bar{\varepsilon}}$ in a local coordinate is defined by the principal crystal directions (x', y', z') and can be expressed as

$$\bar{\bar{\varepsilon}}' = \begin{pmatrix} \varepsilon_{x'} & 0 & 0 \\ 0 & \varepsilon_{y'} & 0 \\ 0 & 0 & \tilde{\varepsilon}_{z'} \end{pmatrix} = \begin{pmatrix} \tilde{n}_{x'}^2 & 0 & 0 \\ 0 & \tilde{n}_{y'}^2 & 0 \\ 0 & 0 & \tilde{n}_{z'}^2 \end{pmatrix} \tag{2.19a}$$

For easier expression, the tilde as a notation for complex quantities is omitted in the following derivation. In general, for biaxial media with two optical axes, $\varepsilon_{x'} \neq \varepsilon_{y'} \neq \varepsilon_{z'}$. However, for the special case of uniaxial (or birefringent) media with only one optical axis along z' axis ($\mathbf{c} \| \mathbf{z}'$), the off-diagonal elements in the dielectric tensor vanish

$$\overline{\overline{\varepsilon}}' = \begin{pmatrix} \varepsilon_{x'} & 0 & 0 \\ 0 & \varepsilon_{y'} & 0 \\ 0 & 0 & \varepsilon_{z'} \end{pmatrix} = \begin{pmatrix} \varepsilon_{\mathrm{O}} & 0 & 0 \\ 0 & \varepsilon_{\mathrm{O}} & 0 \\ 0 & 0 & \varepsilon_{\mathrm{E}} \end{pmatrix} = \begin{pmatrix} n_{\mathrm{O}}^2 & 0 & 0 \\ 0 & n_{\mathrm{O}}^2 & 0 \\ 0 & 0 & n_{\mathrm{E}}^2 \end{pmatrix} \tag{2.19b}$$

where ε_{O} and ε_{E} are the principal dielectric functions and n_{O} and n_{E} are the principal indices of refraction for ordinary and extraordinary waves, respectively.

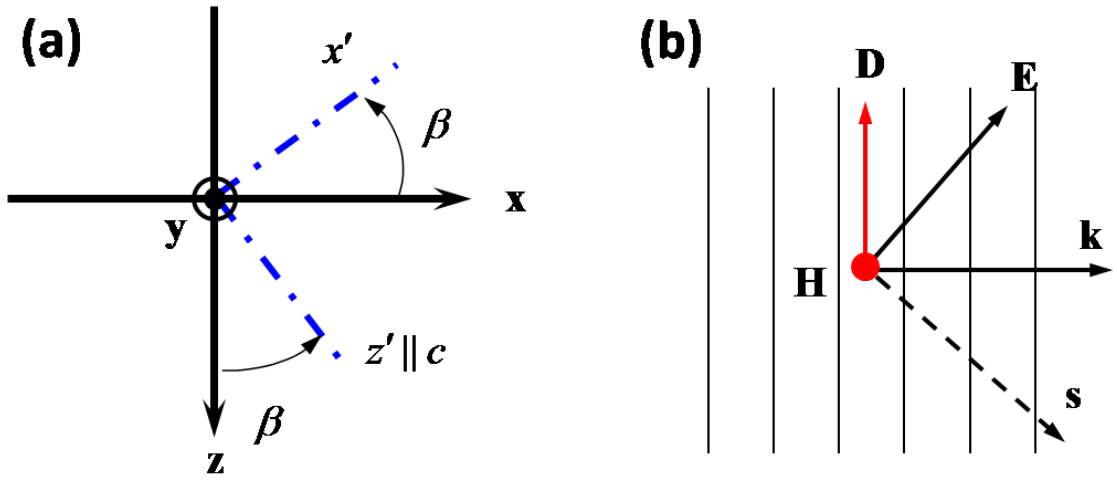

Figure 2.2 (a) Coordinate transform from global to local coordinates; (b) Directions associated with wave propagation in a uniaxial medium. The black vertical lines correspond to the constant phase front.

The dielectric tensor elements in global coordinate (x, y, z) can be expressed using the principal dielectric functions in local coordinate (x', y', z') through a coordinate transform. Ordinary waves in uniaxial media behave isotropically with n_{O} as the

refractive index; while for extraordinary waves, the refractive index varies upon propagation direction and lies in between n_O and n_E. To better understand the anisotropic features of extraordinary wave propagation, we consider a case that $\mathbf{c}$ lies in the x–z plane with the normal component of wavevector along +z axis. The angle of β between $\mathbf{c}$ and +z axis is the angle for coordinate rotation, which equals the inclination angle of nanorods, as shown in Fig. 2.2(a). In uniaxial media, $\mathbf{D}$, $\mathbf{E}$, and the wavevector $\mathbf{k}$ are coplanar, but $\mathbf{E}$ and $\mathbf{k}$ are not mutually perpendicular. While the magnetic field ($\mathbf{H}$) is always perpendicular to $\mathbf{k}$ and $\mathbf{E}$ for nonmagnetic materials; hence, the energy flow direction (denoted by the poynting vector $\mathbf{s}$, also the direction of group velocity) deviates from the phase propagation direction ($\mathbf{k}$, also the direction of phase velocity), as illustrated in Fig. 2.2(b).

For the configuration in Fig. 2.2(a), the optical-axis vector can be represented as

$$\mathbf{c} = c_x\hat{x} + c_y\hat{y} + c_z\hat{z} = \sin\beta\hat{x} + \cos\beta\hat{z} \tag{2.20}$$

The dielectric function in the global coordinates is

$$\bar{\bar{\varepsilon}} = \begin{pmatrix} \varepsilon_{xx} & \varepsilon_{xy} & \varepsilon_{xz} \\ \varepsilon_{yx} & \varepsilon_{yy} & \varepsilon_{yz} \\ \varepsilon_{zx} & \varepsilon_{zy} & \varepsilon_{zz} \end{pmatrix} \tag{2.21}$$

Then the diagonal and off-diagonal tensor elements in Eq. (2.21) can be written as:

$$\varepsilon_{ii} = n_O^2 + \left(n_E^2 - n_O^2\right)c_i^2 \tag{2.22a}$$

$$\varepsilon_{ij} = \left(n_E^2 - n_O^2\right)c_i\,c_j \tag{2.22b}$$

where i, j = x, y, and z, respectively. Note that n_O and n_E are defined in Eq. (2.19). Substitution of Eqs. (2.22a) and (2.22b) into Eq. (2.21) gives

$$\overline{\overline{\varepsilon}} = \begin{pmatrix} \varepsilon_{\mathrm{O}} \cos^2\beta + \varepsilon_{\mathrm{E}} \sin^2\beta & 0 & (\varepsilon_{\mathrm{E}} - \varepsilon_{\mathrm{O}}) \sin\beta \cos\beta \\ 0 & \varepsilon_{\mathrm{O}} & 0 \\ (\varepsilon_{\mathrm{E}} - \varepsilon_{\mathrm{O}}) \sin\beta \cos\beta & 0 & \varepsilon_{\mathrm{O}} \sin^2\beta + \varepsilon_{\mathrm{E}} \cos^2\beta \end{pmatrix} \tag{2.23}$$

Note that $\overline{\overline{\varepsilon}} = \overline{\overline{\varepsilon}}^{\mathrm{T}}$ has only 6 independent elements. Substituting Eq. (2.23) into Eq. (2.18b), the components of electric field E_x and E_z can be solved as

$$E_x = \frac{1}{\omega\varepsilon_0} \frac{k_x\varepsilon_{xz} + k_z\varepsilon_{zz}}{\varepsilon_{xx}\varepsilon_{zz} - \varepsilon_{xz}^2} H_y \tag{2.24a}$$

$$E_z = -\frac{1}{\omega\varepsilon_0} \frac{k_x\varepsilon_{xx} + k_z\varepsilon_{xz}}{\varepsilon_{xx}\varepsilon_{zz} - \varepsilon_{xz}^2} H_y \tag{2.24b}$$

Substituting the above expressions of E_x and E_z into Eq. (2.18a) gives

$$k_z^2\varepsilon_{zz} + (2k_x\varepsilon_{xz})k_z + \left[k_x^2\varepsilon_{xx} + \frac{\omega^2}{c_0^2}\left(\varepsilon_{xz}^2 - \varepsilon_{xx}\varepsilon_{zz}\right) \right] = 0 \tag{2.25}$$

This is a quadratic equation of k_z with two solutions as

$$k_z^{\pm} = \frac{-k_x\varepsilon_{xz} \pm \sqrt{(\varepsilon_{xx}\varepsilon_{zz} - \varepsilon_{xz}^2)\left(k_0^2\varepsilon_{zz} - k_x^2\right)}}{\varepsilon_{zz}} \tag{2.26}$$

Here, $k_0 = \omega/c_0$ and $\varepsilon_{xx}\varepsilon_{zz} - \varepsilon_{xz}^2 = \varepsilon_{\mathrm{O}}\varepsilon_{\mathrm{E}} = \left(n_{\mathrm{O}}n_{\mathrm{E}}\right)^2$ are used. The positive and negative square roots in Eq. (2.26) correspond to forward and backward waves, i.e., incident and transmitted waves for positive sign and reflected waves for negative sign at an interface. The tangential component of wavevector (k_x) is the same for each medium if a multi-layer structure is used due to the phase matching condition at interfaces.

2.4 Reflectance and Transmittance Coefficients at Anisotropic Interfaces

At an interface, transverse-electric polarization (TE, also called *s* polarization)

and transverse-magnetic polarization (TM, also called *p* polarization) correspond to **E** and **H** perpendicular to the plane of incidence (POI), which contains both the wavevector and surface normal ($\hat{n}$). Note that at normal incidence, there is no difference between TE and TM since $\mathbf{k} \| \hat{n}$. In general, at an interface between two anisotropic media, pure TE and TM polarizations do not exist due to the coupling between the ordinary and extraordinary waves, which means incidence with one polarization in medium 1 generates both TE and TM waves in medium 2. However, if one of the principal axes of $\bar{\bar{\varepsilon}}$ tensor for both media are normal to the POI, polarizations are decoupled. The configuration shown in Fig. 2.3 belongs to decoupling cases with the optic axes of both media ($\mathbf{c_1}$ and $\mathbf{c_2}$) lying in the POI (the *x*–*z* plane). For this configuration, ordinary and extraordinary waves correspond to the TE and TM polarizations, respectively. Ordinary waves behave similarly to waves propagating in isotropic media and satisfy the Snell law. Using the surface admittance definition stated in Ref. [88] $Y_j = H_{x,j} / E_{y,j}$ with *j* = 1 and 2 for media 1 and 2, respectively, the reflectance and transmittance coefficients at the interface between two uniaxial media for TE polarization are

$$r_{12}^{\mathrm{s}} = \frac{Y_1 - Y_2}{Y_1 + Y_2} = \frac{\sqrt{\varepsilon_{1\mathrm{O}}}\cos\theta_{\mathrm{i}} - \sqrt{\varepsilon_{2\mathrm{O}} - \varepsilon_{1\mathrm{O}}(\sin\theta_{\mathrm{i}})^2}}{\sqrt{\varepsilon_{1\mathrm{O}}}\cos\theta_{\mathrm{i}} + \sqrt{\varepsilon_{2\mathrm{O}} - \varepsilon_{1\mathrm{O}}(\sin\theta_{\mathrm{i}})^2}} \tag{2.27a}$$

and

$$t_{12}^{\mathrm{s}} = \frac{2Y_1}{Y_1 + Y_2} = \frac{2\sqrt{\varepsilon_{1\mathrm{O}}}\cos\theta_{\mathrm{i}}}{\sqrt{\varepsilon_{1\mathrm{O}}}\cos\theta_{\mathrm{i}} + \sqrt{\varepsilon_{2\mathrm{O}} - \varepsilon_{1\mathrm{O}}(\sin\theta_{\mathrm{i}})^2}} \tag{2.27b}$$

where

$$Y_1 = \frac{-\sqrt{k_0^2 n_{1\mathrm{O}}^2 - k_x^2}}{\omega\mu_0} = -\frac{k_0}{\omega\mu_0}\sqrt{\varepsilon_{1\mathrm{O}}}\cos\theta_{\mathrm{i}} \tag{2.27c}$$

and

$$Y_2 = \frac{-\sqrt{k_0^2 n_{2\mathrm{O}}^2 - k_x^2}}{\omega\mu_0} = -\frac{k_0}{\omega\mu_0}\sqrt{\varepsilon_{2\mathrm{O}} - \varepsilon_{1\mathrm{O}}(\sin\theta_{\mathrm{i}})^2} \tag{2.27d}$$

Correspondingly, the reflectance and transmittance for TE polarization are

$$R_{12}^{\mathrm{s}} = \left| r_{12}^{\mathrm{s}} \right|^2 \qquad \text{and} \qquad T_{12}^{\mathrm{s}} = \left| t_{12}^{\mathrm{s}} \right|^2 \mathrm{Re}\left(Y_2\right) / \mathrm{Re}\left(Y_1\right) \tag{2.28}$$

In Fig. 2.3(a), TM incident waves with **H** along the *y*-axis correspond to extraordinary waves only $\left(\mathbf{H} \perp \mathbf{c}\right)$. Here, the reflectance and transmittance is re-derived for extraordinary waves to facilitate the understanding of anisotropic wave propagation.

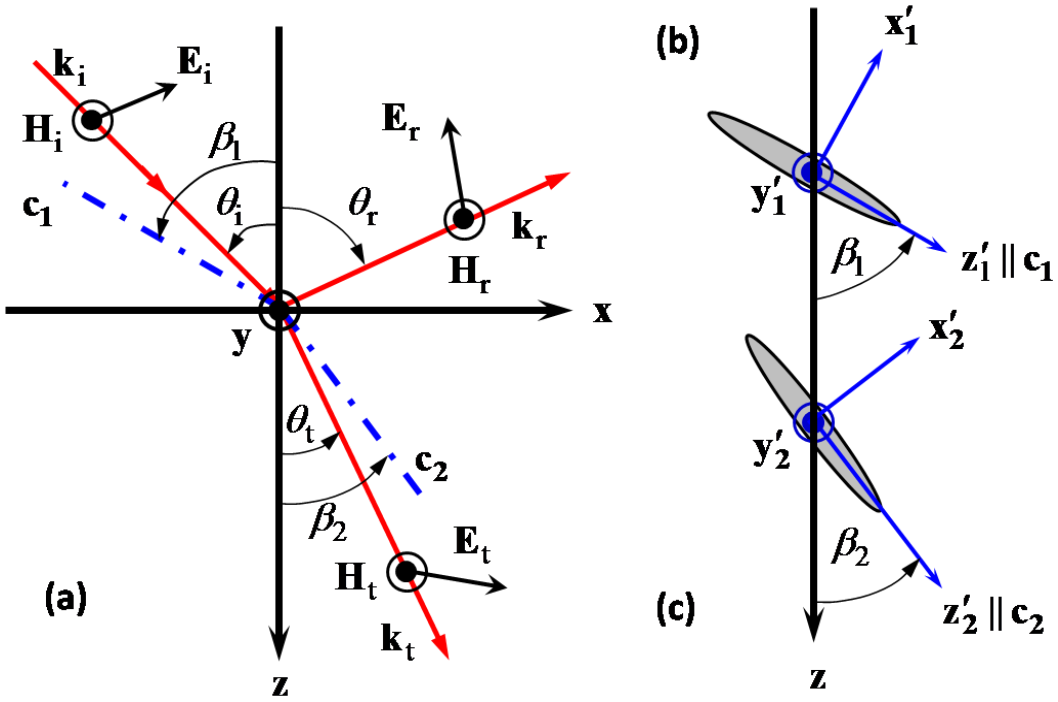

Figure 2.3 (a) Schematic of an anisotropic interface between two uniaxial media; (b) Optical axis orientation, local coordinates along principal crystal directions and global coordinates of medium 1; (c) Optical axis orientation, local coordinates along principal crystal directions and global coordinates of medium 2.

The individual wavevector and magnetic field for incidence, reflection, and transmission are

Incidence:
$$\begin{cases} \mathbf{H}_{\mathrm{i}} = H_{\mathrm{i}}\, \mathrm{e}^{\mathrm{i}k_{1x}x + \mathrm{i}k_{1z}^{+}z}\, \hat{y} \\ \mathbf{k}_{\mathrm{i}} = k_{1z}^{+}\hat{z} + k_x \hat{x} \end{cases} \tag{2.29a}$$

Reflection:
$$\begin{cases}\mathbf{H}_{\mathrm{r}} = H_{\mathrm{r}}\,\mathrm{e}^{\mathrm{i}k_{1x}x+\mathrm{i}k_{1z}^{-}z}\hat{y} \\ \mathbf{k}_{\mathrm{r}} = k_{1z}^{-}\hat{z} + k_x\hat{x}\end{cases} \tag{2.29b}$$

Transmission:
$$\begin{cases}\mathbf{H}_{\mathrm{t}} = H_{\mathrm{t}}\,\mathrm{e}^{\mathrm{i}k_{2x}x+\mathrm{i}k_{2z}^{+}z}\hat{y} \\ \mathbf{k}_{\mathrm{r}} = k_{2z}^{+}\hat{z} + k_x\hat{x}\end{cases} \tag{2.29c}$$

As mentioned before, the sign convention of k_z is positive for forward waves (incident or transmitted) and negative for backward waves (reflected), respectively. Note that in Eqs. (2.29a) to (2.29c), the time-harmonic terms of $\mathrm{e}^{-\mathrm{i}\omega t}$ are removed for convenience. Matching the tangential components of $H_y\left(z=0+\right)=H_y\left(z=0-\right)$ at the interface results in

$$\left(H_{\mathrm{i}}+H_{\mathrm{r}}\right)=H_{\mathrm{t}} \Rightarrow 1+r_{12}^{\mathrm{p}}=t_{12}^{\mathrm{p}} \tag{2.30}$$

Substituting Eqs. (2.29a) to (2.29c) into Eq. (2.18b), one can get the tangential components of the electric field of both media at the interface, whose expressions are similar to Eq. (2.24a). The continuity of the tangential components of the electric field with $E_x\left(z=0+\right)=E_x\left(z=0-\right)$ results in

$$\frac{k_x\varepsilon_{1,xz}+k_{1z}^{+}\varepsilon_{1,zz}}{\varepsilon_{1,xx}\varepsilon_{1,zz}-\varepsilon_{1,xz}^2}+\frac{k_x\varepsilon_{1,xz}+k_{1z}^{-}\varepsilon_{1,zz}}{\varepsilon_{1,xx}\varepsilon_{1,zz}-\varepsilon_{1,xz}^2}r_{12}^{\mathrm{p}}=\frac{k_x\varepsilon_{2,xz}+k_{2z}^{+}\varepsilon_{2,zz}}{\varepsilon_{2,xx}\varepsilon_{2,zz}-\varepsilon_{2,xz}^2}t_{12}^{\mathrm{p}} \tag{2.31}$$

The surface impedance $Z=E_x/H_y$ for incidence, reflection, and transmission waves are defined as

Incidence:
$$Z_1^{+}=\frac{E_{x,\mathrm{i}}}{H_{y,\mathrm{i}}}=\frac{1}{\omega\varepsilon_0}\frac{k_x\varepsilon_{1,xz}+k_{1z}^{+}\varepsilon_{1,zz}}{\varepsilon_{1,xx}\varepsilon_{1,zz}-\varepsilon_{1,xz}^2}=\frac{1}{\omega\varepsilon_0}\frac{k_x\varepsilon_{1,xz}+k_{1z}^{+}\varepsilon_{1,zz}}{\varepsilon_{1\mathrm{O}}\varepsilon_{1\mathrm{E}}} \tag{2.32a}$$

Reflection:
$$Z_1^{-}=\frac{E_{x,\mathrm{r}}}{H_{y,\mathrm{r}}}=\frac{1}{\omega\varepsilon_0}\frac{k_x\varepsilon_{1,xz}+k_{1z}^{-}\varepsilon_{1,zz}}{\varepsilon_{1,xx}\varepsilon_{1,zz}-\varepsilon_{1,xz}^2}=\frac{1}{\omega\varepsilon_0}\frac{k_x\varepsilon_{1,xz}+k_{1z}^{-}\varepsilon_{1,zz}}{\varepsilon_{1\mathrm{O}}\varepsilon_{1\mathrm{E}}} \tag{2.32b}$$

Transmission: $$Z_2^+ = \frac{E_{x,\mathrm{t}}}{H_{y,\mathrm{t}}} = \frac{1}{\omega\varepsilon_0}\frac{k_x\varepsilon_{2,xz} + k_{2z}^+\varepsilon_{2,zz}}{\varepsilon_{2,xx}\varepsilon_{2,zz} - \varepsilon_{2,xz}^2} = \frac{1}{\omega\varepsilon_0}\frac{k_x\varepsilon_{2,xz} + k_{2z}^+\varepsilon_{2,zz}}{\varepsilon_{2\mathrm{O}}\varepsilon_{2\mathrm{E}}} \tag{2.32c}$$

It is easy to see that Eq. (2.31) can be reorganized as

$$Z_1^+ + Z_1^- r_{12}^{\mathrm{p}} = Z_2^+ t_{12}^{\mathrm{p}} \tag{2.33}$$

Combining Eqs. (2.30) and (2.33) and solving for r_{12}^{p} and t_{12}^{p}, it follows that

$$r_{12}^{\mathrm{p}} = \frac{H_{\mathrm{r}}}{H_{\mathrm{i}}} = \frac{Z_1^+ - Z_2^+}{Z_2^+ - Z_1^-} \qquad \text{and} \qquad t_{12}^{\mathrm{p}} = \frac{H_{\mathrm{t}}}{H_{\mathrm{i}}} = \frac{Z_1^+ - Z_1^-}{Z_2^+ - Z_1^-} \tag{2.34}$$

Here, the positive/negative sign convention for surface impendence follows the same rules for the wavevector. $k_{1z}^{\pm}$ and $k_{2z}^{\pm}$ can be calculated using Eq. (2.26) together with related uniaxial material dielectric functions based on Eq. (2.22). Applying the conservation of power flow carried by extraordinary waves at the interface, one obtains

$$R_{12}^{\mathrm{p}} = \left|r_{12}^{\mathrm{p}}\right|^2 \qquad \text{and} \qquad T_{12}^{\mathrm{p}} = \left|t_{12}^{\mathrm{p}}\right|^2 \frac{\mathrm{Re}\left(Z_2^+\right)}{\mathrm{Re}\left(Z_1^+\right)} \tag{2.35}$$

2.5 Thin-Film Optics for Anisotropic-Layer Structures

The effective homogenous layer formed by nanorods can be treated as a semi-infinite medium if the penetration depth of the nanorod layer is much less than the layer thickness. For this case, Eqs. (2.28) and (2.35) are sufficient to characterize the radiative properties of the nanorod layer. When the layer thickness is comparable or less than the wavelength of incident radiation, the wave interference effects must be considered to correctly predict the radiative properties of multilayer structures of thin films. Here, the three-layer model of a thin film on a semi-infinite substrate is presented for better understanding of the anisotropic wave propagation in uniaxial media.

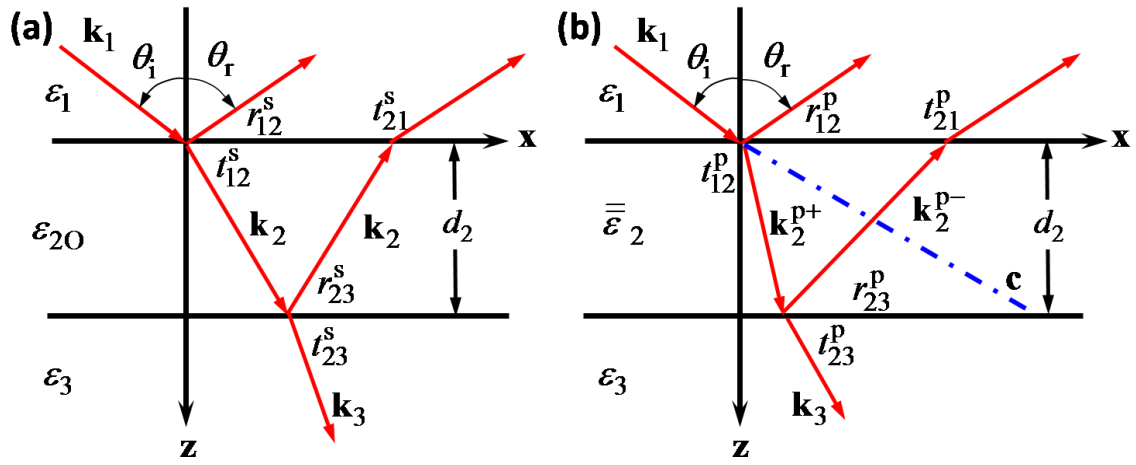

Figure 2.4 Configuration of the three-layer model of a uniaxial thin film on an optically semi-infinite substrate: (a) Isotropic propagation of ordinary waves corresponding to TE polarization; (b) Anisotropic propagation of extraordinary waves corresponding to TM polarization.

Considering light incident from a nonabsorbing and optically isotropic medium (ε_1) at an angle of θ_i to a uniaxial layer (ε_{2O} and ε_{2E}) deposited on a substrate which is optically isotropic and semi-infinite (ε_3), as indicated in Fig. 2.4. The optical axis lies in the POI (*x*-*z* plane) and the normal component of wavevector propagates along +*z* axis. For TE polarization, ordinary waves behave isotropically with n_O as the index of refraction, hence the thin-film optics formulation is similar to that of the wave propagation in an isotropic medium for TE polarization, and is summarized below:

$$Y_j = \frac{-\sqrt{k_0^2 \varepsilon_j - k_x^2}}{\omega \mu_0} = -\frac{k_0}{\omega \mu_0} \sqrt{\varepsilon_j - \varepsilon_1 (\sin \theta_i)^2} \tag{2.36}$$

where j = 1, 2O, and 3, respectively.

$$r_{ij}^s = \frac{Y_i - Y_j}{Y_i + Y_j} \quad \text{and} \quad t_{ij}^s = \frac{2Y_i}{Y_i + Y_j} \tag{2.37}$$

where i, j are two consecutive variables of the series [1, 2O, and 3].

$$r_{123}^{\mathrm{s}} = r_{12}^{\mathrm{s}} + \frac{t_{12}^{\mathrm{s}} r_{23}^{\mathrm{s}} t_{21}^{\mathrm{s}} \exp(2\phi^{\mathrm{s}}\mathrm{i})}{1 - r_{23}^{\mathrm{s}} r_{21}^{\mathrm{s}} \exp(2\phi^{\mathrm{s}}\mathrm{i})} \quad \text{and} \quad t_{123}^{\mathrm{s}} = \frac{t_{12}^{\mathrm{s}} t_{23}^{\mathrm{s}} \exp(\phi^{\mathrm{s}}\mathrm{i})}{1 - r_{23}^{\mathrm{s}} r_{21}^{\mathrm{s}} \exp(2\phi^{\mathrm{s}}\mathrm{i})} \tag{2.38}$$

where $\phi^{\mathrm{s}} = \frac{2\pi d_2}{\lambda}\sqrt{\varepsilon_{2\mathrm{O}} - \varepsilon_1(\sin\theta_{\mathrm{i}})^2}$ and d_2 is the thickness of the uniaxial layer.

$$R_{123}^{\mathrm{s}} = \left|r_{123}^{\mathrm{s}}\right|^2 \qquad \text{and} \qquad T_{123}^{\mathrm{s}} = \left|t_{123}^{\mathrm{s}}\right|^2 \frac{\mathrm{Re}\left[Y_3\right]}{\mathrm{Re}\left[Y_1\right]} \tag{2.39}$$

Notice that $k_x = k_0\sqrt{\varepsilon_1}\sin\theta_{\mathrm{i}}$ is the same for each interface due to phase matching.

For TM polarization, the calculation of reflectance and transmittance is based on surface impedance.

$$Z_j = \frac{\sqrt{k_0^2\varepsilon_j - k_x^2}}{\varepsilon_j} = \frac{k_0}{\omega\varepsilon_0}\frac{\sqrt{\varepsilon_j - \varepsilon_1(\sin\theta_{\mathrm{i}})^2}}{\varepsilon_j} \quad \text{for } j = 1 \text{ or } 3 \tag{2.40a}$$

$$Z_2 = \frac{\sqrt{k_0^2\varepsilon_{zz} - k_x^2}}{\omega\varepsilon_0 n_{2\mathrm{O}} n_{2\mathrm{E}}} = \frac{k_0}{\omega\varepsilon_0}\frac{\sqrt{\varepsilon_{zz} - \varepsilon_1(\sin\theta_{\mathrm{i}})^2}}{\sqrt{\varepsilon_{2\mathrm{O}}\varepsilon_{2\mathrm{E}}}} \tag{2.40b}$$

$$r_{ij}^{\mathrm{p}} = \frac{Z_i - Z_j}{Z_i + Z_j} \quad \text{and} \quad t_{ij}^{\mathrm{p}} = \frac{2Z_i}{Z_i + Z_j} \tag{2.41}$$

where i, j are two consecutive variables of the series [1, 2, and 3].

$$r_{123}^{\mathrm{p}} = r_{12}^{\mathrm{p}} + \frac{t_{12}^{\mathrm{p}} r_{23}^{\mathrm{p}} t_{21}^{\mathrm{p}} \exp\left[\left(\phi_+^{\mathrm{p}} - \phi_-^{\mathrm{p}}\right)\mathrm{i}\right]}{1 - r_{23}^{\mathrm{p}} r_{21}^{\mathrm{p}} \exp\left[\left(\phi_+^{\mathrm{p}} - \phi_-^{\mathrm{p}}\right)\mathrm{i}\right]} \quad \text{and} \quad t_{123}^{\mathrm{p}} = \frac{t_{12}^{\mathrm{p}} t_{23}^{\mathrm{p}} \exp\left[\left(\phi_+^{\mathrm{p}}\right)\mathrm{i}\right]}{1 - r_{23}^{\mathrm{p}} r_{21}^{\mathrm{p}} \exp\left[\left(\phi_+^{\mathrm{p}} - \phi_-^{\mathrm{p}}\right)\mathrm{i}\right]} \tag{2.42}$$

where $\phi_{\pm}^{\mathrm{p}} = d_2 k_{2z}^{\pm} = \frac{2\pi d_2}{\lambda}\left(\frac{-\varepsilon_{xz} n_1 \sin\theta_{\mathrm{i}} \pm \varepsilon_{2\mathrm{O}}\varepsilon_{2\mathrm{E}} Z_2 \varepsilon_0 c_0}{\varepsilon_{zz}}\right)$ are the phase angles in the uniaxial layer corresponding to propagating and reflecting waves, respectively. Based on Eqs. (2.22a) and (2.22b), ε_{xz} and ε_{zz} can be determined as

$$\varepsilon_{xz} = \left(\varepsilon_{2\mathrm{E}} - \varepsilon_{2\mathrm{O}}\right)\sin\beta\cos\beta \quad \text{and} \quad \varepsilon_{zz} = \varepsilon_{2\mathrm{O}}\left(\sin\beta\right)^2 + \varepsilon_{2\mathrm{E}}\left(\cos\beta\right)^2 \tag{2.43}$$

The reflectance and transmittance for the structure illustrated in Fig. 2.4(b) are calculated to be

$$R_{123}^{\mathrm{p}} = \left| r_{123}^{\mathrm{p}} \right|^2 \qquad \text{and} \qquad T_{123}^{\mathrm{p}} = \left| t_{123}^{\mathrm{p}} \right|^2 \frac{\mathrm{Re}\left[Z_3 \right]}{\mathrm{Re}\left[Z_1 \right]} \tag{2.44}$$

The theoretical foundations of this dissertation are presented in this chapter, which are later implemented into the modeling for various samples to analyze the measurement results. The CNT and AgNR samples investigated in this dissertation can be treated as effectively homogenous and uniaxial media with surface roughness and bulk inhomogeneity. The sample radiative properties can be studied by analyzing related BRDF, angle-resolved reflectance, DHR, and scattering. In addition, the EMT provides a way to estimate the effective properties of the CNT and AgNR samples which are optically uniaxial. The reflectance, transmittance, and absorptance of different samples, which can be modeled as either semi-infinite media or multi-layer structures, will be calculated based on the anisotropic thin-film optics formulation.

CHAPTER 3

MEASUREMENT INSTRUMENTATION

This chapter provides a general description of the measurement instruments and setups used for subsequent chapters, including an optical laser scatterometer for measuring BRDF, angle-resolved reflectance, and diffraction peaks, and an IS along with a monochromator for measuring the DHR.

3.1 Optical Laser Scatterometer

Optical scatterometers or reflecrometers are typical instruments for BRDF measurements. In this dissertation, a three-axis automated scatterometer (TAAS) is used to characterize the radiative properties of samples formed by both the VACNT and inclined AgNR arrays. TAAS was originally developed by Shen [89] to measure the BRDF of rough silicon wafers for accurate temperature measurement and control in rapid thermal processing (RTP), and semiconductor surface metrology and inspection. In the present work, the TAAS setup is adjusted and improved to increase the signal-to-noise ratio for low-level measurements and better accuracy.

The so-called "three-axis" in the name of the TAAS setup means the rotation axes of three movable stages, which are used to vary the angles of incidence and observation. Note that the observation angles can be angles of reflection, scattering, or diffraction, depending on the measurement purpose. Figure 3.1 shows a schematic of the experimental arrangement of the TAAS, including a light source assembling, a goniometric table, a detection and data acquisition system. Two photos of the TAAS are also depicted in Fig. 3.2 for easier visualization of three movable stages and the light

source assembling. A compact fiber-coupled diode laser system serves as the light source providing coherent and highly collimated incident light at certain wavelengths. A thermoelectric laser controller is used to maintain the laser operation temperature for better laser power stability. A 12-hour drift test shows that the standard deviation of the laser power fluctuation is less than 0.22%. An optical fiber and an adjustable laser holder provide flexibility for optical access and alignment, as well as the convenience of replacing diode lasers with different wavelengths. The laser diode is modulated at 400 Hz through an oscillating signal sent from a lock-in amplifier (EG&G 7265DSP) to the diode laser controller to reduce the effect of background radiation and stray light without using a mechanical chopper. During the measurement, the laser beam first passes through a collimator consisting of a pair of lenses and a small aperture, and then through a polarizer dial which is used to produce linearly polarized incident light. After that, the beam is divided into two portions by a beamsplitter: the transmitted portion with higher power is directed to the sample and the reflected beam goes to a stationary reference detector, which is used to monitor the laser fluctuation and improve the source stability. The sample is loaded on a holder attached with Stage 1. The rotation of Stage 1 varies the angle of incidence. A sample detector attached with Stage 2 is used to collect the light reflected or scattered from the sample surface. The rotation of Stages 2 and 3 allows the sample detector to move precisely in the upper hemisphere above the goniometric table. Two types of measurements can be conducted with the TAAS based on the sample detector movement: in-plane measurements and out-of-plane measurements. For in-plane measurements, the sample detector is confined within the POI, which is parallel to the goniometric table (the *x*-*z* plane) and illustrated as the dashed black circle in Fig. 3.1;

while for out-of-plane measurements, the sample detector can move above the POI. Both the reference and sample detectors are silicon detectors with the spectral working range from 350 to 1100 nm. The signals collected by both detectors are sent to two trans-impedance pre-amplifiers with a large dynamic range from 10 to 10^9 Ω, and later to the lock-in amplifier which provides the modulation signal for the laser controller. The output of the lock-in amplifier and two step motors are connected to a desktop with the LabView environment for data acquisition and automatic rotary-stage control.

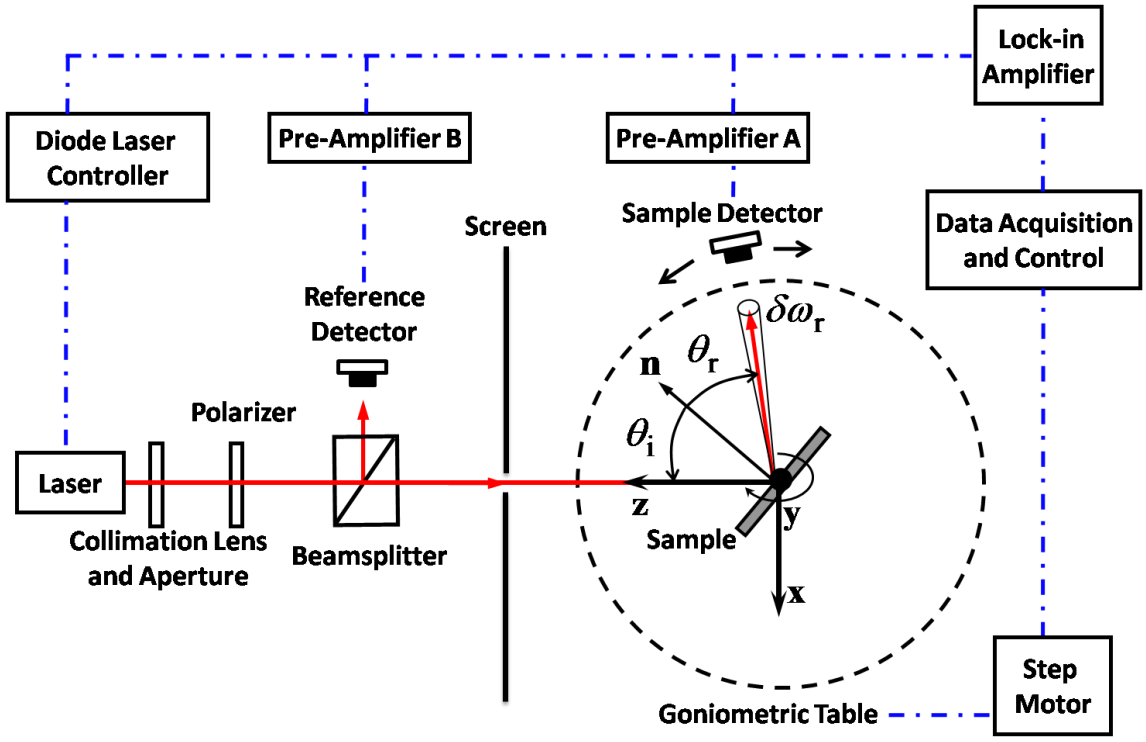

Figure 3.1 Schematic showing the experimental arrangement of the TAAS. The dashed circle represents the projection of the upper hemisphere on the goniometric table, which also indicates the sample detector movement for in-plane measurement.

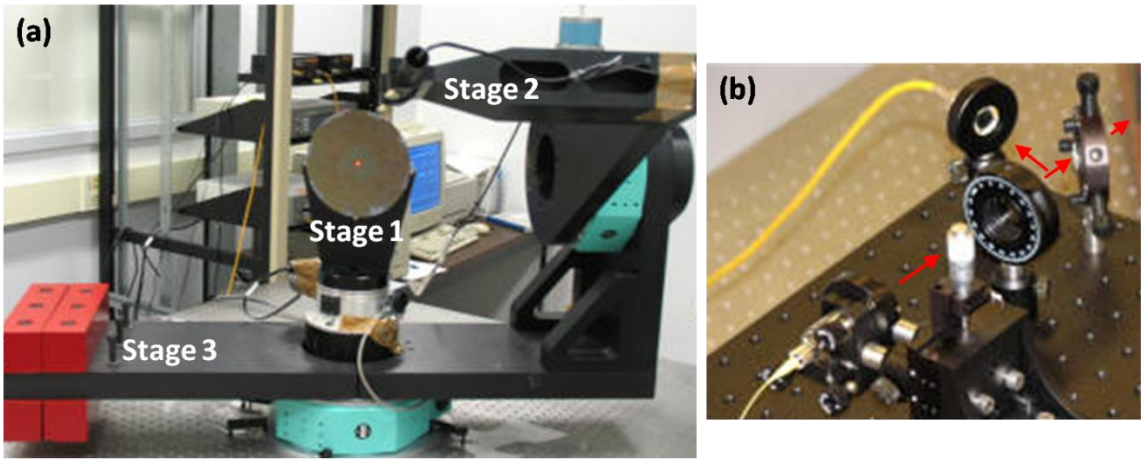

Figure 3.2 Two photos of the TAAS for easier visualization: (a) Three movable stages; (b) The light source assembling.

Since the output signal of the detector is proportional to the power received, the measurement equation of BRDF with the TAAS setup can be expressed as [89,90]

$$f_{\mathrm{r}}(\lambda,\theta_{\mathrm{i}},\theta_{\mathrm{r}}) = C\frac{S_{\mathrm{sample}}}{S_{\mathrm{reference}}\cos\theta_{\mathrm{r}}\Delta\Omega_{\mathrm{r}}} \tag{3.1}$$

where S_{sample} and $S_{\mathrm{reference}}$ are the output signals of the sample detector and the reference detector, respectively; C is a constant to compensate for the beamsplitter ratio and the different responsivities of two detectors, and $\Delta\Omega_{\mathrm{r}}$ is the solid angle of the sample detector, which is 0.000184 sr and corresponds to a 0.45^{o} half-cone angle as viewed from the laser spot on the sample. Such a small detector solid angle provides high accuracy for the TAAS measurements. Note that for in-plane measurements conducted in the present work, the azimuthal angle is confined to be either 0^{o} or 180^{o} depending on whether the sample detector projection is on the $+x$ side or $-x$ side, as can be seen from Fig. 3.1; hence the dependence of BRDF on the azimuthal angle is neglected when Eq. (2.1) is converted to the measurement equation. It should be noted here that the BRDF within $\pm 3^{\mathrm{o}}$

of the retroreflection direction cannot be measured since the sample detector blocks the incident beam at this position ($\theta_i = \theta_r$ and $\phi_i = \phi_r$). Besides BRDF, angle-resolved reflectance and diffraction efficiency can also be characterized with the TAAS following corresponding procedures, which will be further explained in the following chapters.

The maximal output power of the diode laser (single-mode) is around 3 mW at the output of the optical fiber, and will be further reduced after passing through the collimator, polarizer, and beamsplitter. To reduce the random system error, the detector signals are usually averaged over several consecutive measurements for a given position with a fixed set of θ_i and θ_r. In addition, some other approaches are adopted to improve the signal-to-noise ratio for low-level measurements of highly absorbing samples, i.e., VACNT arrays, and will be discussed in detail later. The relative uncertainty of the TAAS was estimated to be 5% with 95% confidence level for the BRDF greater than 0.01 by intercomparison with a reference standard instrument in NIST [89]. However, the uncertainty is expected to increase due to unavoidable stray light and the reduction of signal-to-noise ratio if the VACNT samples are used with extremely small reflectance.

3.2 Integrating Sphere for DHR Measurement

Ideally, the directional-hemispherical reflectance can be obtained from the TAAS measurements by collecting the BRDFs over the whole hemisphere. However, practically it is not feasible due to the large amount of measurements. Therefore, an IS is a good alternation for measuring R_{dh}. Figure 3.3 shows a schematic of the experimental setup for spectral and directional-hemispherical radiative property measurements with a custom-designed IS from Sphere Optics, Inc. [91]. A photo of the IS system is also presented in Fig. 3.4 for better visualization. The light source is a tungsten-halogen lamp with a broad

spectral range from visible to NIR. Monochromatic light is achieved by interchanging several filters on a filter wheel which acts as a "transmission window" and a monochromator (Oriel Instruments Cornerstone 130) with two gratings inside. The root mean square (rms) power fluctuation of the monochromator is less than 1%. The lamp beam which contains multi-wavelengths is diffracted by the grating (1200 lines/mm) into various directions depending on wavelengths with the required wavelength being allowed to pass through the exit slit. The beam width is determined by the width of the exit slit of the monochromator, and the beam height can be reduced by blocking both the upper and lower portions of the slit. A resolution of 10 nm (characterized at 500 nm) can be achieved with this monochromator. A mechanical chopper synchronized to a lock-in amplifier is used to modulate the signal at 400 Hz to avoid stray light. Two optical lenses with a 25-mm diameter and a 100-mm focal length are used to focus the beam at different locations of the IS based on the purposes of measurements and sample properties.

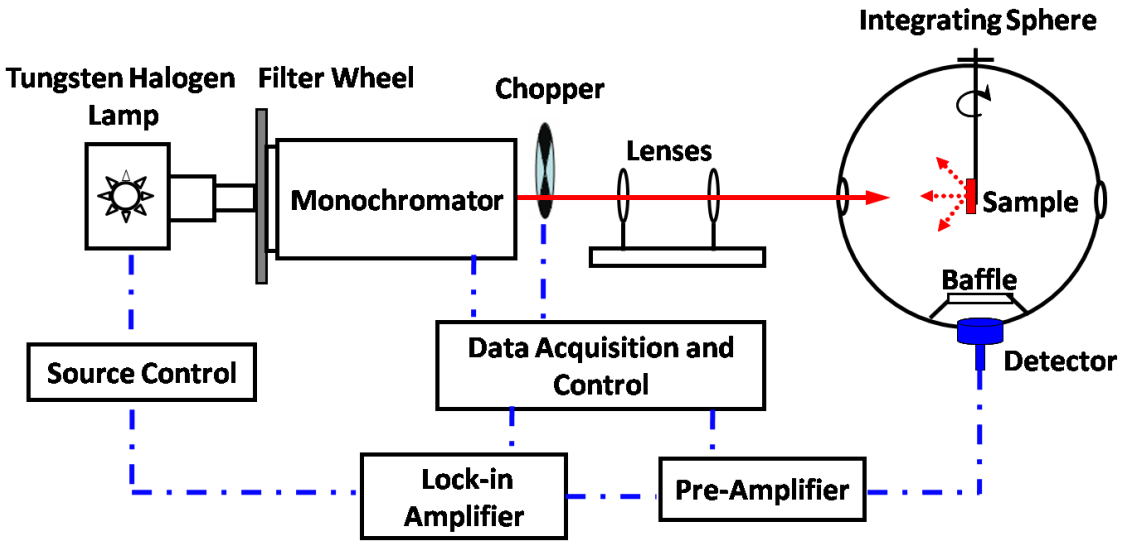

Figure 3.3 Schematic of the IS setup for spectral and directional-hemispherical reflectance measurement with the center-mount configuration. The light source is a tungsten-halogen lamp with a broad spectrum from visible to NIR. Monochromatic light is produced by a filter wheel and monochromator.

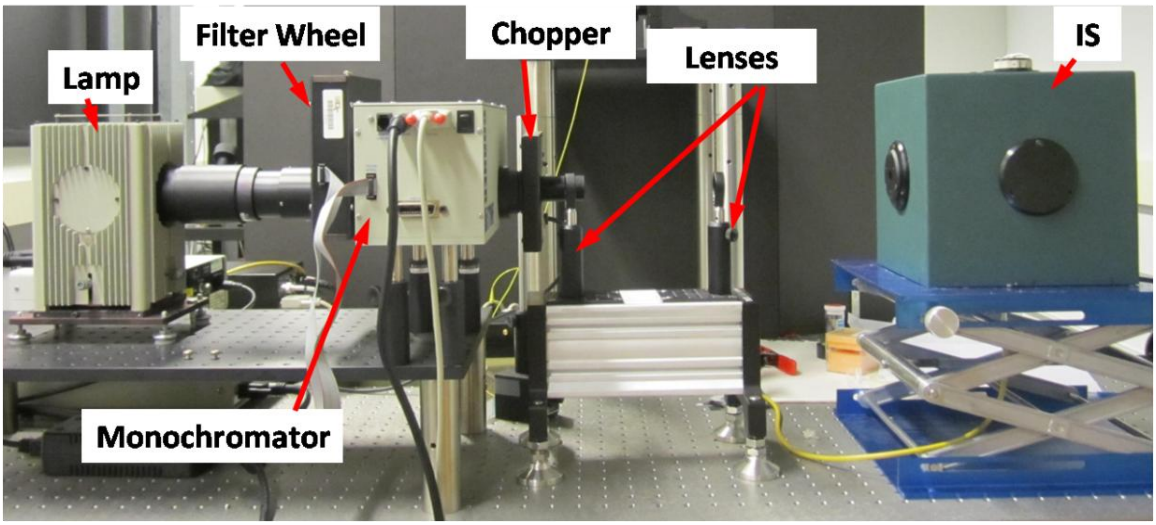

Figure 3.4 A photo of the IS system showing the light source, filter wheel, monochromator, chopper, focus lenses, and the sphere.

The IS is a 200-mm-diameter sphere imbedded in a cube, which has 25-mm-diameter ports on all sides. The inner wall of the IS is coated with polytetrafluoroethylene (PTFE), which is a nearly perfect diffuse reflector with a reflectance of approximately 0.988 in the wavelength region of interest [92,93]. Monochromatic beam enters the IS through the entrance port and is focused on the sample surface. The sample can be mounted on a rotary holder through the top port of the IS (center-mount configuration), or on the back port (back-mount configuration), or on the front port (front-configuration) for different measurement purposes. If the center-mount configuration is used, by rotating the sample holder, the beam can be directed either onto the back wall of the sphere to obtain the reference signal or onto the sample to obtain the sample signal. For the other two configurations, the sample signal and reference signal are obtained by loading and removing the sample from corresponding ports, respectively. The light reflected and scattered by either the sample or the reference hits on the PTFE coating and finally goes

to a detector through multi-reflection. The detector for signal collection is located at the bottom port of the IS and is covered by a baffle placed above to prevent the direct illumination of the first reflected light from the sample. To ensure that the DHR measurement covers both the visible and part of the NIR spectra, two types of detectors are used, which are a silicon detector with the working spectral range from 400 to 1000 nm and a germanium detector with the working spectral range from 1100 to 1800 nm. The detector signal is amplified by a trans-impedance pre-amplifier, and then sent to a lock-in amplifier collecting signals at the chopping frequency of 400 Hz. The ratio of the sample signal to the reference signal gives the R_{dh} for samples with the back-mount configuration, T_{dh} for samples with front-mount configuration, and $R_{dh} + T_{dh}$ for samples with center-mount configuration. Based on Kirchhoff's law, the absorptance can be determined. Note that if the sample is opaque, then both the center-mount and back-mount configurations measure R_{dh}. However, the center-mount configuration provides an easy way for varying the angle of incidence by rotating the sample holder as compared with the back-mount configuration.

The size of lamp beam spot on the sample suspended in the sphere center is approximately 6 mm × 6 mm with good focus. Hence, measurements with large angles of incidence are limited by the sample size which should be less than 1 inch × 1 inch as required by the port dimensions. Replacement of the tungsten-halogen lamp with a thermoelectrically-cooled diode laser at a certain wavelength provides more space for variation of incidence angles because of its small beam size (3 mm in diameter). While the laser source is less capable for continuous spectral property measurement, it has some advantages over the lamp source. Besides the larger variation range of incidence angles,

the diode laser provides more stable and higher optical power than the lamp connected with a monochromator, resulting in noise reduction. For the IS-Laser operation, the lock-in amplifier is connected to the diode laser controller to modulate the frequency electrically; hence, no chopper is needed. In addition, a linear polarizer can be placed between the diode laser and the IS to measure the reflectance with *p* or *s* polarization separately.

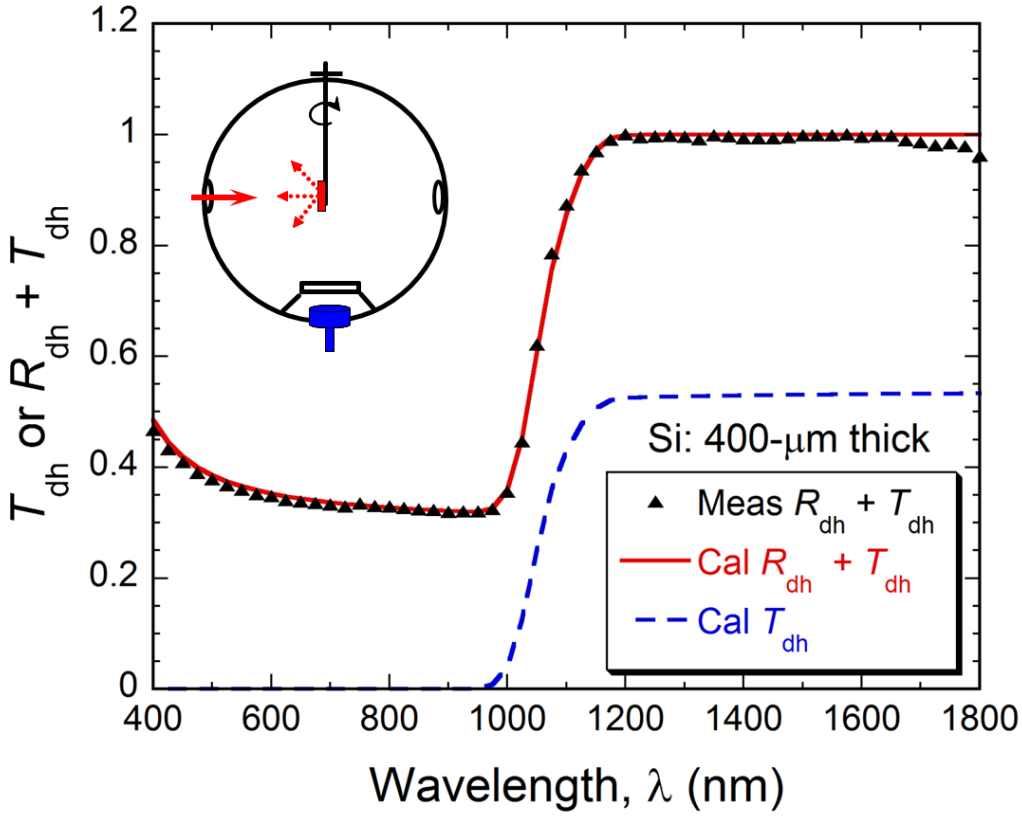

Figure 3.5 Calibration of IS by comparing the measurements with theoretical calculation of the spectral and directional-hemispherical radiative properties of a bare silicon wafer.

A number of facts can affect the accuracy of the integrating sphere measurements and, therefore, calibration and corrections are often necessary to reduce the measurement uncertainty [94]. A double-side polished silicon wafer with a thickness of 400 μm is used

to calibrate the IS with the center-mount configuration. At wavelengths longer than approximately 1050 nm, silicon becomes semitransparent, and the ratio of the sample signal to the reference signal gives the sum of R_{dh} and T_{dh}, as shown in Fig. 3.5. The wafer is tilted for about 7° so that the light specularly reflected by the silicon wafer would not escape from the entrance port. The measurement results agree well with those predicted, using the empirical formulation of bare silicon from Lee et al. [95]. The average standard deviation of the results from IS measurement and those from theoretical modeling is approximately 1.3%. Slightly larger differences exist at the ends of the spectrum but are still less than 4%.

Detailed instrumentation of the TAAS and IS setups is provided in this chapter,. Generally speaking, TAAS characterizes the angular properties of samples, such as BRDF, diffuse component of reflectance, and angle-resolved reflectance at a certain wavelength, and IS measures the spectral DHR in the visible and NIR ranges. Related calibration procedures and uncertainty estimation under typical operation conditions are also presented. The actual measurement uncertainties may vary for different samples and will be explained in details in subsequent chapters.

CHAPTER 4

HIGHLY ABSORBING CARBON NANOTUBE ARRAYS: TIP GROWTH VS. BASE GROWTH

The nanostructured material described in this chapter is arrays formed by VACNTs. In general, CNTs can be divided into two categories: SWCNTs and MWCNTs depending on their wall numbers. An SWCNT can be conveniently illustrated as a graphene sheet of honeycomb structure rolled along a certain chiral direction [96]. Depending on the chiral direction, the SWCNT can be either semiconducting or metallic. An SWCNT has only one shell with a diameter usually less than 2 nm. An MWCNT, which is similar to an SWCNT for the individual wall structure, usually consists of multiple concentric cylindrical shells of wrapped graphene layers coaxially arranged around a central hollow with a constant separation between adjacent layers [97-99]. The typical diameter of an MWCNT lies between 2 to 30 nm. Arrays formed by CNTs are highly absorbing for two reasons: one is the material properties of carbon π-band absorption, and the other is the low array density of CNTs imbedded in air. The extremely high absorption of several vertically aligned MWCNT samples is demonstrated by an experimental study as described in this chapter along with the effect of growth mechanisms on the CNT radiative properties.

4.1 Sample Fabrication and Characterization

There have been a large number of manufacturing processes with different metal catalysts in various temperature ranges for CNT growth, among which, thermal chemical

vapor deposition (TCVD) is a synthesis method with easily controlled parameters and ability for manufacturing relatively large areas with high throughput [100]. This method was first described by Baker [101] in carbon filament formation. First the hydrocarbon feedstock is pyrolytically dissociated into carbon and hydrogen. The carbon then dissolves into, and forms a saturated solution with the metal nanoparticle before it precipitates on the surface to form a nanotube. The growth continues through addition of small C-C particles until the catalyst particle is eventually poisoned by impurities or stable carbide formation.

The samples were prepared by Dr. Ready's group in GTRI. The CNTs were synthesized on double-side polished (100) silicon substrates, approximately 400 μm in thickness and 25 mm × 25 mm in area. During the fabrication process, an iron catalyst layer of approximately 10 nm was deposited by a resistively heated thermal evaporation system at 4.3×10^{-4} Pa. Iron wire with 127 μm diameter and 99.999% purity was used as the catalyst source. Vertically aligned MWCNTs were synthesized in a programmable furnace as described by Camacho et al. [3]. The substrate was heated to 820^{o}C, and Argon gas was introduced into the furnace as a carrier gas at a flow rate of 1000 standard cubic centimeters per minute (sccm). After 13 minutes of temperature ramp, a gas mixture of 1000 sccm methane, 120 sccm ethylene, and 500 sccm hydrogen was introduced with various soak times. Afterward, the tube furnace was quenched to 676^{o}C in ten minutes under a 1000 sccm flow of Argon. In the end, the furnace was cooled to room temperature and the sample was removed. Figure 4.1 depicts the fabrication systems with a schematic of the synthesis setup and a photo of the TCVD chamber, gas supply, and computer based programming controller.

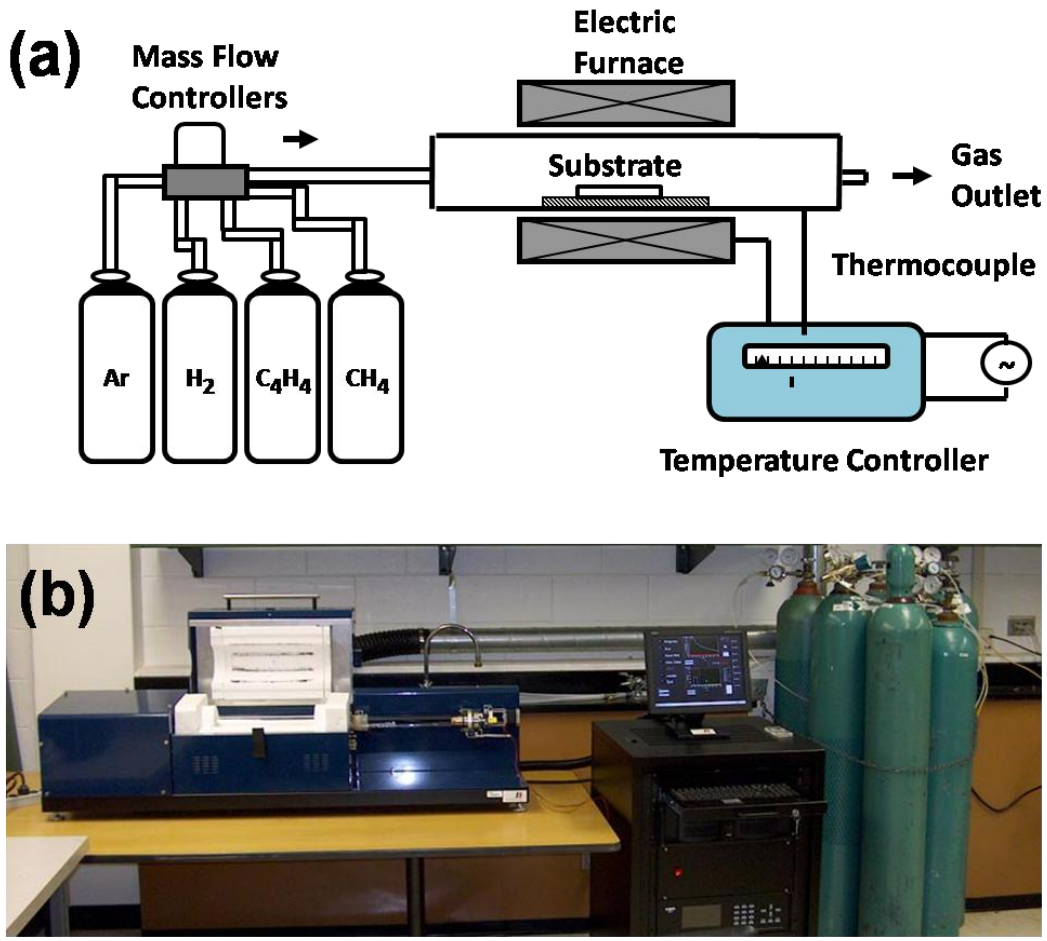

Figure 4.1 Illustrations of fabrication systems: (a) A schematic of the synthesis setup; (b) A photo of the TCVD chamber, gas supply, and programmable computer controller.

Depending on the interaction of the catalyst nanoparticle and substrate, two growth mechanisms exist for the CNT fabrication [101]: base (or root) growth and tip growth, as can be seen from Fig. 4.2. Base growth is characterized by a strong catalyst-substrate adhesion; however, in tip growth, substrate-catalyst adhesion is rather weak. Liu et al. [102] showed that carbon deposits on the CVD reactor sidewalls can affect the growth of CNT arrays through the re-deposition of carbonaceous byproducts from previous CNT growth runs. It is found that samples grown with a high concentration of carbon byproduct on the reactor sidewalls are prone to tip growth. The re-deposition of

carbonaceous impurities from the reactor sidewalls on the Si substrate may have weakened the adhesion of the iron catalyst nanoparticles, causing them to be carried up from the Si substrate during the CNT growth.

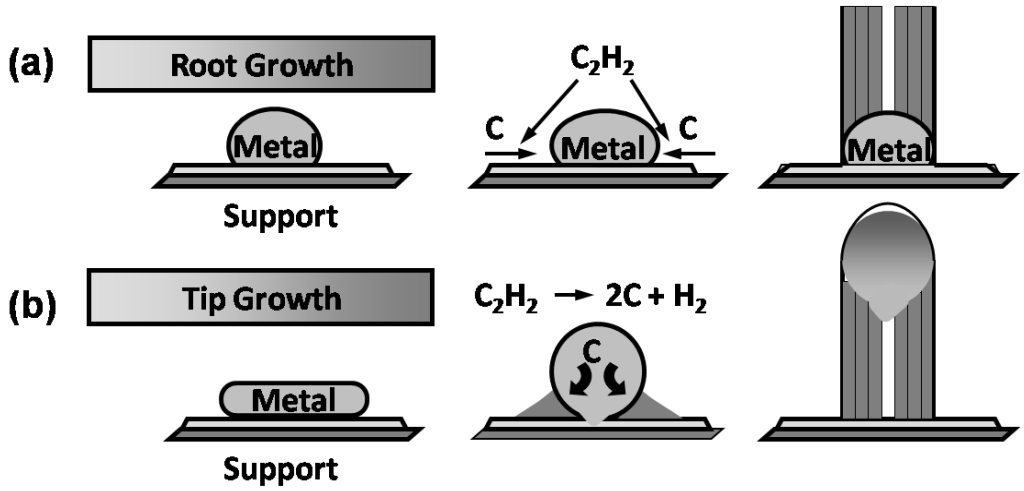

Figure 4.2 Two growth mechanisms: (a) Root growth with metal catalyst on bottom; (b) Tip growth with metal catalyst on top.

In total, there were six samples fabricated. Samples 4, 5, and 6 are tip-growth dominant as observed by SEM images. In order to remove the carbon byproducts, the CVD reactor was cleaned by heating the chamber to slightly less than 1000^{o}C in ambient atmosphere. The removal of these sidewall impurities results in better adhesion between the iron catalyst nanoparticles and the substrate. Samples 1, 2, and 3 were prepared after cleaning of the sidewalls and are base-growth dominant. Figure 4.3 displays the SEM images of a base-growth and a tip-growth VACNT sample. As shown in Fig 4.3(a), the tip-growth sample has noticeable iron catalyst nanoparticles (white) at the top of the CNTs. On the other hand, the SEM image of the surface of the base-growth sample shown in Fig. 4.3(b) looks like dark clouds, suggesting a high degree of surface roughness.

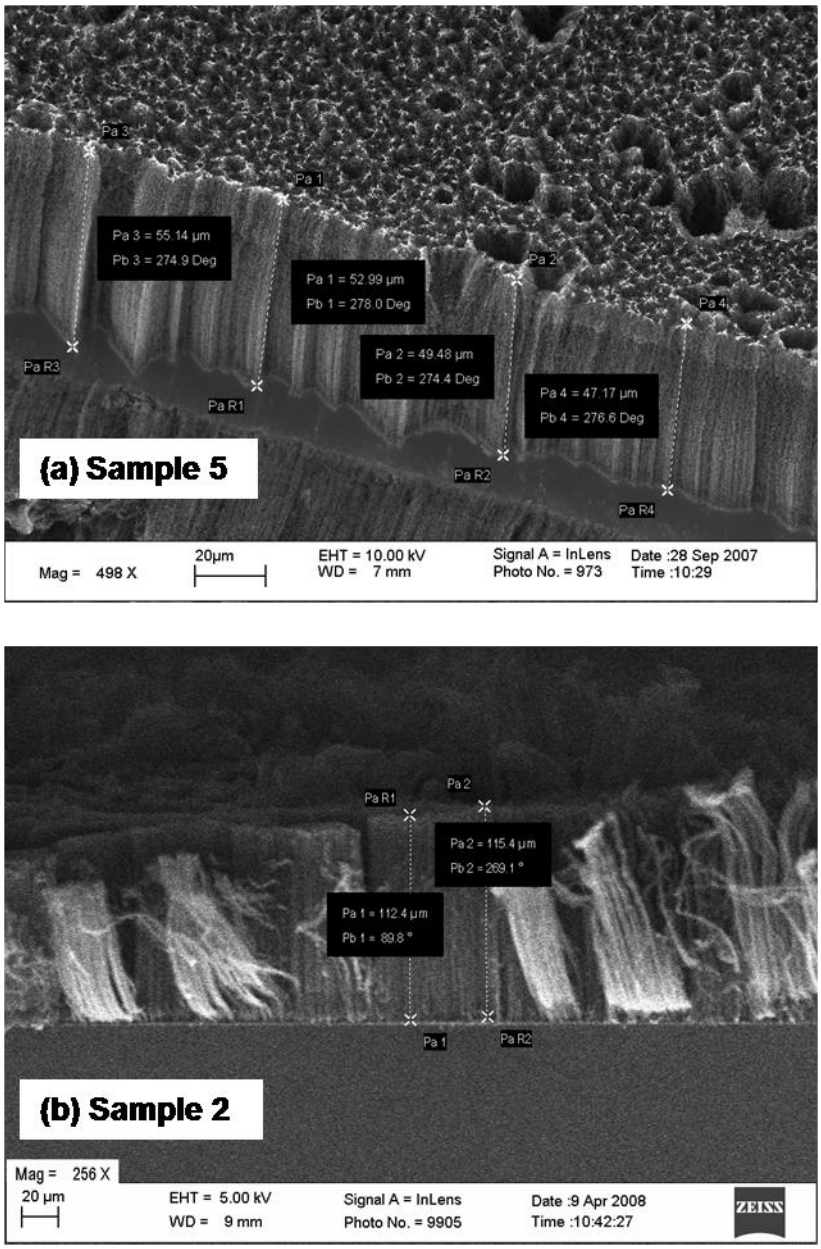

Figure 4.3 SEM images: (a) Sample 5, which is tip-growth dominant with catalyst nanoparticles at VACNT tips; (b) Sample 2, which is base-growth dominant.

Table 4.1 lists the parameters of fabricated samples, including the thickness (*d*) and the density of VACNT carpet, as well as the volume (filling) fraction denoted by *f*. The thickness was calculated based on the average from the SEM pictures taken at different locations, and the standard deviation is also shown to indicate the uniformity of

the sample. For Samples 1 to 3, the SEM images were obtained by dicing corresponding samples under the same growth conditions, while for Samples 4 to 6, the SEM images for individual samples were taken from their side edges. The thickness was obtained by averaging more than 40 measured points for each sample. The nonuniformity in the CNT thickness is associated with misalignment and other defects, as can be seen clearly from the SEM image of Sample 2 as shown in Fig. 4.3(b). The variations in the sample parameters are caused by the intentional variations in the fabrication parameters, such as the flow rates of the reaction gases, the growth temperature, soak time, and the size of the catalyst nanoparticles as well as other particles in the furnace. The weight was measured with an analytical balance by removing the CNTs from the substrate, after the reflectance of the samples was measured. By assuming that the density of the VACNTs is the same as that of graphite (2.2 g/cm^3), we used the ratio of the sample density to that of graphite to estimate the volume fraction of the VACNT carpet. Due to the thickness nonuniformity and the uncertainty in the weight measurement, the estimated uncertainty is up to 50% in density and volume fraction.

Table 4.1 Parameters of the VACNT samples used in the present study.

Sample #	Growth mechanism	Thickness d (μm)	Density (g/cm^3)	Volume fraction f (%)
1	base-growth	86 ± 10	0.079	3.6
2	base-growth	107 ± 18	0.072	3.3
3	base-growth	141 ± 9	0.046	2.2
4	tip-growth	56 ± 13	0.180	8.2
5	tip-growth	54 ± 8	0.330	15
6	tip-growth	88 ± 14	0.025	1.1

The values in Table 4.1 show that the densities of Samples 4 and 5 are much higher than those of Samples 1 to 3; this may be explained by the iron catalyst nanoparticles and other carbonaceous impurities for the tip-growth samples (Samples 4 and 5). For base-growth samples, the iron catalyst nanoparticles are presumed to remain on the substrates, when the CNTs were removed for the weight measurement. It is not clear why the density of Sample 6 (tip growth) is the lowest among all measured samples. However, it was noted that the surface of Sample 6 had been damaged after spectroscopic measurements and was not uniformly covered by CNTs before the weight measurement. A large portion of the substrate surface was not covered by CNTs, resulting in a much lower estimated density. Hence, the density for Samples 4, 5, and 6 may not reflect the actual density of the VACNTs. Nevertheless, the density and volume fraction of these samples are listed in Table 1 for reference only. The volume fraction for Samples 1 to 3 varies in the range from 2% to 4%, which is comparable with the values reported by Yang et al. [1].

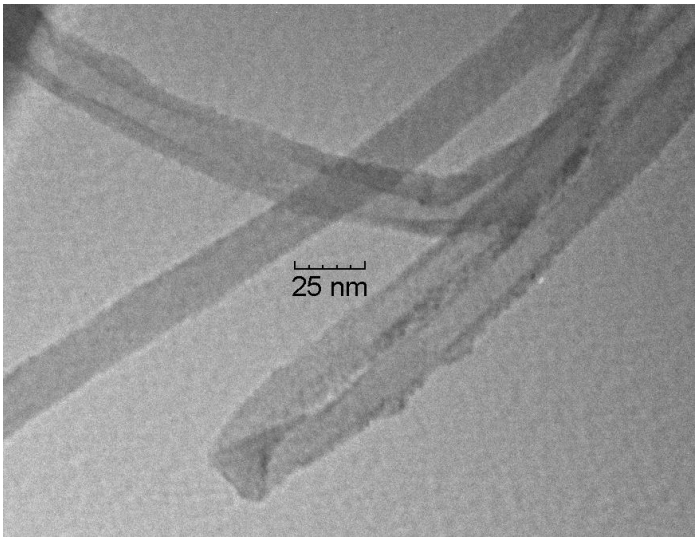

Figure 4.4 TEM image of the MWCNTs under the same growth conditions as those of the measured samples.

The diameters of the VACNTs were measured with transmission electron microscopy (TEM), by scraping the VACNTs from the silicon substrate onto a lacey carbon grid and imaging on a JEOL 100CX2 TEM operated at 100 kV. Figure 4.4 presents the TEM image of a CNT sample under the same growth conditions as those of the measured samples. From the TEM images, the average diameter of the VACNT samples is around 25 nm.

4.2 Measurement Results and Discussions

4.2.1 Directional-Hemispherical Reflectance

The IS with a grating monochromator as described in Chapter 3 was used to measure the spectral, directional-hemispherical reflectance of those six CNT samples. The measurement spectral range was from 400 to 1800 nm with an increment of 25 nm provided by the tungsten-halogen lamp with continuous broad spectra as the light source. Two detectors were used: a silicon detector for the wavelength range from 400 to 1000 nm and a germanium detector for the wavelength range from 1100 to 1800 nm. The center-configuration was adopted for reflectance measurement since all samples were essentially opaque. This was verified by placing the sample in front of the entrance port of the sphere and the obtained transmittance signal of the samples was negligible.

The measured R_{dh} spectra of the six CNT samples are shown in Fig. 4.5 in the wavelength region from 400 to 1800 nm. Since the CNT samples exhibit a much lower reflectance (less than 3%), it is difficult to achieve high accuracy in the reflectance measurement. As to be seen from the BRDF measurement results in the later discussions, the CNT samples scatter light toward the whole hemisphere with a large specular peak and significant retroreflection. Therefore, the samples are neither diffuse nor specular.

Hence, in the DHR measurement, each CNT sample was tilted by about 7° to reduce the fraction of light being reflected back to the entrance port. Based on previous study and the view factor of the entrance port to the whole sphere, approximately 1.5% of the light reflected by a diffuse sample will escape from the entrance port [93]. Because of retroreflection, the percentage of light escaping the entrance aperture is estimated to be larger around 2-4%. Corrections were not made because it is difficult to quantify the exact amount of reflected light that escapes the aperture. A major uncertainty arises from the lower signal-to-noise ratio and sample nonuniformity. A black shielding tube was placed in front of the entrance port to prevent stray light from entering the sphere. The noise level was found to be a few percent of the signal when the reflectance is less than 1%. Repeated measurements of the sample suggested that the relative standard deviation was within 5%. The relative expanded uncertainty in R_{dh} is estimated to be 15% for the CNT samples. The error bars indicate the uncertainties for Sample 1 and Sample 4. The measurement results are not good enough and not shown in Fig. 4.5 for the spectral range of 1000 nm < λ < 1100 nm, because of the instrument limits of the grating, filter, and detector when used as a combination. There is some discontinuity between 1000 and 1100 nm due to the change of measurement configurations, i.e., different detectors and gratings of the monochromator, especially for Samples 4 and 5. It should be noted that while the responsivity of the germanium detector is about one order of magnitude lower than that of silicon at 1000 nm, the change of the gratings results in about one order of magnitude enhancement of the light intensity in the long wavelength region. Hence, the signal-to-noise ratio is similar in different spectral regions.

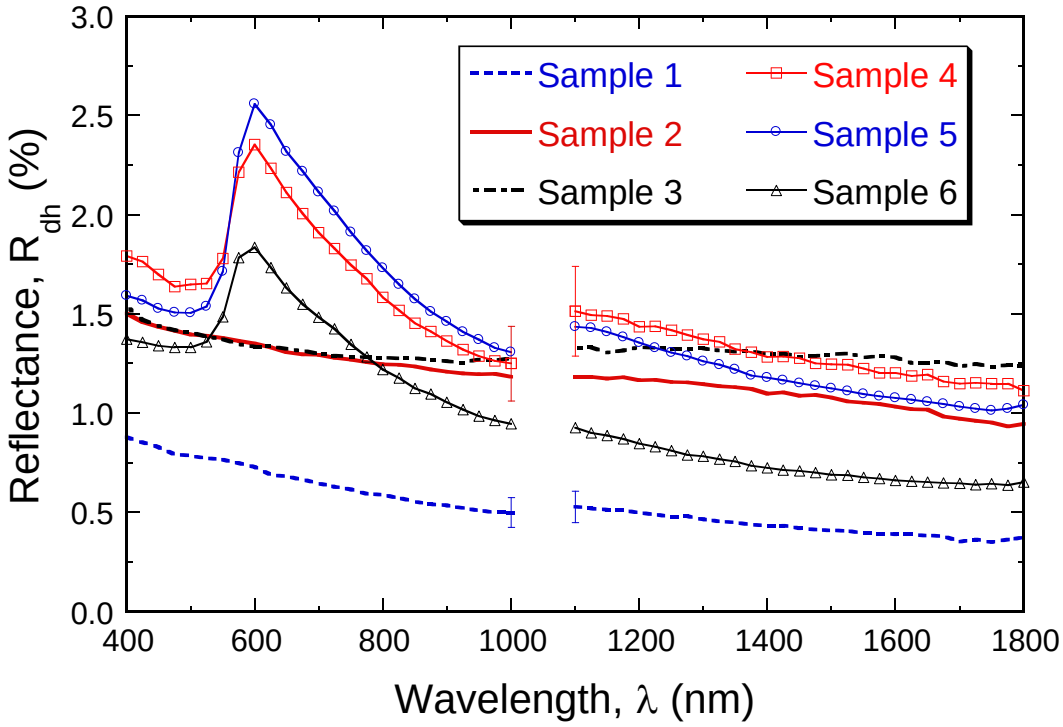

Figure 4.5 R_{dh} of six CNT samples measured with the IS in the spectral ranges from 400 to 1000 nm and from 1100 to 1800 nm. The usage of different grating and detector combinations results in the discontinuities of the curves from 1000 to 1100 nm.

The most noticeable feature in the reflectance spectra shown in Fig. 4.5 is the reflectance peak near λ = 600 nm for tip-growth dominant samples (#4, 5 and 6). This is attributed to the iron impurities on top of the CNTs. Visual inspection reveals that the surfaces of Samples 4 to 6 appear somewhat brownish, unlike the pure black look of Samples 1 to 3. In general, the reflectance decreases slightly toward longer wavelength. It can be seen that Sample 1 exhibits the lowest reflectance, which is less than 1% in the measured spectral region and less than 0.5% for λ > 1200 nm, suggesting that the absorptance $\alpha = 1 - R_{dh}$ is between 0.991 (at λ = 400 nm) and 0.996 (at λ = 1800 nm). The high absorptance with excellent spectral uniformity is ideal for thermal detectors and emitters. The variations of the reflectance among different samples are not related to the

thickness, because the thickness of the CNTs is much greater than the photon penetration depth such that the CNTs can be treated as semi-infinite. The entanglement of VACNTs, iron and other impurities, nonuniformity of the sample surface, and measurement uncertainty may be responsible for the sample-to-sample variations.

4.2.2 Bidirectional Reflectance Distribution Function

The BRDFs of CNT samples were measured with the TAAS at the 635-nm wavelength for different polarizations. Due to the high absorption of CNTs which decreases the signal-to-noise ratio, several approaches were implemented before each measurement in order to increase the power received by the sample detector. First, the optical fiber was adjusted for each polarization to maximize the output power by improving the coupling between the optical fiber polarization and polarizer [90]. Second, a black screen was used to separate the light source assembling and the sample-detector area during the BRDF measurements to further decrease the effect of stray light. Last, the sample holder was wrapped with black carbon tapes so that light incident on the sample holder will be largely absorbed instead of being reflected and going to the detector.

The measured BRDFs of two representative samples are shown in Fig. 4.6, at incidence angles of 0^{o}, 30^{o}, and 60^{o} for both *s* and *p* polarizations. The value of $f_{\mathrm{r}} \cos\theta_{\mathrm{r}}$, which is the so-called cosine corrected BRDF generally used in previous studies, is plotted for clarity and to facilitate the discussion. The reflection angles covered $\pm\ 80^{o}$ with respect to the surface normal of the sample. Recall that Sample 1 is base-growth dominant with a very low reflectance (approximately 0.7% at λ = 635 nm) and Sample 4 is tip-growth dominant with a relatively higher reflectance (approximately 2.2% at λ = 635 nm). Although the BRDF of Sample 1 is much lower than that of Sample 4, the

BRDFs of both samples exhibit similar angular and polarization dependence. The BRDFs of Samples 2, 3, and 5 were also measured and similar trends were observed but not shown in the figure.

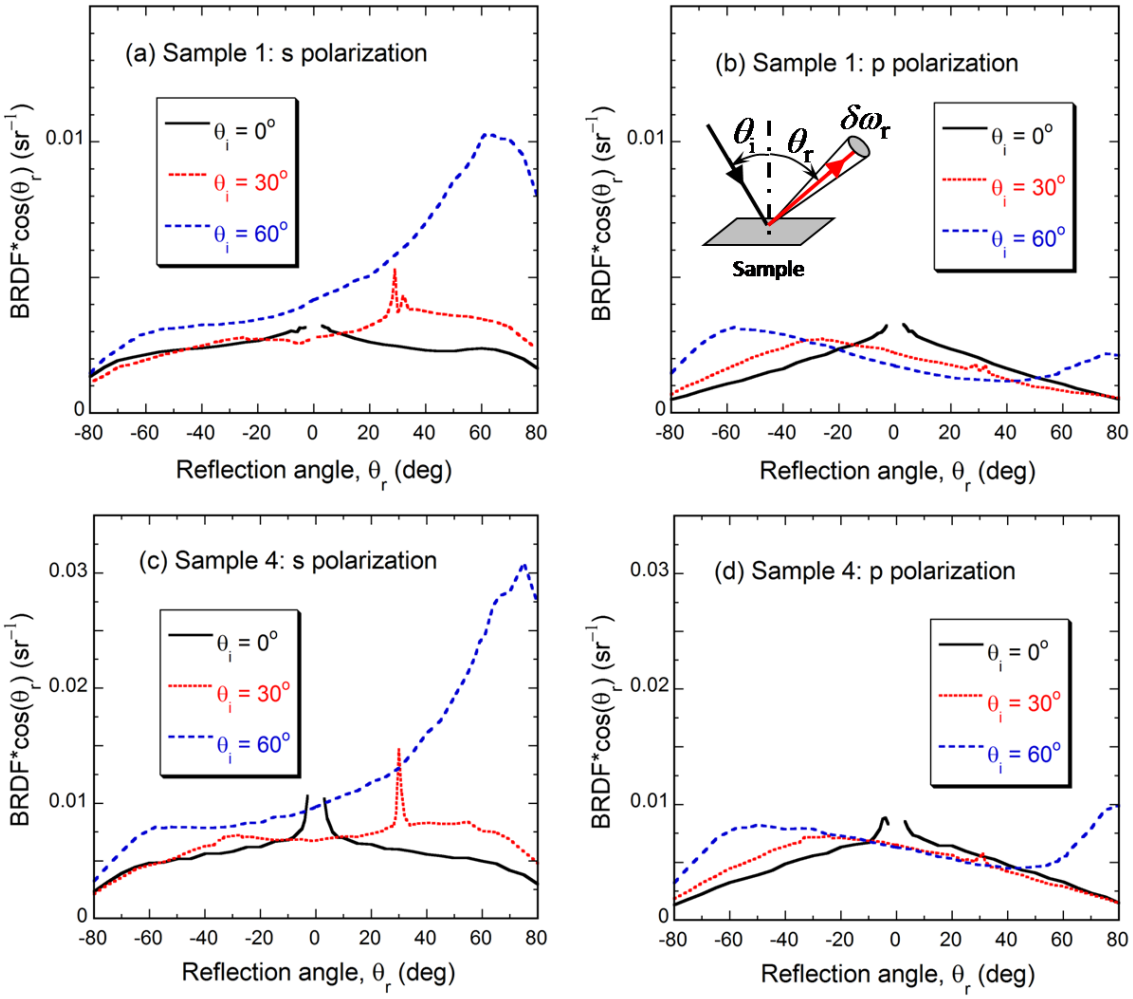

Figure 4.6 BRDF measurements of Sample 1 (a,b) and Sample 4 (c,d) at different incidence angles for both *s* polarization (left) and *p* polarization (right). The inset of Fig. 4.6(b) shows the geometry of bidirectional reflection.

If the reflection from the sample surface were perfectly diffuse, the scatted light would follow the Lambertian law such that the BRDF would be independent of the observation angle. On the other hand, a specular surface would reflect light in the

specular direction only. The scattering from the VACNT samples is much more complicated however. At normal incidence, there exists a peak around $\theta_r = 0°$. This could be caused by specular reflection and/or retroreflection. Furthermore, the trend of the BRDF depends on the polarization even at normal incidence. At $\theta_i = 30°$, there exists a much larger specular peak for *s* polarization than for *p* polarization. This appears to follow the Fresnel equations of reflection at a smooth interface [76]. For Sample 1, there exist split peaks near the specular observation angle of $\theta_r = 30°$ for both polarizations. Split specular peaks were previously observed for a gold film coated on microrough silicon samples and explained by diffraction from the rough surfaces [103]. Retroreflection can be seen in a large region of observation angle (even though the measurement was not done at $-\theta_i - 3° \le \theta_r \le -\theta_i + 3°$ due to beam blocking) for $\theta_i = 30°$ and $60°$. The cause of retroreflection may be associated with scattering by catalyst nanoparticles and/or by the enclosed cup on the CNT tips, since Rayleigh scattering by small particles can have a strong backward component in the scattering phase function. At $\theta_i = 60°$, there exists strong forward reflection that overshadows the specular peaks, especially for *s* polarization. This is consistent with the observation of volume scattering samples [104]. While the exact reasons need further investigation, scattering by rough surfaces, by small particles, and by volumetric defects seems to have interplayed, leading to the distinct features in the measured BRDF of the VACNT samples.

Table 4.2 Comparison of the absorptance $\alpha = 1 - R_{dh}$ from integration of BRDF at normal incidence and from the integrating sphere measurement at λ = 635 nm.

Sample #	Integrating Sphere α (%)	Integration of BRDF α (%)	Relative Difference (%)
1	99.3	99.0	0.3
2	98.7	98.5	0.2
3	98.7	98.4	0.3
4	97.8	97.6	0.2
5	97.6	97.3	0.3
6	98.3	-	-

At normal incidence, R_{dh} can be estimated by integrating the BRDFs averaged over the two polarizations, by assuming that the samples are isotropic with respect to the azimuthal angle. Note that BRDF was not measured for Sample 6 due to surface damage after integrating sphere measurements. For the other five samples, except for Sample 1, the integrated reflectance is higher than that measured with the IS by less than 10–20%. This is anticipated because the reported *R* values from the IS measurement may be slightly lower due to the loss of the reflected light through the entrance port, while the BRDF results may be slightly higher than the actual values due to stray light. For Sample 1, due to its low reflectance, the reflectance obtained from integration of the BRDF is approximately 1%, which is about 43% higher than that measured with the sphere. Despite the relatively large difference in the reflectance, the two methods give very close agreement in terms of the absorptance of the samples, with a difference of 0.2% to 0.3%

for all five samples, as shown in Table 4.2. An absorptance of greater than 98.5% was achieved for three base-growth samples as demonstrated by IS measurements.

4.3 Theoretical Modeling

Without considering scattering and surface roughness, the CNT carpet may be treated as a homogeneous thin film with effective optical constants. The optical properties of such idealized system may allow one to estimate the maximum achievable absorptance and also provide quantitative information on the absorption coefficients and penetration depths for various wavelengths and volume filling factors. The EMT introduced in Chapter 2 is a homogenization method of characterizing the optical properties of inhomogeneous media based on the average of the electric fields [85,86].

A VACNT can be considered as a graphene sheet (a single layer of graphite with the hexagonal lattice) wrapped into a seamless cylinder along different rolling directions. Due to birefringency, the dielectric function of graphite consists of two components: $\varepsilon_{\perp}$ and $\varepsilon_{\parallel}$ which correspond to the cases that the polarization is normal (ordinary rays) and perpendicular (extraordinary rays) to the c-axis of graphite, respectively. Here the c-axis of graphite is in the same direction of the surface normal to a graphene sheet [87], which is shown in Fig. 4.7(a). By assuming that the dielectric function of a VACNT is uniform within the whole tube and locally identical to that of graphite, the dielectric constants of an individual VACNT can be obtained after a coordinate transformation from Cartesian coordinates to cylindrical coordinates, neglecting the hollow core of the VACNT [28]. Then, the effective dielectric function of a VACNT carpet can be calculated based on the general MG approach which gives the effective dielectric function as [40]

$$\varepsilon_{\text{eff}}^{\text{O}} = \frac{\varepsilon_{\parallel} + \sqrt{\varepsilon_{\parallel}/\varepsilon_{\perp}} + (\varepsilon_{\parallel} - \sqrt{\varepsilon_{\parallel}/\varepsilon_{\perp}})f}{\varepsilon_{\parallel} + \sqrt{\varepsilon_{\parallel}/\varepsilon_{\perp}} - (\varepsilon_{\parallel} - \sqrt{\varepsilon_{\parallel}/\varepsilon_{\perp}})f} \tag{4.1}$$

and

$$\varepsilon_{\text{eff}}^{\text{E}} = f\varepsilon_{\perp} + 1 - f \tag{4.2}$$

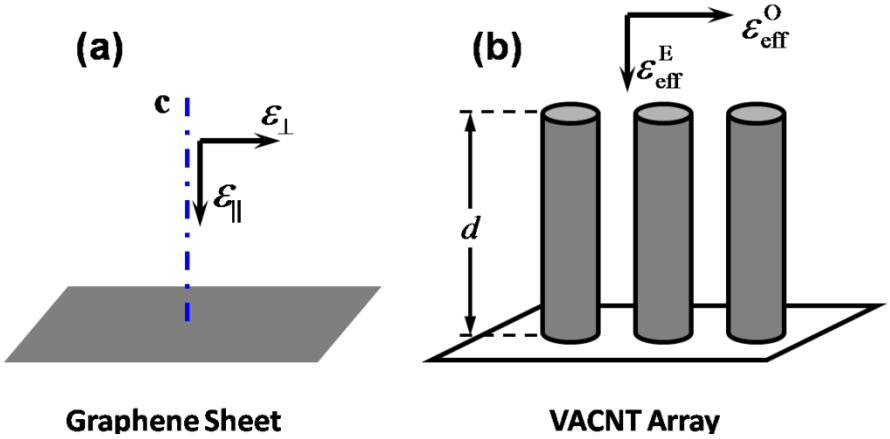

Figure 4.7 Schematic showing the polarization-dependent dielectric functions of (a) Single graphene sheet; (b) VACNT array.

Since the VACNT-air layer is anisotropic, it reflects differences in the dielectric function for differently polarized incident light. The superscripts "O" and "E" in Eqs. (4.1) and (4.2) denote two effective principle dielectric functions when the incident electrical field is normal or parallel to the effective optical axis **c** along the nanotube direction, respectively, as can be seen from Fig. 4.7(b). The overall effective dielectric function can be obtained by

$$\varepsilon_{\text{eff}} = (n_{\text{eff}} + i\kappa_{\text{eff}})^2 = x\varepsilon_{\text{eff}}^{\text{O}} + (1-x)\varepsilon_{\text{eff}}^{\text{E}} \tag{4.3}$$

where x specifies the fraction of contributions by the two effective dielectric functions. For ideal VACNT samples at normal incidence, $x = 1$ and the effective dielectric function is dominated by $\varepsilon_{\text{eff}}^{\text{O}}$ since the electric field is always perpendicular to the CNTs

regardless the polarizations. In practice, however, certain contribution from $\varepsilon_{\text{eff}}^{\text{E}}$ must be included due to the imperfect alignment and entanglements of VACNTs.

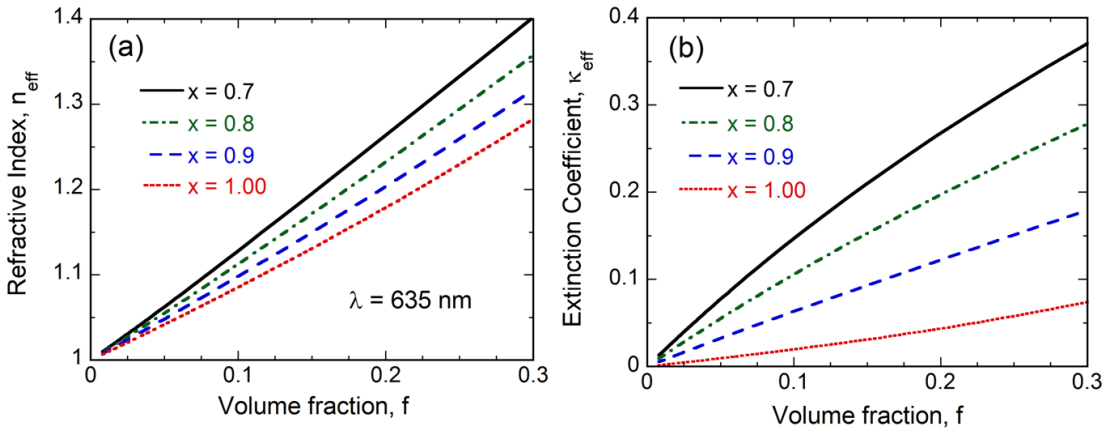

Figure 4.8 Effective optical constants calculated from EMT as a function of *f* for different combination factors at λ = 536 nm: (a) Refractive index; (b) Extinction coefficient.

Figure 4.8 shows the effective refractive index n_{eff} and extinction coefficient κ_{eff} of VACNT carpets calculated based on Eqs. (4.1) to (4.3) as functions of the volume fraction *f* for different *x* values at λ = 635 nm. The optical constants of graphite for both polarizations are taken from Palik [87]. It can be seen from Fig. 4.8, both n_{eff} and κ_{eff} increase with *f* and decrease as *x* increases. Taking *f* = 0.03 and *x* = 0.9 as an example, the calculated $n_{\text{eff}} = 1.03$ and $\kappa_{\text{eff}} = 0.02$ resulting in a small radiation penetration depth $\lambda/(4\pi\kappa_{\text{eff}}) \approx 2.5\ \mu\text{m}$, which is much smaller compared with the thicknesses of all samples. The reflectivity at the interface between air and VACNT carpet at normal incidence can be calculated by [76]

$$\rho_{\lambda} = \frac{(n_{\text{eff}} - 1)^2 + \kappa_{\text{eff}}^2}{(n_{\text{eff}} + 1)^2 + \kappa_{\text{eff}}^2} \tag{4.4}$$

Because $\kappa_{\text{eff}} << n_{\text{eff}}$, ρ_λ is close to zero when n_{eff} is close to 1. At λ = 635 nm for f = 0.03 and x = 0.9, one obtains ρ_λ = 0.12%; for f = 0.03 and x = 1, one obtains ρ_λ = 0.06%.

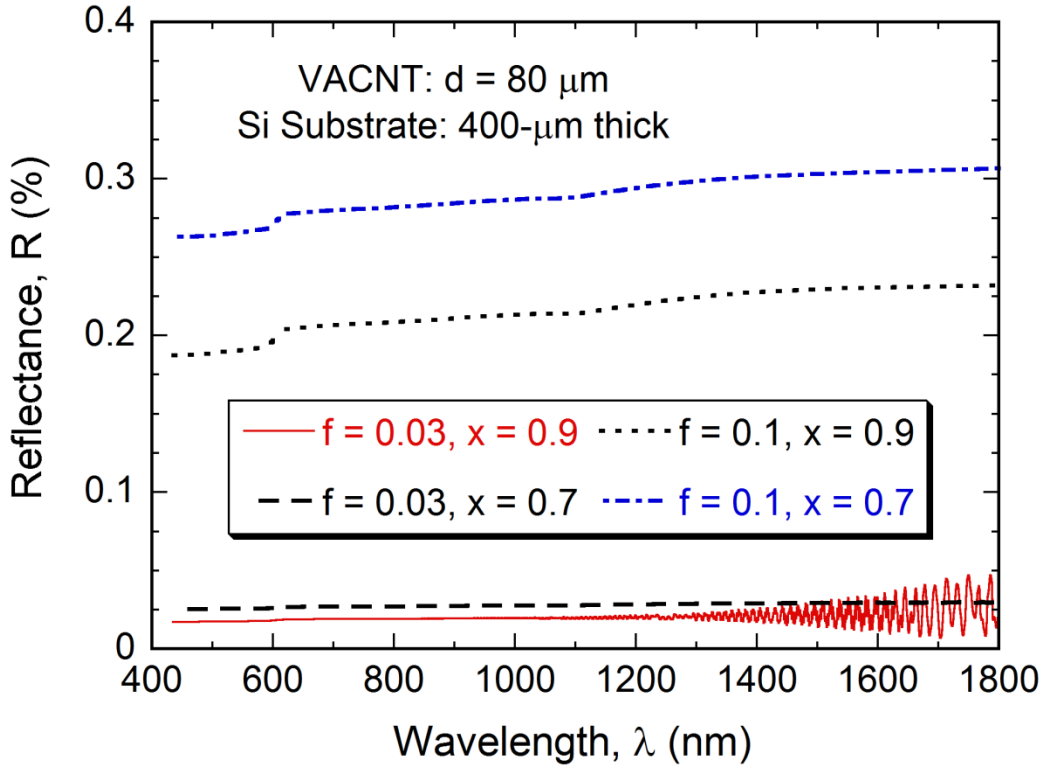

Figure 4.9 Spectral reflectance calculated from thin-film optics using the effective optical constants calculated from EMT for different f and x.

The general formulation for the reflectance calculation is to treat both the CNT carpet and silicon substrate as thin films [76]. The reflectance (R) spectra for several combinations of f and x are shown in Fig.4.9, assuming that the thickness of the VACNTs is 80 μm and the thickness of the silicon substrate is 400 μm. Note that the discontinuity around 600 nm is due to the tabulated optical constants. For f = 0.03 and x = 0.9, the radiation penetration depth of the CNT carpet is about 17 μm at λ = 1800 nm, resulting in some interference effect in the reflectance. However, the overall transmittance is still less

than 1%. For all other cases, $R = \rho_\lambda$. Clearly, larger *f* yields higher reflectance and, with the same *f*, larger *x* results in higher reflectance and smaller penetration depth. Note that the volume fraction for base-growth samples (#1, 2, and 3) is 2– 4% (Table 4.1). Comparing Fig. 4.9 with Fig. 4.5, it can be seen that the calculated reflectance is much lower than the measured. Furthermore, the calculated reflectance increases slightly at longer wavelength, while the measured spectra exhibit an opposite wavelength dependence due to the scattering from a rough surface.

As discussed earlier, scattering by rough surface, small particles including the CNT tips, and volumetric defects (such as misalignment) and nonuniformity may significantly alter the bidirectional distribution of the reflected light and the measured samples are more diffuse than specular. Hence, it can be concluded that scattering dominates the reflection and the reflection by the air-CNT carpet interface plays a minor role in the fabricated samples. The strength of Rayleigh scattering decreases with wavelength. This may be the reason why the measured reflectance decreases toward longer wavelengths. The EMT calculation suggests that further reduction of scattering and improvements in the sample quality can result in VACNT carpet with even higher absorptance in the visible and infrared.

4.4 Conclusion

In this chapter, the high absorptance (greater than 97%) in the visible and NIR regions is achieved by synthesizing multi-walled VACNTs on silicon substrates with TCVD method. For tip-growth dominant samples, a wide specular peak appears in the reflectance spectra at around λ = 600 nm due to metal impurities on top of the MWCNTs. For a base-growth sample with a CNT height of around 80 μm, the measured absorptance

exceeds 0.992 at wavelengths from 400 to 1800 nm. The polarization-dependent BRDFs at the wavelength of 635 nm reveal different scattering mechanisms of the MWCNT samples, including surface scattering (both specular and diffuse), small particle scattering (retroreflection), and volume scattering (forward scattering at large incidence angles). Modeling with EMT suggests that interface reflection is relatively small compared with light scattering; hence, further increase of the absorptance is possible if scattering by impurities and defects can be reduced. This study will facilitate promising applications of CNTs in energy conversion and thermal detectors.

CHAPTER 5

HIGHLY ABSORBING CARBON NANOTUBE ARRAYS: SPECULAR VS. DIFFUSE

While VACNT arrays with low effective refractive indices can have close-to-unity absorptance, so far the reported VACNT arrays have been essentially diffuse, including those six VACNT samples investigated in Chapter 4. In certain applications, such as blackbody cavities for absolute radiometry, radiation thermometry, and baffle design, specular black is often preferred over diffuse black [23,34]. This chapter reports a systemic investigation of VACNTs of high absorptance in the visible and near-infrared and with various surface features from nearly specular to highly diffuse. In addition, the specular VACNT sample allows the effective optical constants to be extracted from the specular reflectance measurements with a fitting method.

5.1 Sample Fabrication and Characterization

Multiwall VACNT specimens were synthesized on a 100-mm-diameter Si wafer using a thermal CVD technique by Dr. Cola's group with an Axitron Black Magic system. Figure 5.1 depicts the fabrication procedures and a photo of the Black Magic system with a PC monitor. The catalysts were made by coating a trilayer of 30-nm Ti, 10-nm Al, and 3-nm Fe in sequence [105]. Process gases were C_2H_2 and H_2 mixed at the flow rates of 100 and 160 sccm for Samples 1 and 3. While for Sample 2, the flow rates for C_2H_2 and H_2 gases were 100 and 700 sccm, respectively. N_2 was used as a carrier gas with variable flow rates. The growth pressure measured before the gas exit into the vacuum pump was 70 kPa for Samples 1 and 3, and 0.13 kPa for Sample 2. The growth time was 10 min for

Samples 1 and 2, and 2 min for Sample 3. The substrate temperature was maintained at 750°C during the CNT growth for all three samples.

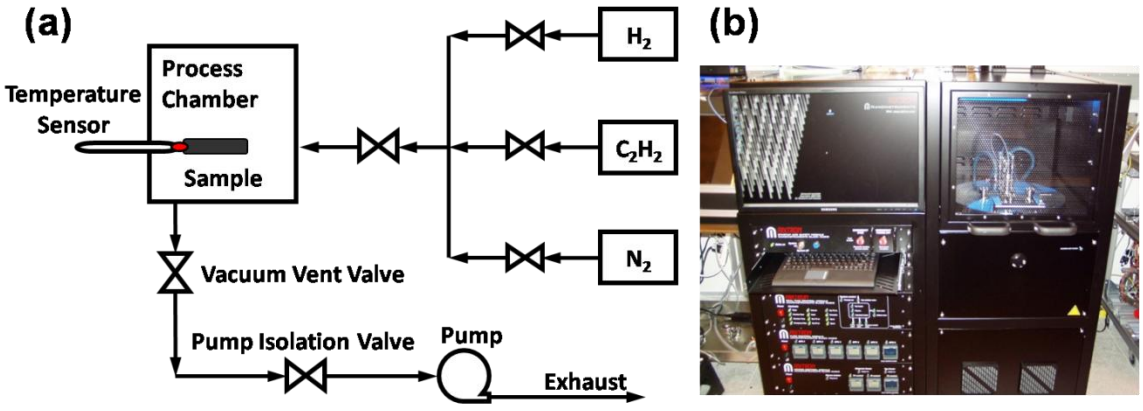

Figure 5.1 (a) Schematic of the VACNT sample fabrication procedures; (b) A photo of the Axitron Black Magic system.

The samples were diced into smaller pieces before the SEM imaging and IS measurements. For BRDF measurements, most samples were measured both before dicing and after dicing at similar locations on the sample and the repeatability of measurement results is within the uncertainty. Based on the SEM images, the average thicknesses of Samples 1 to 3 statistically estimated from random locations (around 40 locations for each sample) were approximately as 166 μm, 48 μm, and 34 μm, respectively. The density was obtained by weighing the mass of the CNTs using an analytic balance and measuring the covering areas of the substrates. The volume fraction, *f*, can be calculated by comparing the CNT array density to the graphite density which is taken as 2.2 g/cm^3. Table 5.1 lists the fabrication conditions as well as the parameters of each sample. From Table 5.1, the sample thickness is larger with a longer growth time but the relationship between thickness and growth time is not linear. In addition, when the growth time stays the same, pressure and gas flow rate of H_2 seem to affect the mass

of deposited CNTs. The uncertainties of density and volume fraction are estimated based on a 10% thickness uncertainty and 10% area uncertainty due to the somewhat irregular shape and the substrate is not fully covered with CNTs. The mass uncertainty is estimated less than 7% based on the instrument resolution. The relative uncertainty of density is around 15% mainly due to the uncertainties in thickness and area.

Table 5.1 Growth conditions and measured parameters for the CNT samples.

Sample #	Pressure (kPa)	Process Gas C_2H_2 : H_2 (sccm)	Growth Time (min)	Thickness (μm)	Density (g/cm^3)	f (%)
1	70	160 : 100	10	166 ± 16	0.067 ± 0.010	3.0 ± 0.5
2	0.13	100 : 700	10	48 ± 5	0.129 ± 0.019	5.9 ± 0.9
3	70	160 : 100	2	34 ± 3	0.190 ± 0.028	8.6 ± 1.3

Several SEM images of the fabricated VACNT arrays are depicted in Fig. 5.2. Figures 5.2(a) to 5.2(c) are side views of Sample 1 with the most specular surface imaged at different regions. From the low-magnification image of the entire array as shown in Fig. 5.2(c), it can be seen clearly that the CNTs of Sample 1 with an average thickness of around 160 μm are well aligned and very uniform. The high-resolution image of Sample 1 at the tip region demonstrates good alignment near the tip of the CNTs, as can be seen from Fig. 5.2(a). Figure 5.2(b) was taken from the middle region and some bending and entanglement of CNTs can be seen in the image. Due to the resolution limit of the SEM imaging, it is hard to distinguish the differences between individual samples based on the side view of the entire arrays; hence, only Sample 1 is selected as the representative.

However, the comparison of SEM images with similar magnification of Samples 1 and 2 with top surfaces viewed at an inclined angle shows certain different surface features.

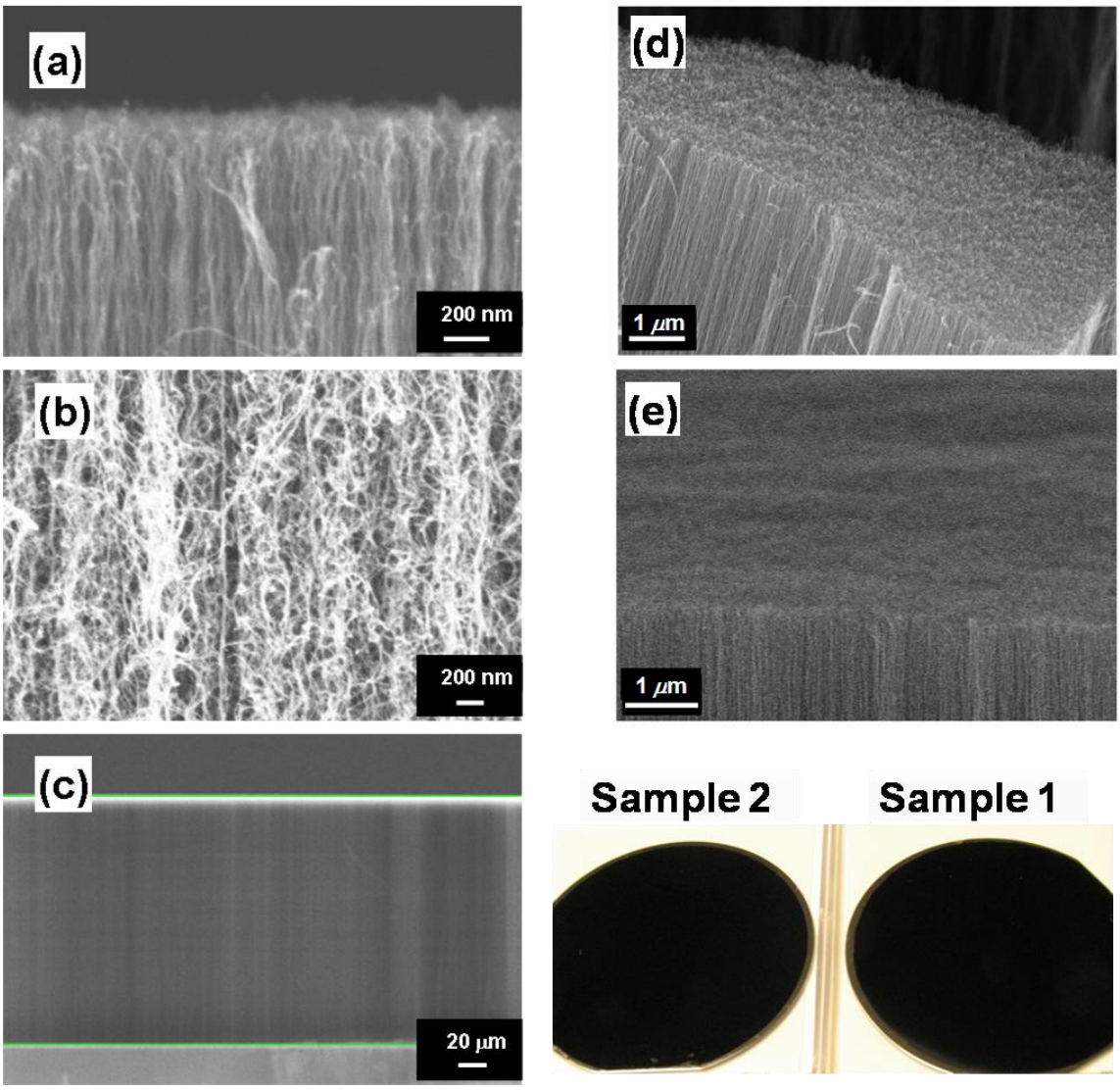

Figure 5.2 Representative SEM images: (a) Side view of Sample 1 for top region; (b) Side view of Sample 1 for middle region; (c) Side view of Sample 1 for the entire region; (d) Inclined view of Sample 1 whose side is well aligned and top is relatively smooth; (e) Inclined view of Sample 2 whose surface is less smooth. The scale bars correspond to different magnifications. The lower right corner shows two photos of Samples 1 and 2, respectively.

Figures 5.2(d) and 5.2(e) are inclined views near the top of Samples 1 and 2, respectively, with nearly the same magnification as indicated by the scale bars. Sample 1 has a fairly flat surface formed by the tube tips and the array is pretty uniform as shown by the edge. When Sample 2 is viewed from the side along the edge, the array uniformity is comparable with that of Sample 1. However, its surface appears cloudy and wavy over a large area, suggesting the surface of Sample 2 is relatively rough. Since the top view of Sample 3 with the same magnification has similar features as that of Sample 2, its images are not presented here. In addition, when these samples are examined by naked eyes, the surface of Sample 1 is shinny and displays different colors when the angle of observation is varied, which may be due to interference and diffraction effects caused by surface roughness, tip scattering, and optical anisotropy, though the exact reason needs further investigation; the surface of Sample 2 is dark color and not as smooth; the surface of Sample 3 is purely dark, diffuse, and nearly isotropic when tilted. The trend in appearance suggests that Sample 1 is more specular, presumably due to the better uniformity, smoothness, and alignment. Two photos of Samples 1 and 2 are presented in the lower right corner of Fig. 5.2 to visualize the purely black appearances of CNT samples, which is an indication of their close-to-unity absorptance.

5.2 Measurement Results and Discussions

5.2.1 BRDF for Comparison of Surface Features

The BRDF measurements were taken at the wavelength of λ = 635 nm for all three CNT samples with both polarizations. Here, only the in-plane measurements ($\phi_r = 0^o$ and 180^o) were considered; in other words, the movement of the sample detector

was confined within the POI as indicated by the dashed circle in Fig. 3.1. Similar to previous measurements of CNT samples, precautions were applied to reduce stray light and to improve the signal-to-noise ratio for low-level measurements [69,70].

The BRDF measurement results are plotted in Fig. 5.3, in which the ordinate with the same scale for all three samples is the product $f_r \times \cos\theta_r$, often called the cosine corrected BRDF in relevant publications. The cosine corrected BRDF is independent of θ_r for an ideal diffuse surface and can be viewed as proportional to the power that the sample detector received for given incidence power and solid angle. Since the interest of this study is to investigate the BRDF of the VACNT arrays near the specular peaks, only the forward reflectance were considered within a certain range of θ_r around the direction of specular reflection. The interval of θ_r was taken as 0.2^o near the specular reflection angle and 5^o for off-specular measurements. The incidence angles for BRDF measurements were set to be 0^o, 30^o, and 60^o corresponding to three curves of individual samples for one polarization. At normal incidence, the BRDFs within $\pm 3^o$ of the specular direction could not be measured due to the blockage of the incident beam by the sample detector. Therefore, to resolve the specular peak at normal incidence, θ_i was set to 4^o and the specular peak was shifted by 4^o in θ_r to match up with the off-peak BRDF at $\theta_i = 0^o$. On the other hand, BRDFs at normal incidence exhibit symmetry for both negative and positive reflection angles; and hence the average values of BRDFs measured within two ranges of θ_r from -80^o to -3^o and from 3^o to 80^o were used to present θ_r from 3^o to 80^o.

In order to reduce the random error, the collected signals were averaged over 30 measurements for each position. For the specular peaks in Sample 1, the standard

deviation is within 5%, but for very small BRDF values, the standard deviation of the 30 measurements can be as large as 30% due to the low signal-to-noise ratio. Additional uncertainty sources could arise from optical misalignment of the setup, stray light, and variation of illumination location due to sample nonuniformity. The overall uncertainty in the BRDF is estimated to be 10% near the specular peak when the corrected BRDF is higher than 10 sr^{-1}, but increases to 40% when the corrected BRDF is less than 0.001 sr^{-1} due to low signal-to-noise ratio and stray light.

As can be seen from Fig. 5.3, specular peaks with different magnitudes and sharpness exist for individual samples at all incidence angles and for both polarizations. For Sample 1, the corrected BRDF drops more than 5 orders of magnitude from the peak to the smallest values; while for Sample 2, the peaks are about one order of magnitude lower than those of Sample 1. As for Sample 3, the peaks at near normal incidence are obscure and these at oblique incidence are much lower and broader that those for Sample 2. The sharpness of specular peaks in BRDF for different samples is consistent with their appearance as shown in SEM images, indicating a increase of surface roughness from Samples 1 to 3. Also, the peak magnitudes are higher for *s* polarization than for *p* polarization for all samples; this is consistent with the reflection characteristics (i.e., Fresnel reflection) for a smooth interface. For Sample 3, the magnitudes of specular peak at $\theta_i = 0^o$ and 30^o are on the order of 10^{-3}, but suddenly increases by 2 orders of magnitude at $\theta_i = 60^o$, indicating the diffuse sample tends to be more specular at large incidence. This suggests that light scattering from these CNT samples is dominated by surface roughness and at larger incidence angles, the surface appears less rough.

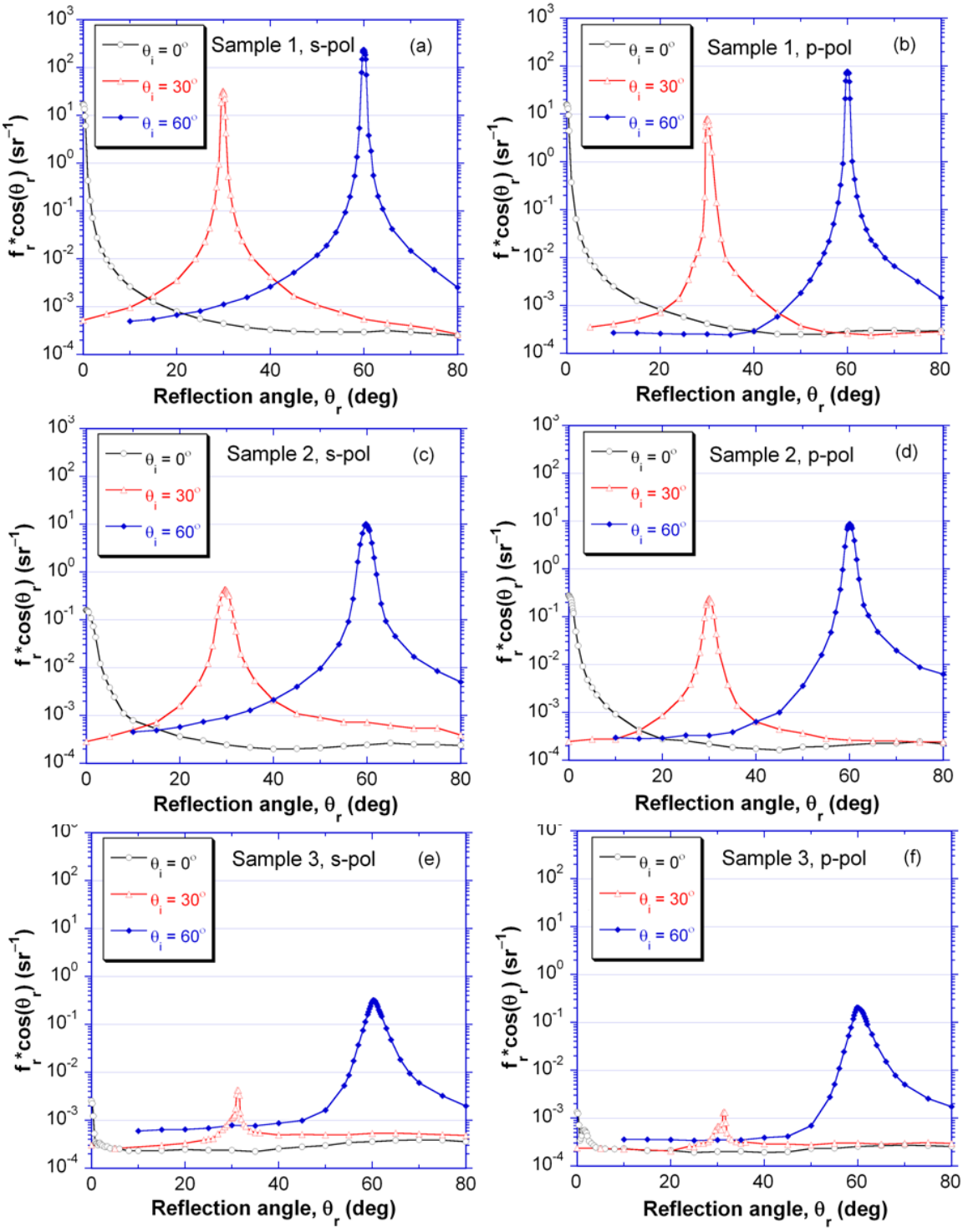

Figure 5.3 BRDFs measured at the 635-nm wavelength for all three samples at incidence angles of 0^{o}, 30^{o}, and 60^{o}. In the plots, "s-pol" and "p-pol" represent *s* polarization and *p* polarization, respectively. The specular peaks at normal incidence are obtained by shifting the measured BRDF at 4^{o} incidence angle.

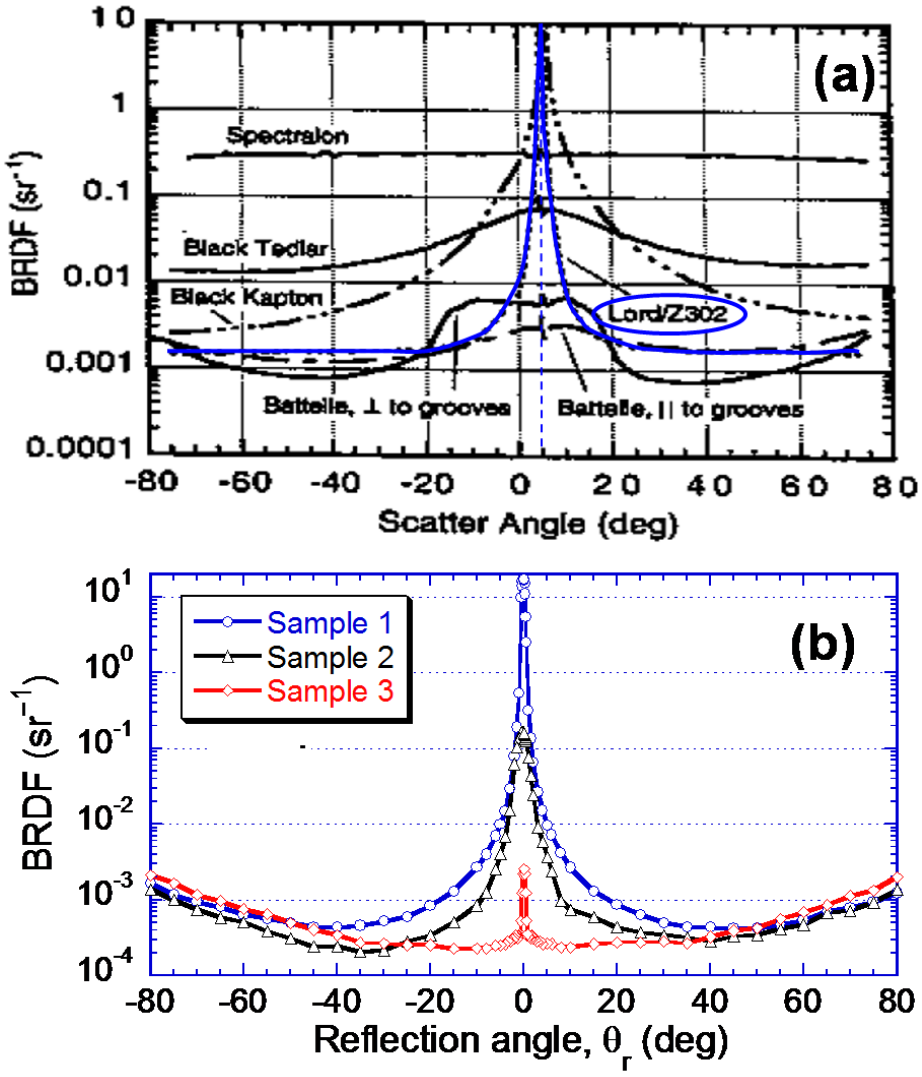

Figure 5.4 Comparison of specular blacks: (a) Lord/Z302 from Snail's work (highlighted with blue curves); (b) Specular CNT array of Sample 1 (blue curves with hollow circle markers). The BRDF plots are for *s* polarization. The incident wavelengths are 632.8 nm and 635 nm for Lord/Z302 and Sample 1, respectively; and the incidence angles are θ_i = 5° and normal incidence for Lord/Z302 and Sample 1, respectively.

At (near) normal incidence, the full width at half maximum of the specular peak for Sample 1 is less than 1°. In addition, within ± 2°, the BRDF of Sample 1 is reduced by 2 orders of magnitude from the peak value. The width and sharpness of BRDF for Sample 1 are comparable with those of Lord/Z302 (also known as Chemglaze Z302 or

Aeroglaze Z302), a typical specular black paint used in high-accuracy radiometers [106]. Figure 5.4 compares the BRDFs of Sample 1 (blue curves with hollow circle markers) and Lord/Z302 (solid blue curves) for *s* polarization as measured by Snail et al. [23]. The measurements of Lord/Z302 were done at the wavelength of 632.8 nm and at the incidence angle of 5^{o}, which were quite close to those used in the TAAS measurements. It is shown clearly that while the specular peaks of both Sample 1 and Lord/Z302 are comparable on both sharpness and magnitude, however, the BRDF for Sample 1 at large reflection (or scatter) angles is about a factor of 2 to 4 lower than that for Lord/Z302, suggesting that Sample 1 has an even lower reflectance or higher absorptance.

5.2.2 Directional-Hemispherical Reflectance

The IS was used to characterize the DHR of specular CNT samples from 400 to 1000 nm. Before measurements, the calibration and uncertainties of the IS with both the center-mount and back-mount configurations were verified again for accurate measurements of specular CNT samples. In an earlier study, calibration of the center-mount configuration was done with a silicon wafer, whose reflectance is greater than 50% [91]. For highly absorbing samples, however, a large portion of the optical energy that is multiply reflected by the sphere wall may be absorbed by the sample itself. The fraction that is absorbed may not be fully compensated between the background measurement and the sample measurement, since the sample orientation is different and the sample is neither ideally specular nor perfectly diffuse. It is found that a large sample (about 25×25 mm^2) would give a much lower reflectance. By reducing the sample size to approximately 18×18 mm^2, the measured reflectance was increased by 30% to 50%. The DHR measured with center-mount configuration using the diode laser is very close

to that obtained using the monochromator at the 635-nm wavelength. On the other hand, when the measurement is compared to that obtained with back-mount configuration using the diode laser, the measured reflectance is increased by 25% to 35%, which is closer to the DHR calculated by integrating the BRDF at normal incidence, under the assumption that the CNT samples are optically isotropic with respect to the azimuthal angle. However, it is difficult to focus the monochromator light to the sample in the back-mount configuration due to the limit of beam size in the current setup with the tungsten-halogen lamp as the light source. In addition, the back-mount configuration is subject to its own uncertainties; therefore, from the laser measurement and the standard deviations, it is estimated that the spectral DHR measurements have a relative uncertainty of 30%, which results in only 0.1% to 0.2% relative uncertainties in the absorptance ($\alpha = 1 - R_{dh}$) using Kirchhoff's law. The DHR and absorptance at the 635-nm wavelength obtained from both the integration of BRDFs at normal incidence and direct measurements with the IS are summarized in Table 5.2.

Table 5.2 R_{dh} and absorptance of three samples obtained using different methods at the wavelength of 635 nm.

Sample #	Center Mounting		Back Mounting		BRDF Integration	
	R_{dh} (%)	α (%)	R_{dh} (%)	α (%)	R_{dh} (%)	α (%)
1	0.42	99.58	0.58	99.43	0.64	99.36
2	0.16	99.84	0.20	99.80	0.21	99.79
3	0.10	99.90	0.13	99.87	0.18	99.82

Figure 5.5 shows the spectral R_{dh} measurements from 400 to 1000 nm for samples with reduced sizes using the center-mount configuration. The laser measurement results

using back-mount configuration are shown as markers for comparisons in Fig. 5.5. The error bars for 30% relative uncertainty are labeled at three wavelengths of 500, 700, and 900 nm for different samples. Since the spectral resolution is very high (10 nm interval in wavelength), the spectral R_{dh} values measured with the monochromator are shown as continues curves instead of individual markers.

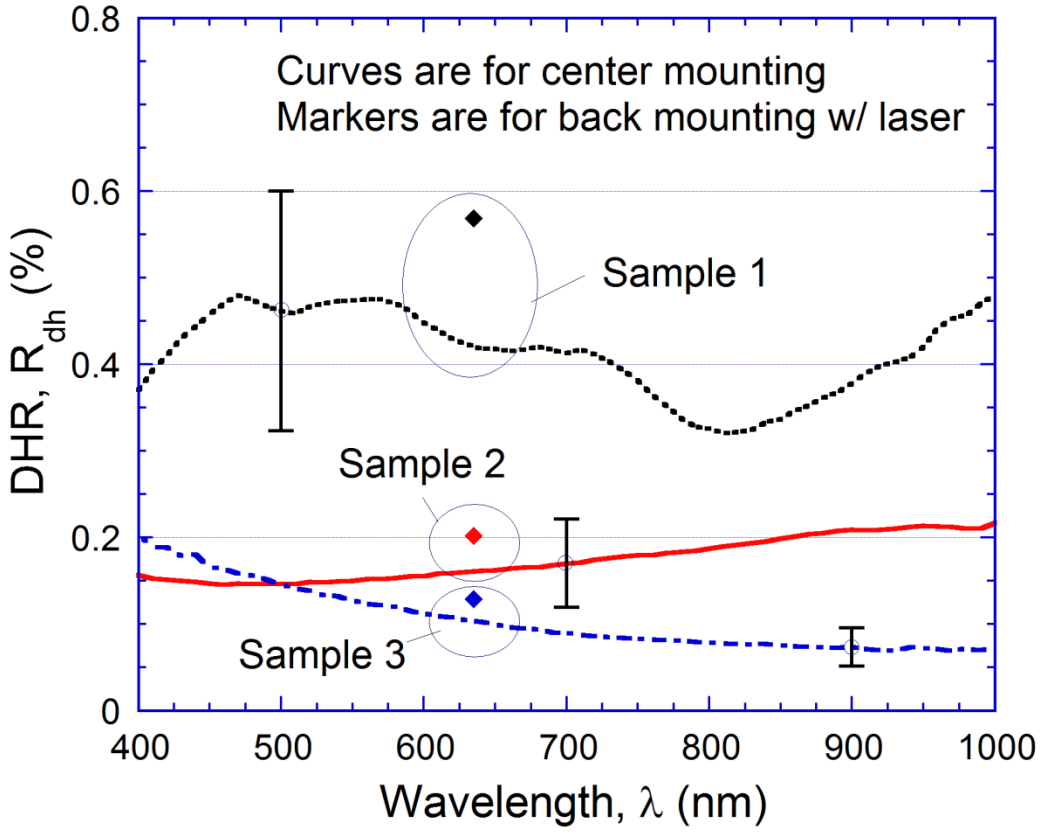

Figure 5.5 Spectral DHR measured using the integrating sphere with center-mount configuration (curves) and back-mount configuration (markers). The sample was cut to about 18 × 18 mm^2 in size to compensate the difference in the sample signal and background signal. The error bars represent an expended uncertainty of 30%.

Within the measured spectral region, Sample 3 has the lowest reflectance ranging from 0.0007 to 0.002, followed by Sample 2 whose R_{dh} ranges from 0.001 to 0.002. On the other hand, Sample 1 has the highest R_{dh}, ranging from 0.003 to 0.005. R_{dh} for Sample 1 exhibits some interference fringes, which are attributed to the density variation near the

tip of the CNTs, within 1-2 μm thickness near the surface of the CNT array. Such a thin layer can be treated as a thin film with different refractive index from the lower portion of CNT array which acts as a semi-infinite medium, hence interference may occur. This density variation was previous observed, and explained with a collective mechanism for the evolution and termination of CNT growth as discussed by Bedewy et al.[107]. However, similar phenomenon does not exist for Samples 2 and 3 due to the reduction of coherence when light gets reflected by rougher surfaces [76]. The interference effect also contributes to the glossy and colorful appearance of the surface of Sample 1 as seen by naked eyes. It is worth noting that R_{dh} for Sample 3 tends to decrease as wavelength gets longer; this may be due to the fact that scattering by roughness becomes weaker at longer wavelength [70,83]. Other effects such as the change of the effective refractive index and the effective surface roughness may also play a role. The trend for Sample 2 is not as distinguishable, but R_{dh} slightly increase with wavelength as opposite to that for Sample 3.

5.2.3 Angle-Resolved Specular Reflectance

The specular reflectance, R_{sp}, was measured with the TAAS by setting the sample detector at the position of $\theta_r = \theta_i$, and can be related to BRDF by $R_{sp} = f_r \cos\theta_r \Delta\Omega_r$. It should be noted that the laser beam diameter is approximately 3 mm as measured at the illumination area on the sample, which is much smaller than the detector aperture whose diameter is 8 mm. This allows the specularly reflected power to be fully captured by the signal detector. In general, the measurements were taken at various incidence angles from 5^o to 80^o with an interval of 5^o, however, the resolution was increased when the incidence angle is getting closer to the Brewster angle for *p* polarization to fully present the dip feature. The measurements (markers) and theoretical calculation (curves) for both

Samples 1 and 2 with two polarizations are shown in Fig. 5.6. Sample 3 was not measured since it is hard to distinguish the specularly reflected energy from the scattered energy due to its large surface roughness. The specular reflectance is plotted in logarithmic scale so that the extremely small reflectance at the Brewster angle for both samples with *p* polarization can be easily differed. For Sample 1 with the smallest surface roughness, while the specular reflectance increases monotonically with θ_i for *s* polarization, it reaches a minimum for *p* polarization. The incidence angle at which the specular reflectance is minimal is defined as the Brewster angle of 44°. Notice that the Brewster angle between two isotropic media must be greater than 45° for incidence from the optically rarer medium. At the Brewster angle, the specular reflectance can be as small as 0.0001. While for Sample 2 with a less specular surface, the dip around the Brewster angle is rather broad and the trends of reflectance plots for both *s* and *p* polarizations are very similar, indicating the reflected light from Sample 2 becomes less coherent due to the rougher surface.

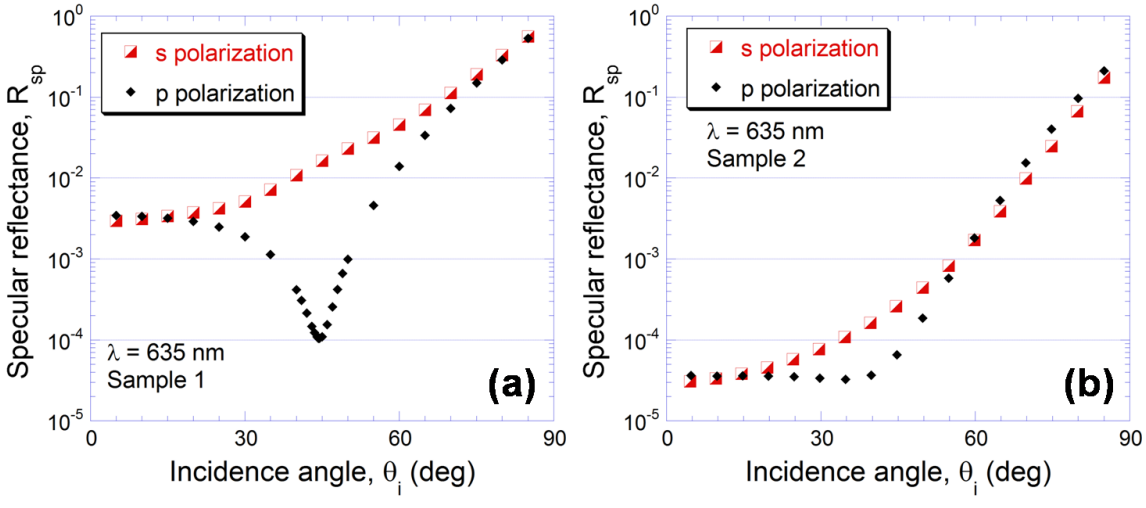

Figure 5.6 Specular reflectance measurements with the TAAS at the wavelength of 635 nm and at various incidence angles: (a) Sample 1 with the most specular surface; (b) Sample 2 with a less specular surface.

5.3 Theoretical Modeling for Effective Optical Constants

As mentioned previously, the CNT array may be treated as an effectively homogenous and uniaxial medium, whose optical constants are described by two complex refractive indices, $n_{\text{eff}}^{\text{O}} = n_{\text{O}} + ik_{\text{O}}$ for ordinary waves and $n_{\text{eff}}^{\text{E}} = n_{\text{E}} + ik_{\text{E}}$ for primary extraordinary waves. For a special case that the optical axis **c** of the VACNT array is perpendicular to the sample surface, the tilting angle of β is 90°. By treating the CNT layer as a semi-infinite medium and setting β = 90°, Eqs. (2.28) and (2.35) can be utilized to calculate the reflectance at the air-VACNT interface for *s* and *p* polarizations, individually. Note that when the incident medium 1 is isotropic air with $\varepsilon_{1\text{O}} = \varepsilon_{1\text{E}} = 1$, the surface admittance and surface impedance of medium 1 are $Y_1 = -\left(k_0/\omega\mu_0\right)\cos\theta_{\text{i}}$ and $Z_1 = \left(1/\omega\varepsilon_0\right)\cos\theta_{\text{i}}$. Correspondingly, Eqs. (2.28) and (2.35) can be reorganized as below with the modification of surface roughness effect [108,109]:

$$R_{\text{s,sp}} = \left(\frac{\cos\theta_{\text{i}} - \sqrt{\left(n_{\text{eff}}^{\text{O}}\right)^2 - \sin^2\theta_{\text{i}}}}{\cos\theta_{\text{i}} + \sqrt{\left(n_{\text{eff}}^{\text{O}}\right)^2 - \sin^2\theta_{\text{i}}}} \right)^2 C_{\text{sp}}, \qquad \text{for } s \text{ polarization} \qquad (5.1)$$

and

$$R_{\text{p,sp}} = \left(\frac{n_{\text{eff}}^{\text{O}} n_{\text{eff}}^{\text{E}} \cos\theta_{\text{i}} - \sqrt{\left(n_{\text{eff}}^{\text{E}}\right)^2 - \sin^2\theta_{\text{i}}}}{n_{\text{eff}}^{\text{O}} n_{\text{eff}}^{\text{E}} \cos\theta_{\text{i}} + \sqrt{\left(n_{\text{eff}}^{\text{E}}\right)^2 - \sin^2\theta_{\text{i}}}} \right)^2 C_{\text{sp}}, \text{ for } p \text{ polarization} \qquad (5.2)$$

Note that the only difference of Eqs. (5.1) and (5.2) as compared with Eqs. (2.28) and (2.35) is the specularity parameter $C_{\text{sp}} = \exp\left[-16\pi^2\sigma_{\text{rms}}^2\cos^2(\theta_{\text{i}})/\lambda^2\right]$, or simply called specularity, which takes into account of the surface roughness effect. The total reflectance as expressed by Eqs. (2.28) and (2.35) without the specularity modification

should be for a perfectly smooth surface only; however, by introducing the specularity, the left-handed sides of Eqs. (5.1) and (5.2) become the specular components of the total reflectance from a surface with moderate roughness. The specularity is based on the first-order approximation of Rayleigh scattering, which is valid when the roughness characteristic length is much smaller compared with the incident wavelength [83].

To determine the effective optical constants for both polarizations, a direct fitting based on the least-squares method is applied to find the minimal relative difference between the reflectance values from the model calculation and the TAAS measurements. First, the objective function as a link of both calculation and measurement is defined as:

$$F = \sqrt{\frac{1}{N}\sum_{j=1}^{N}\left(\frac{R_{\text{cal},j} - R_{\text{meas},j}}{R_{\text{meas},j}}\right)^2} \tag{5.3}$$

where subscripts "cal" and "meas" stand for calculated and measured, j denotes the number of the data point for each incidence angle, and N is the total number of measurements. Second, $n_{\text{eff}}^{\text{O}}$ and σ_{rms} are treated as adjustable parameters with individual ranges as initial values, and are substituted into Eq. (5.1) to calculate the specular reflectance at each incidence angle used in the specular reflectance measurement for *s* polarization. The calculated $R_{\text{s,sp}}$ and measured specular reflectance with the TAAS are plugged into the objective function. Mapping the initial ranges of $n_{\text{eff}}^{\text{O}}$ and σ_{rms} to get the smallest value of the objective function, which in turn determines the optimized values of $n_{\text{eff}}^{\text{O}}$ and σ_{rms}. Third, the fitted $n_{\text{eff}}^{\text{O}}$ and σ_{rms} are used along with Eq. (5.3) to minimize the objective function for *p*-polarized reflectance following similar procedures for *s* polarization in order to obtain $n_{\text{eff}}^{\text{E}}$.

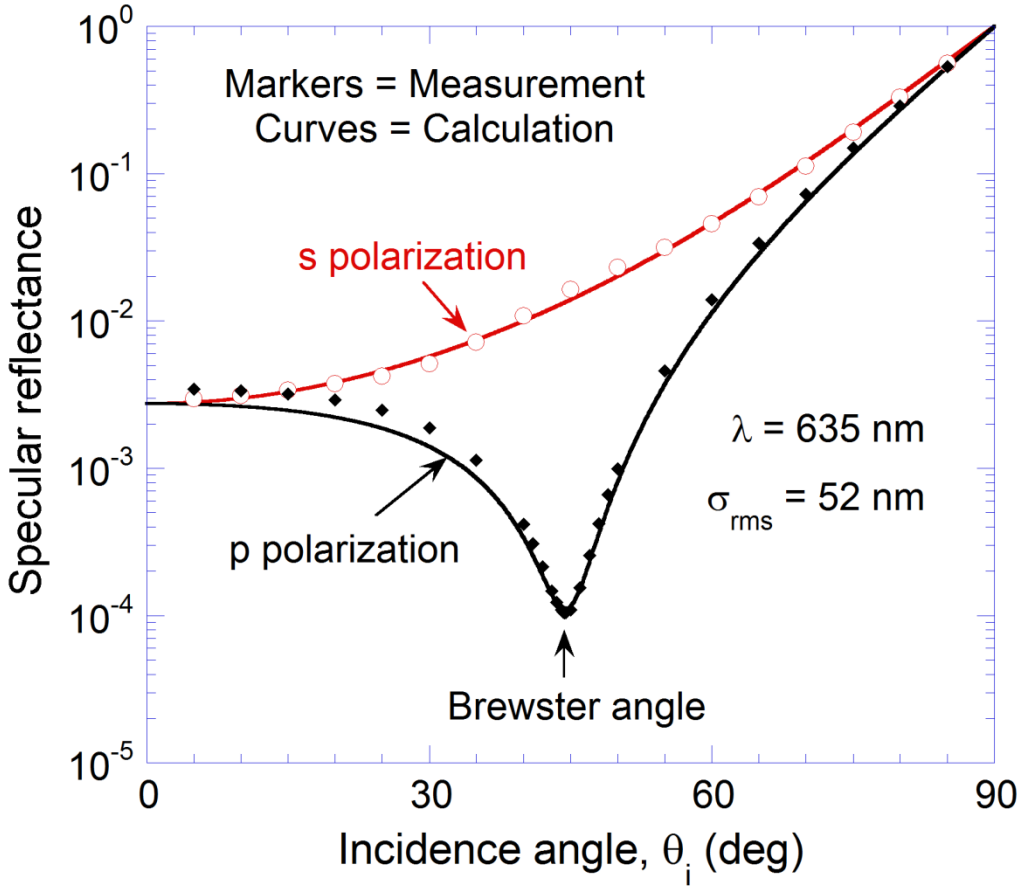

Figure 5.7 Measured and calculated (with best fitted parameters) specular reflectance versus incidence angle for both polarizations. The Brewster angle is around 44°, which is less than 45° as the lower limit of incidence from air to an optically isotropic medium.

The best fitting gives the smallest objective function, F_{min} = 7% for *s* polarization and F_{min} = 15% for *p* polarization. To estimate the uncertainties of the fitted effective optical constants, a 10% variation of F_{min} for *s* polarization and 20% variation of F_{min} for *p* polarization are added to their original values and used as the new optimized values of the objective function. The corresponding ranges of the effective optical constants are used as individual uncertainties. The values obtained from fitting are n_O = 1.19±0.03, k_O=0.043±0.009, n_E = 1.33±0.08, k_E = 0.03±0.01, and $\sigma_{rms} = 52 \pm 10$ nm. The specular reflectance values calculated with the best fitted values of the effective optical constants

for both polarizations and surface roughness are plotted as a function of incidence angles, which is depicted in Fig 5.7. Excellent agreements between measurements and theoretical calculations are obtained, especially on the Brewster angle locations.

In addition, Atomic force microscopy (AFM) was used to obtain the surface profile of the specular CNT array, and the root-mean-square roughness was found to be $\sigma_{\text{rms}} = 57$ nm with a scanning area of 10 μm × 10 μm and $\sigma_{\text{rms}} = 61$ nm with a scanning area of 25 μm × 25 μm. Hence, the average values of surface roughness measured from AFM fall within the uncertainty range of σ_{rms} from fitting. It should be noted that the parameter C_{sp} increases with θ_{i} and varies from 0.35 at $\theta_{\text{i}} = 0°$ to 0.90 at $\theta_{\text{i}} = 72°$ with σ_{rms} = 52 nm as the best fitted value. Based on the extinction coefficients from fitting, the optical penetrate depth of the specular CNT layer is less than 2 μm, which is much smaller than the average thickness of the CNT array. Hence, it is appropriate to treat the CNT array as a semi-infinite medium.

The EMT has also been used to explain the low refractive index of CNT arrays. While the values of optical constants obtained by fitting fall in the range predicted by EMT, it is difficult to quantitatively predict $n_{\text{eff}}^{\text{O}}$ and $n_{\text{eff}}^{\text{E}}$ using EMT because the misalignment and nonuniformity of the CNT arrays and the lack of knowledge of the inherent dielectric function and structure of the multiwall CNTs. Since it is difficult to nail the dip location of the Brewster angle for Sample 2 due to the less coherent features of the reflected light caused by a larger surface roughness, the direct fitting method was applied to Sample 1 only. Furthermore, by assuming the specular CNT array is optically isotropic with respect to the azimuth direction, the integration of BRDFs at normal

incidence gives the directional-hemispherical reflectance to be 0.0064 ± 0.0026, which agrees reasonably well with R_{dh} = 0.0058 ± 0.0018 as measured with the IS using the back-mount configuration at λ = 635 nm.

5.4 Conclusion

In summary, the optical properties of three vertically aligned multi-walled CNT arrays with different surface features from specular to diffuse are examined by measuring the BRDFs at the wavelength of 635 nm and the DHR within the wavelength region from 400 to 1000 nm. Specular peaks with different magnitudes and widths are observed from the measured BRDFs. The sharpness of the peak around the specular direction indicates the surface roughness variation of the CNT samples from nearly specular to highly diffuse. The high absorption of the CNT samples is demonstrated by the near unity (0.995–0.999) absorptance obtained from the DHR measurements. The specular CNT array is attributed to the excellent alignment and sample uniformity and its ordinary and extraordinary optical constants are quantitatively obtained through a direct fitting for individual polarizations. This study not only suggests a method for determining the anisotropic optical constants and surface roughness of VACNT, but also opens up opportunities in applying VACNT arrays with specular surfaces to absolute radiometry and space-borne spectrometry.

CHAPTER 6

ANGLE-RESOLVED PROPERTIES OF INCLINED SILVER NANORODS ON SILVER FILM

In this chapter and subsequent chapters, we are interested in the anisotropic radiative and optical properties of the second type of the 2D confined nanostructures, inclined AgNRs deposited on different substrates, including glass slides with Ag films and CD templates. The inclined AgNRs have recently been reported to be highly anisotropic, with either metallic or dielectric characteristics, and have various applications [52,61,110,111]. So far, related studies have been focused on the anisotropic reflection and/or transmission, whereas diffraction and scattering from anisotropic AgNR arrays are still lacking. Therefore, in this chapter, AgNRs were grown on flat substrates consisting of 1-mm thick glass slides with Ag films. The anisotropic reflectance of inclined AgNR arrays was characterized at the wavelengths of 635 and 977 nm. The specular reflectance at various incidence angles and the BRDFs at normal incidence were measured with the TAAS. The AgNR array is modeled as an effectively homogenous and optically uniaxial thin film and analyzed with the EMT to elucidate the dielectric or metallic response. The well-known thin-film optics formulation is modified to include optical anisotropy and roughness scattering. By comparison of the calculated results with experiments, the anisotropic optical constants and polarization-dependent effective roughness of the AgNR array are determined. On the other hand, due to the structural inhomogeneity, scattering by nanorods is expected to play a significant role, giving rise to complicated effects including both surface and volume scattering, as well as diffraction

[81,82,112,113]. Hence, discussions on the scattering features of AgNR arrays are also presented in this chapter.

6.1 Sample Preparation and Characterization

The samples of inclined AgNRs deposited on a thin Ag film were fabricated by Dr. Zhao's group at the University of Georgia using an OAD method inside a custom-designed electron-beam evaporation system, which is a physical vapor deposition technique to produce aligned nanorod arrays with high yield and controllable structural parameters [42]. Figure 6.1 shows a schematic of the OAD method. Unlike the conventional metal film deposition, in which the substrate is usually placed horizontally facing down the deposition source, the substrate in OAD is rotated to a large angle with respect to the deposition vapor. Due to a geometric shadowing effect caused by the oblique deposition angle, the random nucleation islands from the initial deposition act as shadowing centers to form metallic nanorods [114,115]. A 1-mm-thick glass slide was used as the substrate on which the AgNRs were deposited. Commercially available Ag (99.999%) and Ti (99.995%) pellets were used as source materials for the thin-film and nanorod deposition. A quartz crystal microbalance directly facing the source material was used for monitoring the deposition rate. Prior to the AgNR growth, a 20-nm Ti adhesive layer was deposited onto the glass substrate, followed by a 500-nm Ag film. For the Ti and Ag film deposition, the substrate was placed horizontally facing down the deposition source, then the substrate was rotated by 86^{o} for the growth of nanorods. Due to the geometric shadowing effect induced by the large vapor incidence angle, the random nucleation centers act as shadowing seeds that result in a preferable growth of the

nucleation centers towards the incident vapor, ultimately forming an array of tilted nanorod structures [114,115] .

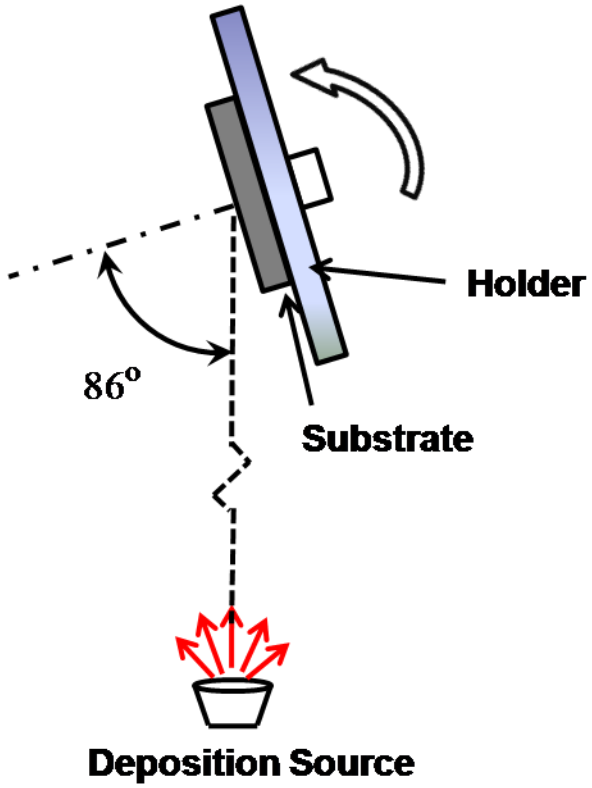

Figure 6.1 Schematic of the OAD setup.

Two SEM images of the top and cross-section views of the obliquely aligned AgNR array are shown in Figs. 6.2(a) and (b). Statistical estimation over 50 AgNRs from the SEM images gives the average length *L*, diameter *D*, and tilting angle β with respect to the substrate surface normal to be $L = 1550 \pm 350$ nm, $D = 100 \pm 30$ nm, and $\beta = 70 \pm 6^{o}$, respectively. The average gap between two adjacent rods (center to center) is approximately 250 ± 50 nm, giving a volume filling ratio *f* (the ratio of the volume occupied by rods to the total array volume) between 0.15 and 0.30. The SEM images suggest that the shapes of the AgNRs are not perfectly cylindrical. The formed AgNRs

exhibit somewhat irregular shapes, such as needles, corrugations, bifurcations, and fusions. However, these imperfections may not be very sensitive to the incident light since the dimensions of the irregular shapes are rather small compared with the laser wavelength. Overall, the samples are fairly smooth and the reflected/scattered light is largely along the specular direction (to be discussed later).

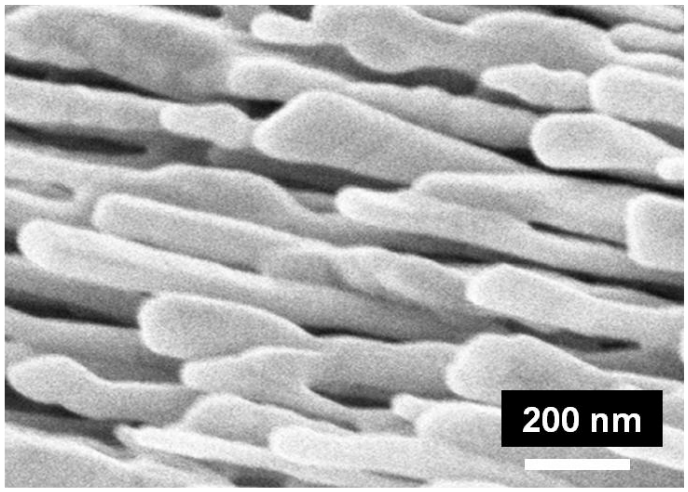

(a) Top view

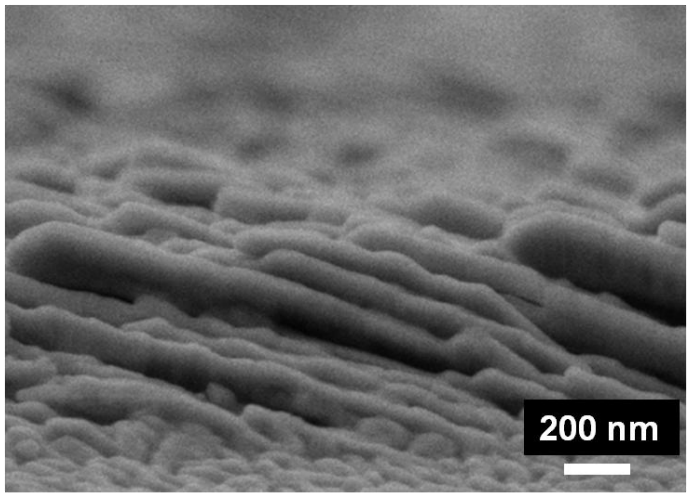

(b) Side view

Figure 6.2 SEM images of the AgNRs: (a) Top view; (b) Side view showing the oblique alignment. The tilting angle is estimated to be $\beta = 70 \pm 6°$ from substrate surface normal. The average length and diameter are L = 1550 ± 350 nm and D = 100 ± 30 nm, respectively.

As far as the material's stability, while Ag does not get oxidized easily in air, silver sulfide (Ag_2S) can form if the sample is exposed in air for an extensive duration. The AgNRs make the contact area much larger than a flat Ag film and get darker after 3-5 weeks. When the sample is stored in a sealed glass container, it can last 4-6 months or longer without changing the color. All the measurements were carried out before the AgNR sample changes color. Hence, the effect of silver sulfide can be neglected.

6.2 Angle-Resolved Reflectance, BRDF, and DHR Measurements

The TAAS was used to measure the BRDF and angle-resolved specular reflectance [89]. Two laser diodes at wavelength λ = 635 and 977 nm were used interchangeably to provide a collimated and stable light source. For BRDF measurements, only the in-plane measurements at normal incidence are considered for AgNR-on-Ag film Samples. In other words, the movement of the sample detector is confined within the POI, following the dashed black circle as indicated in Fig. 3.1. In general, the BRDF for an isotropic material at normal incidence is independent of polarization. However, due to the anisotropy of the AgNR array, the BRDF depends on the polarization even at normal incidence. The sample was measured in two different orientations by rotating the sample with respect to its surface normal by 90º as shown in Fig. 6.3. Note that the incident beam points toward the positive *z* axis. Orientation 1 corresponds to the case that the sample surface is in the *x*-*y* plane and the optical axis **c** of the AgNR array, which is parallel to the rod, lies in plane of incidence (*x*-*z* plane). For Orientation 2, **c** is neither parallel nor perpendicular to the plane of incidence; rather, it lies in the *y*-*z* plane. Incident waves with *s* (or *p*) polarization correspond to the case when the electric field (or magnetic field) is perpendicular to the plane of incidence.

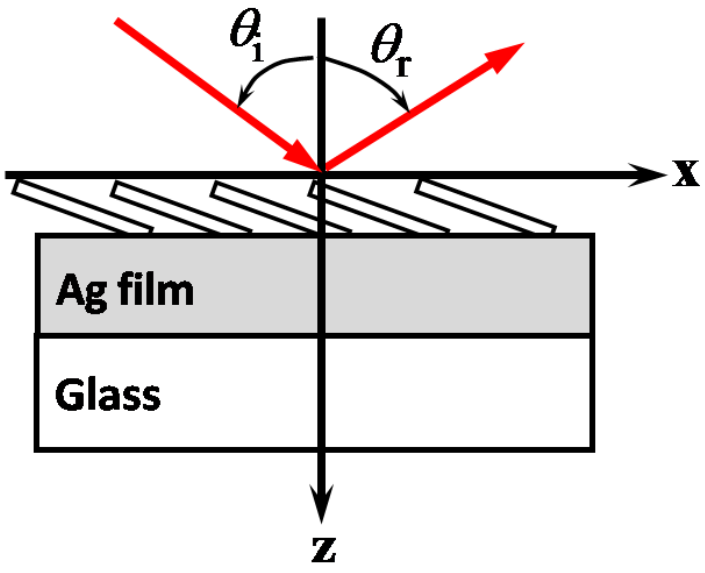

(a) Orientation 1

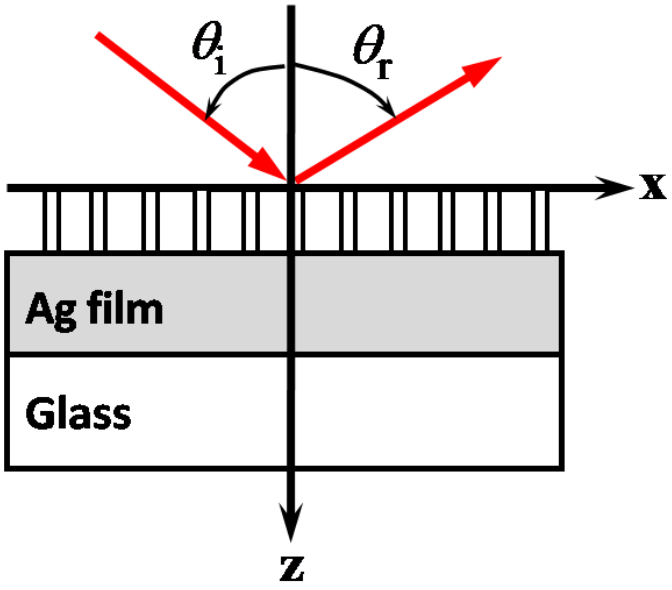

(b) Orientation 2

Figure 6.3 Schematic of the sample loading orientations: (a) Orientation 1 corresponds to the case when the optical axis of AgNR array lies in plane of incidence; (b) Orientation 2 corresponds to the case when the sample loaded with Orientation 1 is counterclockwise rotated along the *z*-axis by 90^{o}.

The specular reflectance, R_{sp}, were measured by positioning the signal detector at the specular direction with $\theta_r = \theta_i$. Note that the specular reflectance is related to the BRDF by $R_{sp} = f_r \cos\theta_r \Delta\Omega_r$. It should be noted that the laser beam diameter is approximately 3 mm, which is much smaller than the detector aperture whose diameter is 8 mm. This allows the specularly reflected power to be fully captured by the signal detector. The overall uncertainty for the specular measurement is estimated to be 5%; whereas for BRDF, the uncertainty becomes larger for lower signals.

The DHR measurement was performed at 635 nm with the IS with the back-mount configuration [93]. To measure the directional-hemispherical reflectance, the integrating sphere was rotated by 3^o (near normal incidence) to prevent the specularly reflected light from escaping through the entrance port. The reflectance of the sample is obtained by correcting the ratio of the sample signal and the reference signal with the reflectance of the PTFE reference, which is 0.988 in the spectra of interest [104]. Details on the instrumentation of DHR measurements are presented in Chapter 3. The overall relative uncertainty of the integrating sphere measurement is estimated to be 10%.

6.3 Measurement Results and Discussion

6.3.1 BRDF Measurement

Figure 6.4 depicts the measured BRDF of the AgNR-on-Ag film sample for both polarizations at normal incidence and 635-nm and 977-nm wavelengths. It should be noted that the specular peak at 4^o incidence is taken as the normal incidence value (by ignoring retroreflection) since the BRDF within $\pm 3^o$ of the specular direction cannot be measured due to the blockage of the incident beam by the signal detector.

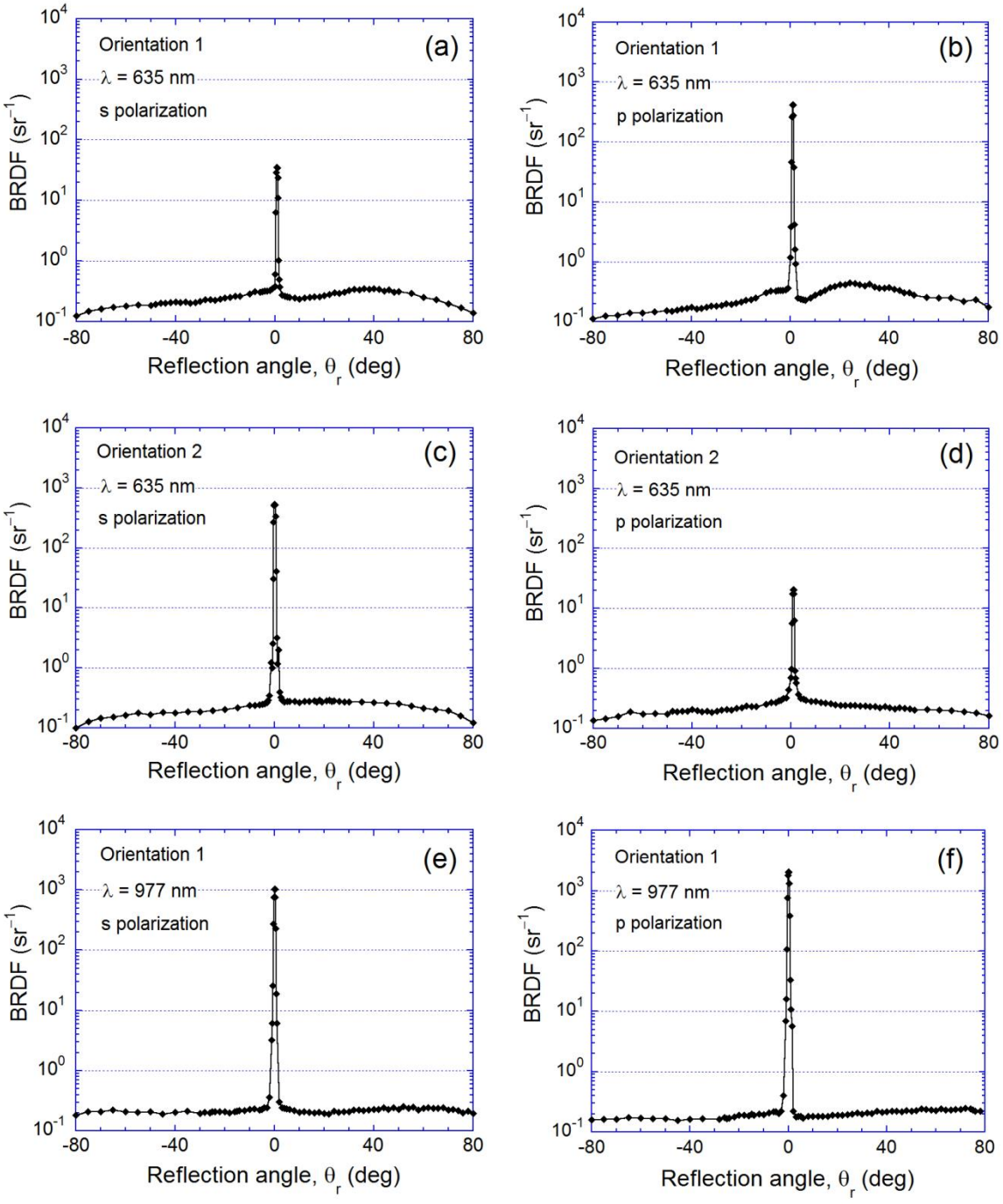

Figure 6.4 Measured BRDFs of the AgNR array at the wavelengths of 635 and 977 nm for both polarizations. AgNRs tilt to the negative *x*-axis for Orientation 1 and are projected to the positive *y*-axis for Orientation 2.

The range of θ_r extends from -80^o to 80^o, where the negative sign is used when θ_r is on the same side as the incident beam. At normal incidence with Orientation 1, *s* polarization (or *p* polarization) corresponds to ordinary (or extraordinary) wave propagation in the AgNR array with the electric (or magnetic) field perpendicular to the rods. Because Orientation 2 is rotated by 90º, *s* and *p* polarizations correspond to extraordinary and ordinary waves, respectively. Due to the oblique alignment of rods, the AgNR array exhibits anisotropic responses regarding different polarizations with a dielectric behavior for ordinary waves and a metallic behavior for extraordinary waves. This anisotropy can be seen clearly from Fig. 6.4, where the magnitudes of specular peaks associated with ordinary waves are one order of magnitude lower than those associated with extraordinary waves. In general, the surfaces exhibit specular peaks, suggesting that the roughness and inhomogeneity scale should be much smaller than the wavelength.

Another noticeable feature of the BRDF plots is the bump at 635 nm with Orientation 1, which exists for both polarizations at θ_r from 20^o to 40^o. Note that in this case AgNRs are tilted towards negative θ_r. The bumps are presumably due to a combined effect of diffraction and scattering from the AgNR surface for *p* polarization, since the AgNR layer is essentially opaque. For *s* polarization, bulk inhomogeneity can also play a role. The location of the bump suggests a characteristic spatial period on the order of the AgNR length. Due to the small magnitude and relative flatness of the bump, the diffraction effect will not be further analyzed. It should be noted that the bump does not show up in the BRDF plots at λ = 977 nm, since the sample surface tends to be smoother at longer wavelengths. The resulting scattering is essentially incoherent.

Furthermore, the magnitudes of the specular peaks at 977 nm are higher than those at 635 nm due to the smaller optical roughness and inhomogeneity at longer wavelengths. In addition, the BRDF plots for Orientation 2 are nearly symmetric. This is because the optical axis **c** is perpendicular to the *x*-axis for Orientation 2 and the incidence is normal to the surface. The slight asymmetry may be caused by the irregular shape of individual AgNRs and imperfect alignment of the nanorods.

6.3.2 Specular Reflectance and DHR

The measured specular reflectance is plotted in Fig. 6.5 at incidence angles from 5^{o} to 75^{o} for Orientation 1 at both wavelengths, except for λ = 977 nm with *p* polarization. In this case, the incidence angle is extended to 78^{o} to illustrate the dip around 75^{o}. Note that the incident beam is parallel to the rod at $\theta_{i} = \beta = 70^{o}$. Due to the anisotropic responses of the AgNR array, specular reflectance for *s* polarization (dielectric behavior) is expected to be smaller than that for *p* polarization (metallic behavior). However, this is only true at smaller incidence angles. At large incidence angles, the reflectance for *p* polarization tends to drop at the principal angle [76]. Furthermore, the angle between the electric field and the optical axis **c** varies with θ_{i}, which makes the metallic behavior less prominent for large incidence angles. For *s* polarization, interference plays an important role in the reflectance. Moreover, surface roughness affects the specular reflectance differently for different polarizations and incidence angles. A detailed analysis of the specular reflectance is deferred to Section 6.4.

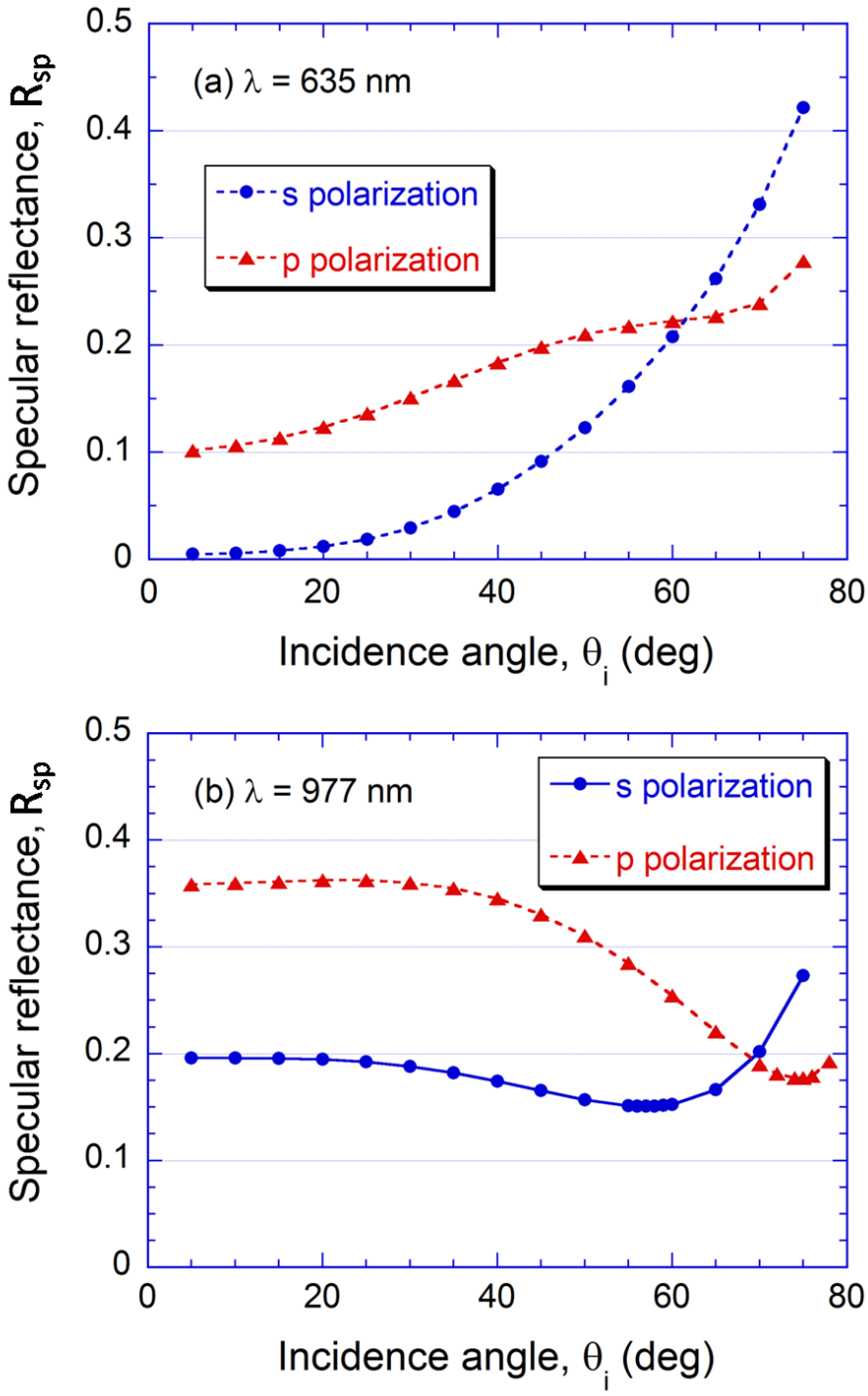

Figure 6.5 Angle-resolved specular reflectance measured for both polarizations with Orientation 1: (a) λ = 635 nm; (b) λ = 977 nm. Note that *s* or *p* polarization corresponds to ordinary or extraordinary wave propagation in the AgNR layer.

The directional-hemispherical reflectance was measured for Orientation 1 at the wavelength of 635 nm. The results are $R_{dh} = 0.67$ for *s* polarization and $R_{dh} = 0.81$ for *p* polarization. Higher R_{dh} value is obtained for the metallic behavior than for the dielectric behavior. Similarly, using the exponential relation described in Chapter 5, when the surface roughness is much smaller than the wavelength, the specularity can be calculated by [71,116]

$$C_{sp} = \frac{R_{sp}}{R_{dh}} = \exp\left[-\frac{16\pi^2\sigma^2\cos^2\theta_i}{\lambda^2}\right] \tag{6.1}$$

where σ is the surface roughness and λ is the wavelength in vacuum. In Eq. (6.1), the specular reflectance is for normal incidence. Using the specular reflectance measured at θ_i = 4°, the values of σ = 113 and 77 nm are calculated from Eq. (6.1) for *s* and *p* polarizations, respectively. The larger roughness for *s* polarization may be attributed to the bulk inhomogeneity, resulting in a polarization-dependent roughness parameter. Again it should be noted that Eq. (6.1) is only a first-order approximation. When volume scattering is included, σ should be viewed as a lumped roughness parameter, rather than the root mean square roughness of the surface of the AgNR layer. More sophisticated theory on light scattering is needed to model the combined surface scattering and volume scattering problems [81,82,112]. However, for simplicity, Eq. (6.1) is used in the analysis to model the angle-resolved specular reflectance, similar to the previous work on carbon nanotube arrays [71], as presented in the subsequent section.

6.4 Theoretical Modeling

The purpose of the analysis presented in this section is to develop a theoretical model that can describe the angle- and polarization-dependent specular reflectance of the

AgNR sample, which is represented by the three-layer system along with Eqs. (2.39) to (2.44) as described in Chapter 2.

6.4.1 Three-Layer Model for AgNR-on-Ag Film Samples

For the theoretical modeling, only Orientation 1 is considered here since polarization coupling exists for Orientation 2, making the analysis much more complex for oblique incidence due to the tilting direction. At 635- or 977-nm incidence, the skin depth of bulk silver is calculated to be approximately 12 and 11 nm using Palik's data [87]; therefore, the 500-nm Ag film is thick enough to be treated as optically opaque. Correspondingly, the three-layer model is essentially a uniaxial medium of the AgNR layer with a thickness of $d_2 = L \times \cos\beta$ = 530 nm, sandwiched between two semi-infinite media of air and bulk Ag. The dielectric property of the AgNR layer is described by a dielectric tensor of $\overline{\overline{\varepsilon}}_2$ as expressed by Eq. (2.23) in Chapter 2, in which, the angle β between the optical axis **c** and the *z*-axis is the same as the tilting angle of nanorods characterized by the SEM image. Figure 6.6 depicts the structure of the three-layer model and indicates the anisotropic reflectance and transmittance coefficients at each interface. Phase matching conditions require that the wavevector k_x is the same regardless of the medium. Note that for *p* polarization, the magnitudes of k_{2z}^{+} and k_{2z}^{-} in medium 2 are different except for normal incidence. Hence, at the interface between media 2 and 3, the reflection and incidence angles are not the same, as illustrated by the wavevectors $\mathbf{k}_2^{+}$ and $\mathbf{k}_2^{-}$ in Fig. 6.6(c). As mentioned previously, the + or – sign signifies forward or backward propagation, respectively.

For Orientation 1 used in specular reflectance measurements with **c** lying in plane of incidence, ordinary and extraordinary waves are decoupled and they correspond to *s* and *p* polarizations, respectively [53]. For a plane wave incident with *s* polarization, the electric field is always perpendicular to the optical axis. The waves inside the AgNR layer behave the same as those in an isotropic medium with an effective dielectric constant $\varepsilon_{\text{eff}}^{\text{O}}$. For *p* polarization, however, extraordinary waves exist in the AgNR layer. In this case, the reflectance and transmittance coefficients must be modified following the formulation presented in Chapter 2.

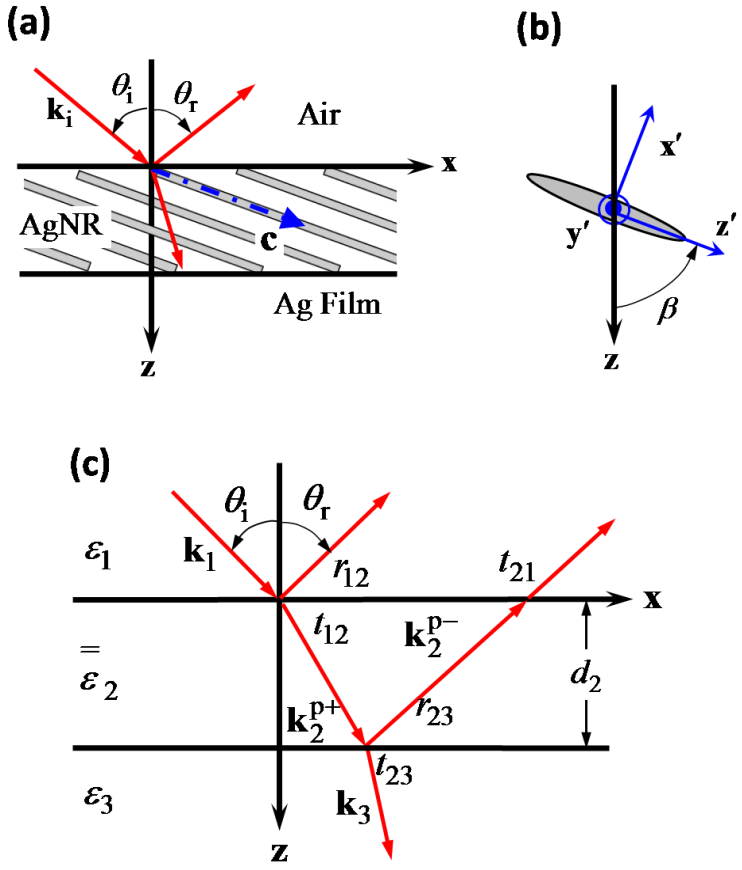

Figure 6.6 Schematic of wave propagation inside a three-layer system with the middle layer being uniaxial: (a) A three-layer system; (b) A prolate-spheroid-shaped AgNR; (c) Wave propagation in the three-layer system, showing the wavevector in each layer, and the reflectance and transmittance coefficients at each interface.

Considering the three-layer model as depicted in Fig. 6.6(c), reflectance and transmittance for *s* polarization can be easily calculated using thin-film optics for isotropic media with ordinary dielectric function or optical constants; whereas for *p* polarization, the formulation needs to be modified. By matching the tangential amplitudes for both the electric and magnetic fields at the air-AgNR and AgNR-Ag interfaces, Eq. (2.40) of the surface impedances used to calculate the reflectance and transmittance coefficients for TM polarization with plane incident waves from air ($\varepsilon_1 = 1$) to the AgNR/Ag system can be simplified as [51,53]:

$$Z_1 = \frac{E_{1x}}{H_{1y}} = \frac{k_0 \cos\theta_\mathrm{i}}{\omega\varepsilon_0} \tag{6.2a}$$

$$Z_2^+ = \frac{E_{2x}}{H_{2y}} = \frac{k_0}{\omega\varepsilon_0}\frac{\sqrt{\varepsilon_{zz} - \sin^2\theta_\mathrm{i}}}{n_{2\mathrm{O}} n_{2\mathrm{E}}} \tag{6.2b}$$

$$Z_3 = \frac{E_{3x}}{H_{3y}} = \frac{k_0}{\omega\varepsilon_0}\frac{\sqrt{n_3^2 - \sin^2\theta_\mathrm{i}}}{n_3^2} \tag{6.2c}$$

where, $n_{2\mathrm{O}}^2 = \left(n_\mathrm{O} + \mathrm{i}\kappa_\mathrm{O}\right)^2 = \varepsilon_\mathrm{eff}^\mathrm{O}$ and $n_{2\mathrm{E}}^2 = \left(n_\mathrm{E} + \mathrm{i}\kappa_\mathrm{E}\right)^2 = \varepsilon_\mathrm{eff}^\mathrm{E}$ are the effective complex refractive indices of medium 2 (AgNR layer) corresponding to ordinary and primary extraordinary waves. $n_3^2 = \varepsilon_3$ is the complex dielectric constant of medium 3 (the Ag film) and is taken from Palik [87] by interpolation. Note that the *z*-component of the wavevector in medium 1 or 3 is $k_{1z} = \sqrt{k_1^2 - k_x^2} = k_0\cos\theta_\mathrm{i}$ or $k_{3z} = k_0\sqrt{n_3^2 - \sin^2\theta_\mathrm{i}}$, respectively. Substitution of Eqs. (6.2a) to (6.2c) into Eqs. (2.38), (2.39), (2.42), and (2.44), the angle-resolved reflectance can be calculated at various incidence angles for both polarizations.

6.4.2 Determination of Effective Optical Constants with Fitting

It should be noted that reflectance calculated from the anisotropic wave propagation in uniaxial media described above is for smooth surfaces only. By multiplying the specularity defined in Eq. (6.1), the model reflectance can be converted to the specular reflectance of a rough surface by assuming $\sigma \ll \lambda$. Similarly as in the specular CNT work presented in Chapter 5, the dielectric function and corresponding optical constants of the AgNR layer can be obtained by a least-squares method to find the minimal relative difference between measured and calculated specular reflectance, as described by the objective function [71]:

$$F = \sqrt{\frac{1}{N}\sum_{j=1}^{N}\left(\frac{R_{\mathrm{cal},j} - R_{\mathrm{meas},j}}{R_{\mathrm{meas},j}}\right)^2} \tag{6.3}$$

where subscripts "cal" and "meas" stand for calculated and measured specular reflectance, and N is the total number of data points. Notice that the reflectance for *s* polarization depends on ordinary optical constants only, and reflectance for *p* polarization depends on both ordinary and extraordinary properties. Therefore, the fitting is applied for *s* polarization first to determine $n_{2\mathrm{O}}$ and σ (for *s* polarization). Then, $n_{2\mathrm{O}}$ is fixed and the reflectance for *p* polarization is fitted to determine $n_{2\mathrm{E}}$ and σ (for *p* polarization). As mentioned previously, different roughness parameters are used for different polarizations and wavelengths in order to obtain the least F.

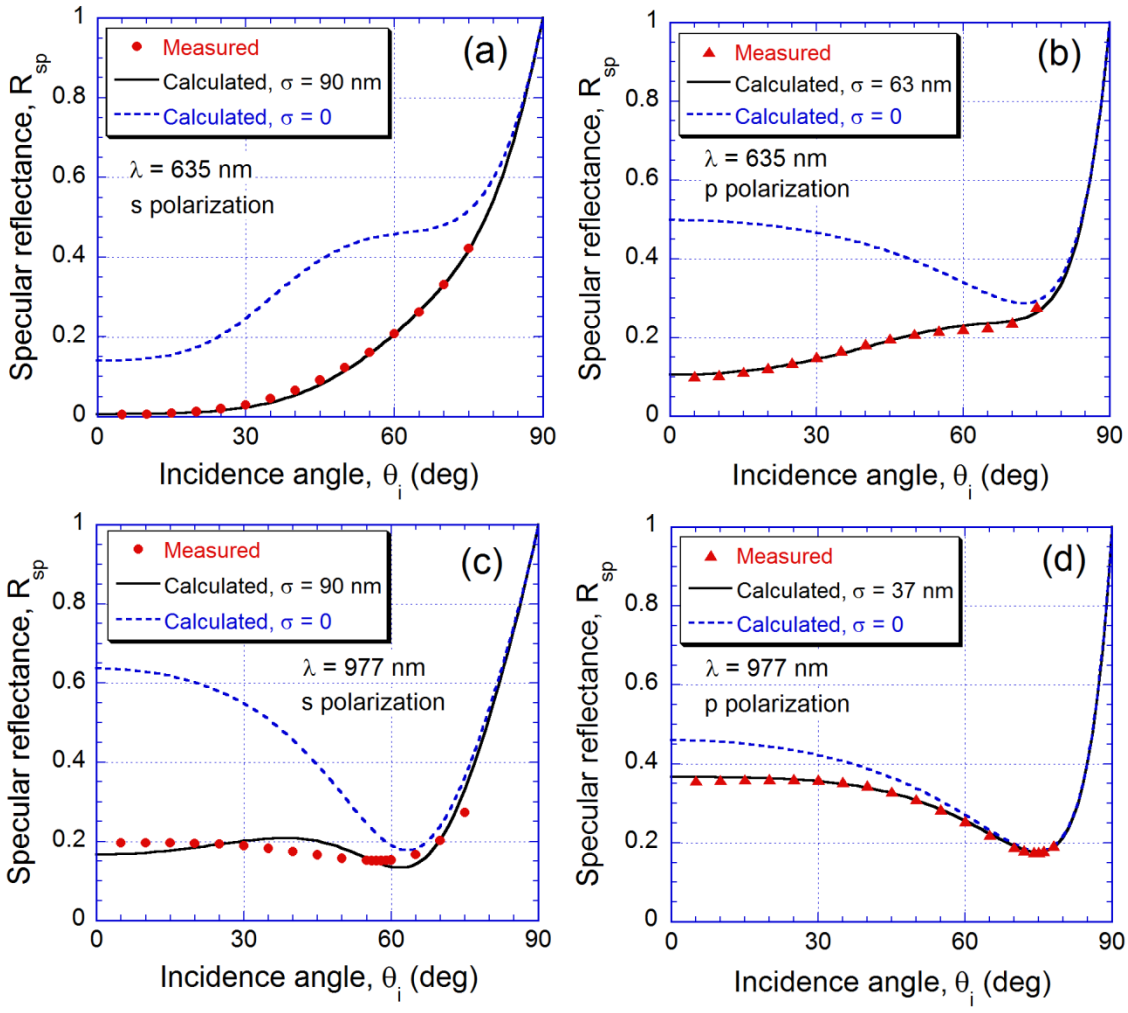

Figure 6.7 Comparison of the specular reflectance measured from TAAS and that calculated with the best fitted parameters. In the calculation, the thickness of AgNR array is fixed at 530 nm based on L = 1550 nm and β = 70°. The best fitted optical constants for both polarizations and wavelengths are summarized in Table 6.1.

The agreement between fitting and experimental results is shown in Fig. 6.7 for comparison. Note that the measurement results are the same as those shown in Fig. 6.4. The calculation without roughness is shown as dotted line in Fig. 6.7. Without introducing roughness in the model, the calculated reflectance is much higher than the measured, especially at smaller incidence angles. Hence, roughness is needed in order to fit the measured specular reflectance. For *s* polarization, the interference effect modifies

the angular-dependent reflectance significantly, although the feature becomes less distinct in experiments due to roughness. For *p* polarization, the principal angle can be clearly seen in the measured reflectance at λ = 977 nm but the measured reflectance at 635 nm exhibits almost monotonic increase with the incidence angle. This is again caused by roughness as shown in Fig. 6.7(b). With the exception of Fig. 6.7(c), the fitted reflectance agrees well with the measured values.

The roughness parameter obtained from the fitting is σ = 90 nm for *s* polarization at both wavelengths. This is 20% smaller than the previously calculated value of 113 nm based on the ratio of the measured R_{sp} and R_{dh}. For *p* polarization at λ = 635 nm, σ = 63 nm, which is 18% smaller than that based on the measured specularity C_{sp}. The difference of about 20% is anticipated due to the uncertainties in the fitting and experiments. However, for *p* polarization at λ = 977 nm, the fitted σ = 37 nm is much smaller. It should be reiterated that the use of specularity is only a first-order approximation, and the scattering mechanism cannot be simply described by the small-roughness surface scattering model.

The values and the uncertainty of the fitted ordinary and extraordinary optical properties are summarized in Table 6.1 at both wavelengths. For *s* polarization, the best fitting corresponds to the smallest *F* of 14% at 635 nm and 12% at 977 nm; while for *p* polarization, the best fitting gives *F* as 4% at 635 nm and 2% at 977 nm. The larger *F* for ordinary waves is attributed to the interference effect at the AgNR-Ag film interface, which induces phase change not considered by the simple roughness model. The fitting uncertainty is estimated according to the experimental uncertainty by relaxing each parameter until the objective function *F* deviates appreciably from the optimal value. A

10% increase for *s* polarization and 30% increase for *p* polarization of the objective function with respect to the smallest *F* result in the relative variation ranges of n_O, κ_O, n_E, and κ_E to be 3%, 30%, 5%, and 15% (with respect to the best fitted values), respectively; this indicates that the ordinary extinction coefficient κ_O is more sensitive to the fitting compared with other optical constants. The dielectric behavior (ordinary) when $\kappa << n$ and the metallic behavior (extraordinary) when $n < \kappa$ can be clearly seen. The uncertainty of the fitted Table 6.1 also shows the predicted optical constants based on the EMT theory to be discussed in the next section.

Table 6.1 Comparison of the optical constants of the inclined AgNR array obtained from specular reflectance fitting and the EMT predictions at λ = 635 and 977 nm. The optical constants of bulk silver are taken from Palik [87]. For λ = 635 nm, the values are n = 0.135 and κ = 4.01; for λ = 977 nm, the values are n = 0.206 and κ = 6.59.

λ (nm)		n_O	κ_O	n_E	κ_E
635	Fitting	1.41±0.04	0.06±0.02	0.59±0.03	1.62±0.24
	MG	1.34	0.004	0.09	1.97
	BR	1.70	0.05	0.075	1.76
	MG*	1.33	0.03	0.89	1.94
	BG*	1.51	0.14	0.74	1.79
977	Fitting	1.58±0.05	0.03±0.01	1.10±0.06	2.17±0.33
	MG	1.31	0.001	0.20	3.98
	BR	1.48	0.005	0.11	3.12
	MG*	1.31	0.01	1.81	3.59
	BG*	1.46	0.034	1.05	3.13

* Calculated by increasing *n* of bulk silver by a factor of 10.

6.4.3 Determination of Effective Optical Constants with the EMT

In order to check the reasonableness of the fitted optical constants, the EMT described in Chapter 2 is used to estimate the ordinary and extraordinary dielectric functions of the AgNR array. The original equation of the EMT, Eq. (2.3) in Chapter 2 should be modified with $\varepsilon_a = \varepsilon_{\mathrm{Ag}}$ and $\varepsilon_b = \varepsilon_{\mathrm{air}}$, in which $\varepsilon_{\mathrm{Ag}}$ are the dielectric function of bulk Ag at 635 and 977 nm taken from Palik [87]. f is the volume filling ratio of AgNRs, and g is a depolarization factor that depends on the array geometry and polarization. The modified equation represents the Bruggeman, BR, approximation when the host is the effective medium ($\varepsilon_{\mathrm{h}} = \varepsilon_{\mathrm{eff}}$) or the Maxwell-Garnett, MG, approximation when the host is air ($\varepsilon_{\mathrm{h}} = \varepsilon_{\mathrm{air}}$) [117]. Detailed discussions about two approximations are provided in Chapter 2. For the MG approximation, the effective dielectric function of the AgNR layer can be expressed in an explicit form as presented by Eq. (2.9). For the BR effective medium approximation, a quadratic equation given in Eq. (6.4) below needs to be solved and the physically meaningful solution for which $\mathrm{Im}(\varepsilon_{\mathrm{eff}}) \geq 0$ should be taken.

$$(1-g)\varepsilon_{\mathrm{eff}}^2 + B\varepsilon_{\mathrm{eff}} - g\varepsilon_{\mathrm{Ag}} = 0 \tag{6.4}$$

where $B = (g-f)\varepsilon_{\mathrm{Ag}} - (1-f-g)$. For prolate-spheroid-like AgNRs as shown in Fig. 6.5(b), the depolarization factor g depends on the principal crystal direction is perpendicular (ordinary, along x' or y') or parallel (extraordinary) to the optical axis, which can be calculated using Eqs. (2.6) and (2.7) along with the geometric parameters of the nanorods. While the calculated values of $g_{\mathrm{O}} = 0.4949$ and $g_{\mathrm{E}} = 0.0102$ for the AgNR structure is close to the values of $g_{\mathrm{O}} = 0.5$ and $g_{\mathrm{E}} = 0$ for a infinitely long cylinder, the

resulting effective dielectric function can have some difference in some cases. In the EMT modeling, the filling fraction *f* is chosen to be 0.25.

The optical constants predicted from both the MG and BR approximations are also listed in Table 6.1 for both wavelengths and polarizations. For simplicity, only the refractive index and extinction coefficient are listed. Note that the dielectric constant can be easily calculated from $\varepsilon = (n^2 - \kappa^2) + \mathrm{i}2n\kappa$. The trends of dielectric behavior (ordinary) and metallic behavior (extraordinary) can be seen in the optical constants predicted by both EMT approximations. While the differences between the two EMT approximations and the fitted values are relative small for n_O and κ_E, the disagreement in κ_O or n_E can be more than an order of magnitude. For example, at λ = 635 nm, the fitted κ_O = 0.06, which agrees with the value of 0.05 predicted by the BR approximation, but the value of 0.005 predicted by the MG approximation is an order of magnitude smaller. On the other hand, at λ = 977 nm, both EMT approximations predict a much smaller κ_O than the fitted value.

Considering the inhomogeneity in the nanorods, which may resulting in increased loss and scattering rate of the electrons [117], the EMT is also calculated by increasing the *n* value of bulk silver by a factor of 10. This gives the same effect as in the free electron model by increasing the scattering rate. The calculated optical constants are also shown in Table 6.1 and marked with MG* and BR*. The resulting n_E and κ_O are very close to the fitted value. While EMT is a useful tool, there are variations between the EMT models. The irregular shapes and entanglement of the AgNRs may challenge the applicability of the EMT. Furthermore, accurate determination of the parameters to be used in the EMT such as the filling ratio, the geometry, and the optical properties of

nanostructured metal are also difficult. On the other hand, the fitting method presented in the preceding section based on the anisotropic thin-film optics and angle-resolved specular reflectance is a convenient way of estimating the anisotropic optical constants of the AgNR layer. The resulting optical constants are consistent with those predicted by the EMT approximations, while the quantitative values may be somewhat different.

6.5 Conclusion

In this chapter, the anisotropic responses of the AgNR array to different polarizations were experimentally demonstrated through the BRDF and angle-resolved specular reflectance measurements. By incorporating roughness effect in a modified thin-film optics formulation considering anisotropic dielectric function, the theoretical analysis elucidates the dependence of dielectric (ordinary) versus metallic (extraordinary) behaviors of the AgNR array on the sample orientation, incidence angle, and polarization. The anisotropic AgNR array can be treated as an effectively homogenous layer with polarization-dependent optical constants obtained by fitting the measured angle-resolved specular reflectance. The optical constants obtained from the fitting method are consistent with the EMT predictions. This work will not only facilitate the applications of AgNR arrays in polarization-dependent optical and photonic devices, but also offer a simple approach to determine the optical constants of anisotropic thin films.

CHAPTER 7

DIFFRACTION OF INCLINED SILVER NANORODS ON CD

This chapter focuses on the anisotropic diffraction from a novel hybrid micro-nanoscale structure comprised of inclined AgNRs on a CD template. The reflectance values of individual diffraction peaks were measured with the TAAS and further compared with the values predicted from the RCWA calculation. The anisotropic diffraction is explained by the dielectric versus metallic behaviors of the inclined AgNR arrays corresponding to ordinary and extraordinary wave propagation.

7.1 Sample Fabrication and Characterization

7.1.1 Sample Fabrication by Oblique Angle Deposition

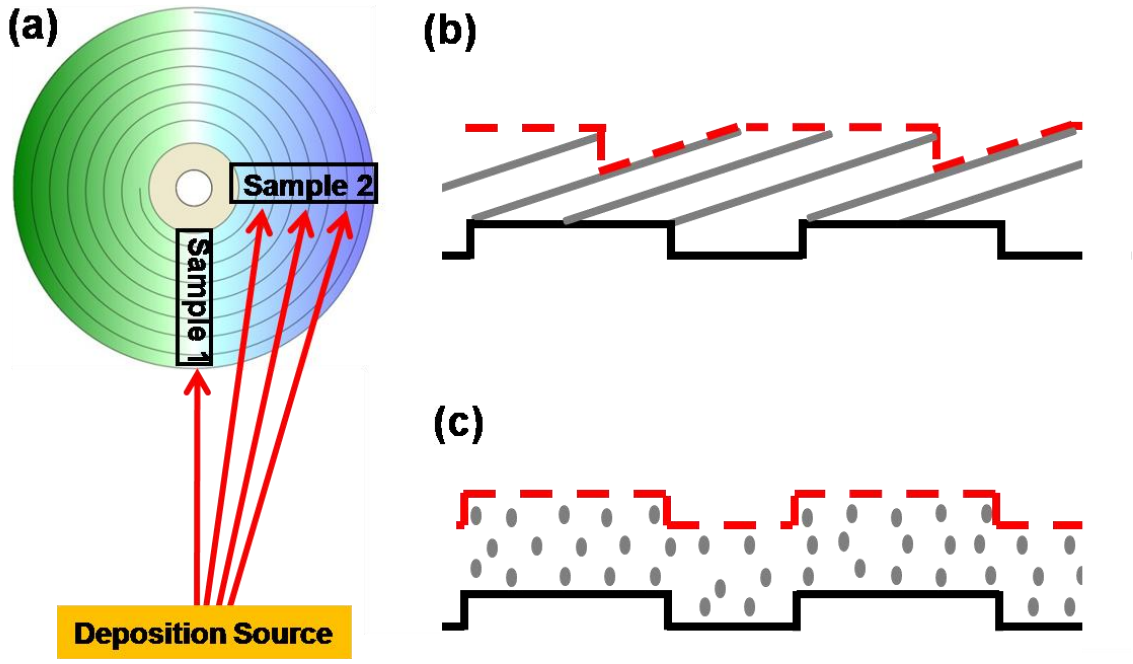

Figure 7.1 (a) Locations of Samples 1 and 2 with respect to the CD substrate (not to scale); cartoons showing the cross-sectional profiles of the effective grating formed by AgNRs: (b) Sample 1; (c) Sample 2.

The AgNR-on-CD samples used in this study were fabricated in Dr. Zhao's group at the University of Georgia using the OAD method, as described in Chapter 6. In the present study, the inclined AgNRs were deposited on a commercial (MAM-A Mitsui) 700 MB Gold CD-R, which was approximately 150 mm in diameter with a track pitch (grating period) of 1.5 μm [118,119]. The Au film coated on the CD gratings was reported to be 50 nm in thickness [118]. Prior to the AgNR deposition, the thin polycarbonate protective coating was removed by immersing the CD into concentrated nitric acid and rinsing the CD with deionized water. Then the CD was dried and loaded onto the substrate holder in the deposition chamber of an electron-beam evaporation system. Similarly as described in Chapter 6, a deposition source of 99.999% pure Ag pellets was positioned right below the center of the CD. The chamber was evacuated to a pressure of about 5×10^{-3} Pa and the CD substrate was rotated manually by controlling a motor to form an angle of 86^{o} in between the surface normal of the CD substrate and the deposition vapor direction. The OAD results in aligned AgNRs downwards tilting to the deposition source.

Since the CD grating has the circular track, the incident vapor direction with respect to the grating direction varies at different CD locations. We are interested in two particular locations as shown in Fig. 7.1(a): Sample 1 was cut from the lower portion where the evaporated nanorods are perpendicular to the CD gratings and Sample 2 was cut from the right portion where the nanorods are parallel to the CD gratings. Figures 7.1(b) and 7.1(c) are two cartoons showing the expected morphologies of inclined AgNRs on the gratings for Samples 1 and 2, respectively. The dashed red lines depict the contours of the resulting grating structures. A full period of the effective grating can be

considered as a combination of a triangle and a rectangle for Sample 1 and as the regular rectangular grating with a wider ridge (nearly 0.9 μm) than the groove (nearly 0.6 μm) for Sample 2. Note that the ellipses representing the AgNR cross-sectional areas are intentionally dislocated to indicate the imperfect alignment of the AgNRs of Sample 2.

7.1.2 Morphology Characterization Based on SEM Images

The morphology of the AgNR-on-CD samples was characterized with SEM. Figure 7.2 presents several SEM images of the bare CD (a) and Samples 1 and 2 (b – g). From Fig. 7.2(a), a full period of the bare CD consists of a 0.9 μm ridge and a 0.6 μm groove. For each sample, three SEM images taken at different radial locations are displayed: the radius increases from locations b to d for Sample 1 and from locations e to f for Sample 2, as indicated in the top-right schematic of the CD substrate. Note that the SEM images of Sample 1 are rotated counterclockwise by 90^{o} so that AgNRs which originally tilt downwards are tilting towards right in Figs. 7.2(b) to 7.2(d). Note that due to the curvature of CD tracks, the grooves on the CD are slightly curved, although this feature is hard to distinguish in the SEM images. As can be seen from the SEM images, both samples tend to form a periodicity over large areas as predetermined by the CD grooves. For Sample 1, the surface morphologies are fairly similar for different locations, and all show periodic nanorod structures. However, there appears to be a clear radial dependent morphology for Sample 2: closer to the center of the CD, the surface is covered uniformly by AgNRs; with the increase of the radius, the periodic feature starts to show and the periodicity is more prominent at larger radii. The radial dependence can be explained by the increased shadowing effect experienced by the CD grooves with the increased radii. For locations close to the CD center, the vapor incident direction is

parallel to the groove, and there appears to have no periodicity in Fig. 7.2(e). When the radius becomes larger, the vapor direction is not parallel to the groove any more. There is a vapor component perpendicular to the groove which generates the shadowing effect in the direction normal to the groove. Such an effect enhances the periodic appearance of the AgNRs deposited on the CD gratings. This perpendicular component of incoming vapor becomes larger and larger with the increase of the radii making the period structure more prominent.

Due to this vapor component, at large radii, the major axis of the nanorods of Sample 2 tends to point slightly leftward with respect to the groove direction. This effect is presented as a red triangle in Fig. 7.2(g): the vertical vector parallel to the CD grooves indicates the normal component of the incoming vapor, the horizontal vector represents the perpendicular component of incoming vapor, and the hypotenuse is along the tilting direction of AgNRs. It should be noted that not all the AgNRs are perfect cylinders and some irregular shapes formed during growth can also be seen from the SEM images, such as needles, corrugations, and rod bifurcations. During the measurements discussed in the following sections, the laser spot was located near the centers of Samples 1 and 2, as shown in the images of Figs. 7.2(c) and 7.2(f). Similar to the previous studies [42,120], the average length, diameter, and tilting angle of AgNRs, statistically estimated over 50 AgNRs from SEM images, are L = 1200 nm, D = 100 nm, and $\beta = 70^{o}$ with respect to the substrate surface normal, respectively. More detailed discussion on the geometrical parameters of two gratings will be presented in Section 7.3 for RCWA modeling.

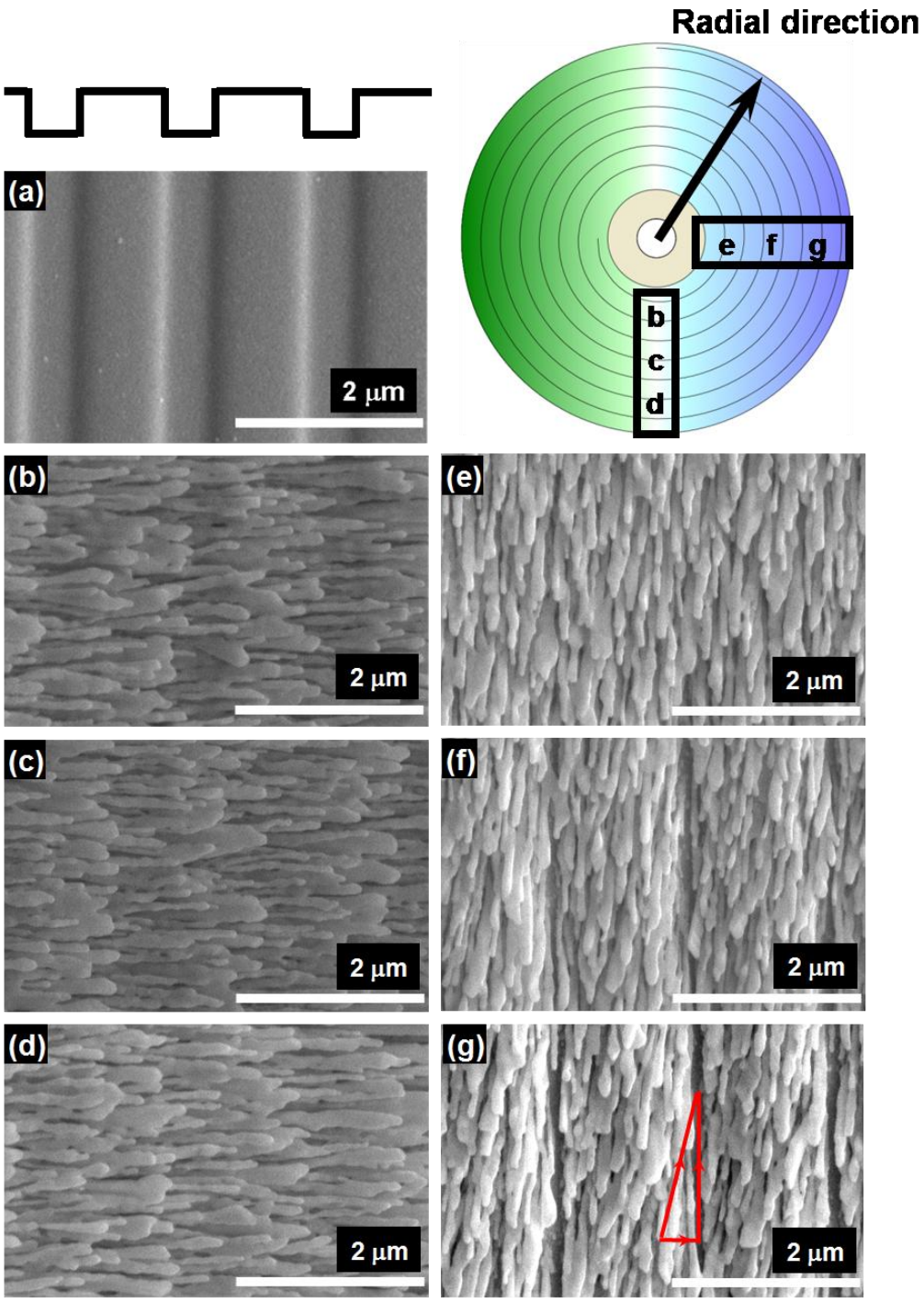

Figure 7.2 SEM images presenting the sample morphologies for sample characterization: (a) Bare CD gratings with a period around 1.5 μm; (b)–(d) Sample 1 with AgNRs perpendicular to CD gratings; (e)–(g) Sample 2 with AgNRs parallel to CD gratings. Images (b), (c), and (d) are rotated by 90 degrees (counterclockwise with respect to the original position). The red triangle in Fig. 7.2(g) indicates the directions of incoming vapor, its normal component, and the CD gratings.

7.2 Sample Loading Orientations for Measurements

To fully characterize the radiative behavior of the AgNR-Grating Hybrid structure, we have carried out three types of radiometric measurements. One is the diffraction measurement with the TAAS, another is the DHR measurement with the IS system, and the third one is the measurements of diffuse component of reflection (also with the TAAS). The pig-tailed diode laser of 635 nm was used as the light source for all the measurements. Considering the anisotropy of AgNR-on-CD samples and the effective grating profiles also has their own polarization directions, it is important to clarify the sample loading orientations for measurements.

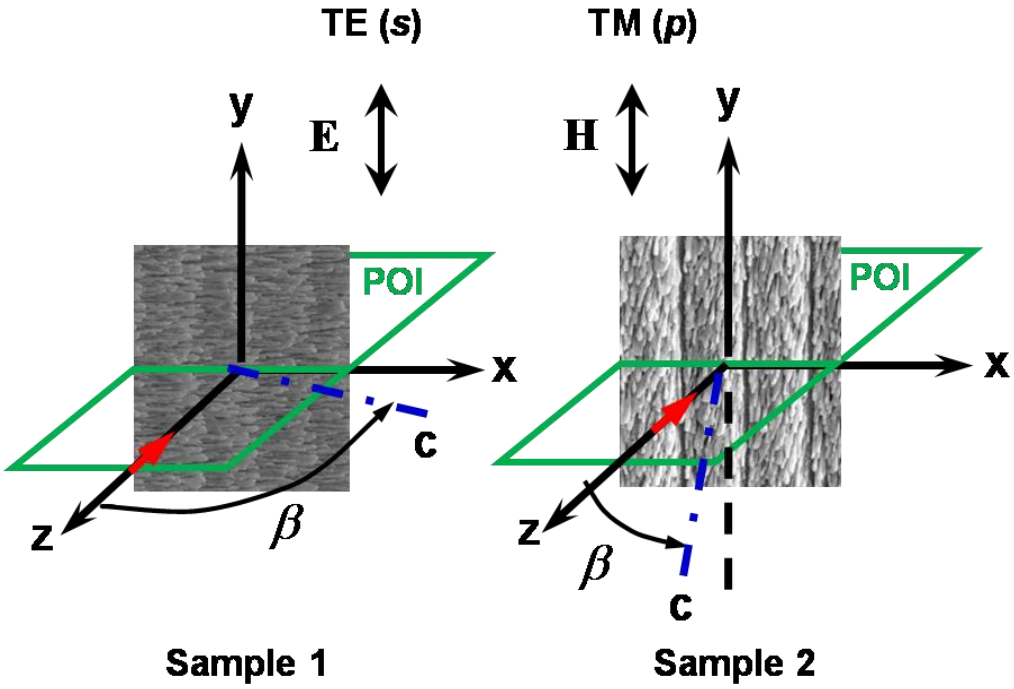

Figure 7.3 Sample loading orientations for both the diffraction and diffuse component measurements with TAAS. The CD gratings are along *y*-axis for both samples and incident light is along negative *z*-axis. The POI is the *x*-*z* plane.

In the diffraction and diffuse component measurements, the same sample loading orientations were adopted for the TAAS setup, as indicated in Fig. 7.3. For both samples,

the CD grating is along the *y*-axis. AgNRs are tilted towards positive *x*-axis for Sample 1 and negative *y*-axis for Sample 2. TE (*s* polarization) or TM (*p* polarization) waves correspond to the electric or magnetic field being vertically polarized along the *y*-axis, which is perpendicular to the POI (the *x*-*z* plane). Recall that polarization decoupling occurs at an anisotropic interface (Chapter 2) when the optical axis either lies in the POI or is perpendicular to it [53]; hence, using the sample loading orientations described above, for Sample 1 with its optical axis (along the rod axial direction) lying in the POI, TE (or TM) incidence generates the ordinary (or extraordinary) wave propagation inside the AgNR array only; while for Sample 2, whose optical axis is neither within the POI nor perpendicular to it (lying in the *y*-*z* plane), ordinary and extraordinary waves are coupled and pure *s* and *p* polarizations do not exist. Some assumptions will be introduced in the theoretical modeling section to reduce the difficulties of simulating such complex coupling cases.

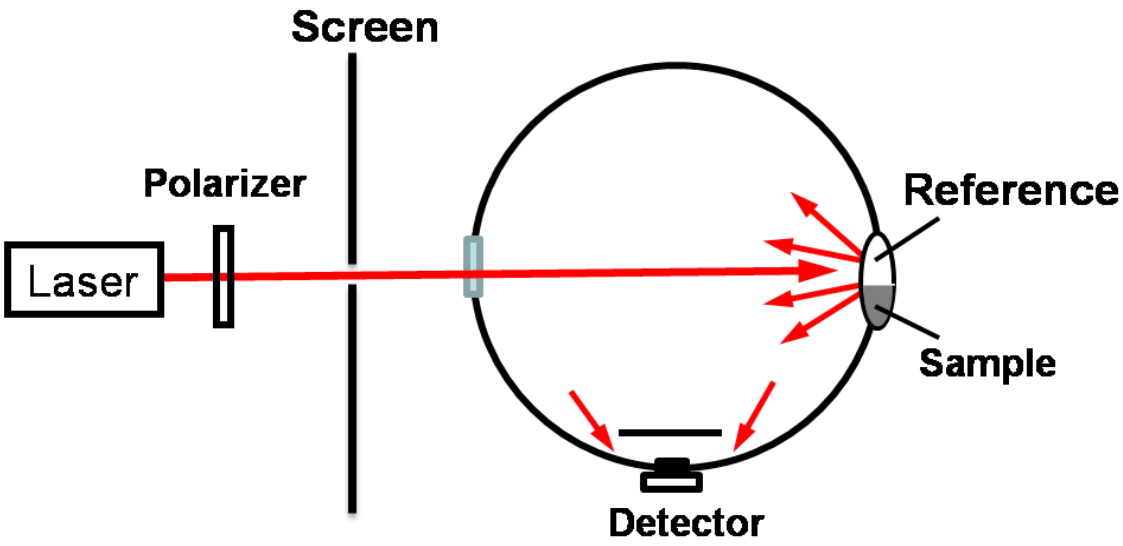

Figure 7.4 IS setup with back-mount configuration for DHR measurements of the AgNR-on-CD samples.

Figure 7.4 presents the IS setup for the DHR measurements of the AgNR-on-CD samples with the IS system, in which the back-mount configuration was used for both samples to reach the maximal symmetry [93]. Both the sample and reference were loaded on the back port and covered the port half by half (up and down), as indicated in Fig. 7.4. In general, there is no polarization-dependence for isotropic samples at normal incidence; however, the oblique orientation of AgNRs gives rise of the sample anisotropy even at normal (or near normal) incidence. Therefore, a polarizer was positioned before the IS to produce linearly polarized incident light with either TE or TM polarization.

7.3 Theoretical Modeling

7.3.1 Determination of the Effective Optical Constants

The AgNR array may be considered as an effectively homogenous medium when both the rod diameter and the separation between adjacent rods are much smaller than the incident wavelength. On the other hand, the oblique alignment of AgNRs makes such a medium optically anisotropic with the optical axis **c** parallel to the rods and at an angle of β with respect to the surface normal. As discussed in Section 2.3, wave propagation in uniaxial media can be characterized as ordinary and extraordinary waves corresponding to the electric field and magnetic field normal to the optical axis, respectively. A special case is the so-called primary extraordinary waves, when $\mathbf{E} \| \mathbf{c}$ holds in addition to $\mathbf{H} \perp \mathbf{c}$. Previous studies demonstrated that ordinary wave propagation in the AgNR array has a dielectric behavior while extraordinary wave propagation exhibits to a metallic behavior [44,120]. As discussed previously, the sample loading orientations used in diffraction measurements can affect the wave propagation in the AgNR array. For Sample 1with its

optical axis lying in the POI, TE incidence generates ordinary wave propagation inside the AgNR array for all diffraction orders, since the electric field is always perpendicular to the effective optical axis, which is along the rod direction. The situation is more complicated for TM incidence for Sample 1 as well as for Sample 2 which belongs to the coupling cases. The discussion will be deferred to the subsection of RCWA modeling.

The refractive indices for both dielectric and metallic behaviors can be obtained from the EMT as described in Chapter 2. Rewrite Eq. (2.4) for silver [49]:

$$\frac{\varepsilon_{\text{eff}}-1}{1+g(\varepsilon_{\text{eff}}-1)}=f\frac{\varepsilon_{\text{Ag}}-1}{1+g(\varepsilon_{\text{Ag}}-1)} \tag{7.1}$$

Note that in Eq. (7.1), air is treated as the host with $\varepsilon_{\text{air}}=1$ and AgNRs are treated as the filler. The effective dielectric function is related to the complex refractive index by $\varepsilon_{\text{eff}}=n_{\text{eff}}{}^2=\left(n+\text{i}\kappa\right)^2$. The dielectric function of Ag can be expressed with the Drude free electron model [76]:

$$\varepsilon_{\text{Ag}}\left(\omega\right)=\left(n_{\text{Ag}}+\text{i}\kappa_{\text{Ag}}\right)^2=\varepsilon_\infty-\frac{\omega_{\text{p}}^2}{\omega^2+\text{i}\gamma\omega} \tag{7.2}$$

For bulk sliver at room temperature, the parameters in the Drude model can be approximated as follows: scattering rate γ = 2.7×10^{13} rad/s, plasma frequency ω_{p} = 1.39×10^{16} rad/s, and a high-frequency constant ε_∞ = 3.4 [75]. Due to size effect of nanostructure as compared to bulk material, the scattering rate may increase significantly [121]. To take into account this size effect, we use a value of ten times bulk scattering rate or Ag from Modest or 2.7×10^{14} rad/s as a first-order approximation [83]. The factor of ten as chosen so that reasonable agreements between the IS measurements and RCWA modeling can be obtained. However, it is neither a fitting nor an optimized value for the

structure of interest. The volume filling fraction *f* is taken to be 0.4 from previous work [47]. The depolarization factor *g* depends on the geometry of the AgNRs and can be calculated using Eqs. (2.6) and (2.7) along with the geometric parameters of the AgNRs.

Using the approach described above, the effective optical constants of the AgNR array at the wavelength of 635 nm are estimated to be $n_{\text{eff}}^{\text{O}} = 1.6 + \text{i}0.011$ for ordinary waves and $n_{\text{eff}}^{\text{E}} = 0.20 + \text{i}2.9$ for primary extraordinary. It should be noted that for ordinary waves, the electric field is perpendicular to the optical axis; hence, the medium behaves like a dielectric with a refractive index of 1.6 and is slightly absorbing. When the electric field is parallel to the optical axis, the medium behaves like a metal with a large extinction coefficient of κ and a refractive index less than unity.

7.3.2 Rigorous Coupled-Wave Analysis

The diffraction properties of the two AgNR-grating hybrid structures are modeled by the RCWA in combining with the effective optical constants predicted from the EMT. The RCWA theory is widely used for diffraction analysis of periodic micro/nanostructured surfaces. It is an exact solution of Maxwell's electromagnetic equations which satisfies the principle of conservation of energy, and can provide numerical solutions of Maxwell's electromagnetic-wave equations with high accuracy by increasing the number of terms in the numerical simulations [72-74].

In this study, the RCWA calculation is performed following the method described by Moharam et al. [72] and detailed discussions of the RCWA calculation for the AgNR-grating structures can be found in Ref. [122]. Both Samples 1 and 2 are modeled as a four-medium structure, as illustrated in Fig. 7.5. The incident medium is air, denoted as Medium 1; Medium 2 is the uniaxial AgNR array with effective polarization-dependent

optical constants predicted from EMT; Medium 3 is the Au layer whose optical constants can be obtained from the tabulated data in Palik [87]; and Medium 4 is the semi-infinite CD substrate, which is made of polycarbonate and has a frequency independent refractive index of $n_{CD} = 1.6$ [123]. While the polycarbonate is semitransparent, due to its thickness, surface roughness, and close-to-air refractive index, the reflection from the interface between the CD substrate and the backside air can be neglected.

The effective grating formed by Sample 1 is modeled as a combination of triangular and rectangular profiles. To approximate the triangular profile, a full period of Sample 1 is divided into a large number of rectangular sub-layers with equal depth but varying widths, as illustrated in Fig. 7.5(a). The number of 100 sub-layers was chosen such that the result converges to within 5% relative error. For Sample 2 with rectangular profile, no sub-layer division is needed and thus few layers are used according to the number of interfaces, which is the usual approach in previous works [72]. In both cases, 161 Fourier diffraction orders are used and the relative differences between 161 versus 221 diffraction orders are less than 5%. The numerical error itself is expected to be smaller than the error arising from the approximation in the geometry and effective optical constants as discussed in the subsequent paragraphs.

Figures 7.5(b) and 7.5(c) depict the detailed geometric parameters used for RCWA calculations for Samples, respectively. For both Samples 1 and 2, the ridge and groove of the CD grating are taken as a = 900 nm, b = 600 nm, respectively; the thickness of thin Au coating is $h_{Au} = 50$ nm, and the normal film thickness of the AgNR array is calculated as $h_{AgNR} = L \times \cos\beta$, which gives 410 nm. To simply the calculation, AgNRs are omitted from the groove region since based on the average diameter and

spacing obtained from the SEM images, there should be only one nanorod deposited within the groove region. On the other hand, the RCWA modeling used here is applicable for binary layers; this implies difficulties of the RCWA modeling will rise from the inclusion of any nanorod in the groove region, which makes the grating a tertiary layer which is composed of CD polycarbonate, air, and the AgNR. Hence, the groove region of the substrate is devoid of nanorods as a layer of pure air with h_{CD} = 100 nm.

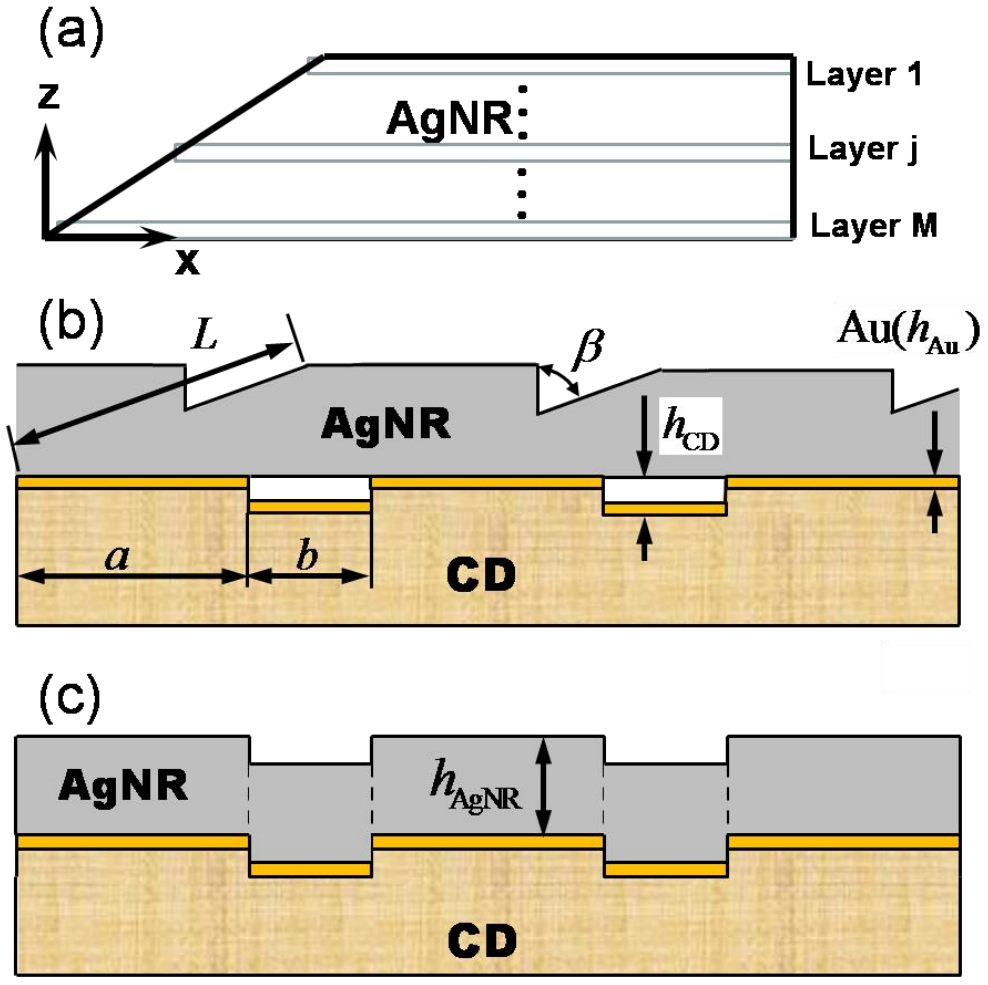

Figure 7.5 (a) Division of the triangular grating into multiple rectangular slices parallel to the substrate surface for implementation of RCWA; (b) Effective grating Sample 1; (c) Effective grating of Sample 2. Geometric parameters are L = 1200 nm, a = 900 nm, b = 600 nm, h_{Au} = 50 nm, h_{CD} = 100 nm, $\beta = 70^{o}$, and $h_{AgNR} = L \times \cos\beta$ = 410 nm.

It should be emphasized that, in the RCWA model, each medium is treated isotropic, although the effective index of AgNR layer varies with the polarization. For Sample 1 with TE wave incidence, this is satisfied because the electric field is always perpendicular to the optical axis. Hence, for TE wave incidence, only ordinary wave propagation exists inside the AgNR array with the refractive index of $n_{\text{eff}}^{\text{O}} = 1.6 + \text{i}0.011$. When the TM wave incidence is considered, both the electric field and the optical axis are in the POI defined by the *x*-*z* plane. At normal incidence, $\mathbf{E} \| \mathbf{D} \| \mathbf{c}$ and $\mathbf{H} \perp \mathbf{c}$ for the 0th order of diffraction, hence the primary extraordinary refractive index should be used. However, for other diffraction orders, both the electric field and the electric displacement have a nonzero z-component; the actual refractive index should be for the general extraordinary waves which deviate from that for the primary extraordinary waves. To simplify the complexity of implementation of RCWA for anisotropic materials, the refractive index of the AgNR layers is approximated as the primary extraordinary index of $n_{\text{eff}}^{\text{E}} = 0.20 + \text{i}2.9$ for characterization of the metallic response of extraordinary waves.

For Sample 2 with the AgNRs nearly parallel to the CD gratings, the optical axis is in the *y*-*z* plane but neither lying in the POI nor perpendicular to it. Therefore, as discussed previously, the ordinary and extraordinary waves are coupled so that both polarizations exist even though the incident wave is purely TE or TM polarized. This fundamental difficulty is dealt with by assuming that all the nanorods are parallel to the CD gratings hence they are well aligned in the *y*-axis direction with the tilting angle β modified to be 90^{o}. With this assumption, the electric field of TE wave incidence is parallel to the optical axis along the *y*-axis, resulting in the metallic characteristics of the AgNR layer with the primary extraordinary refractive index of $n_{\text{eff}}^{\text{E}} = 0.20 + \text{i}2.9$. For the

TM wave incidence, the electric field will stay within the POI, therefore always perpendicular to the optical axis with $\beta = 90^{o}$. Hence, the AgNR array of Sample 2 should exhibit dielectric characteristics with $n_{\text{eff}}^{\text{O}} = 1.6 + \text{i}0.011$ for TM incidence.

Table 7.1 Summary of the effective refractive indices predicted from the EMT (to be used in the RCWA modeling) for both Samples 1 and 2 with different polarizations.

	Sample 1		Sample 2	
	TE	TM	TE	TM
n_{eff}	1.6+i0.011	0.20+i2.9	0.20+i2.9	1.6+i0.030

Considering the actual situation of Sample 2 which is polarization coupled, as well as the entanglement and misalignment of AgNRs, a polarization mixing effect needs to be taken into account of. Following the approach described by Eq. (4.3), a combination factor of x is used to partially compensate the mixing effect. x = 0.98 is chosen so that a better overall agreement on the total reflection energy from the RCWA modeling and DHR measurements can be achieved. Calculation shows that using the above approach, there is not much appreciable change in the optical constants for TE wave incidence; however, for TM wave incidence, the extinction coefficient of Sample 2 increases to 0.3. Table 7.1 summarizes the refractive indices to be used in the RCWA analysis.

7.4 Results and Discussion

7.4.1 Diffraction Measurement

Due to the periodicity of the AgNR-on-CD samples, the diffraction becomes dominant and the intensity of individual diffraction peaks shows polarization-dependent effect since the samples are essentially anisotropic. Figure 7.6 shows the schematics of

the sample loading orientation and the diffraction distribution for diffraction measurements.

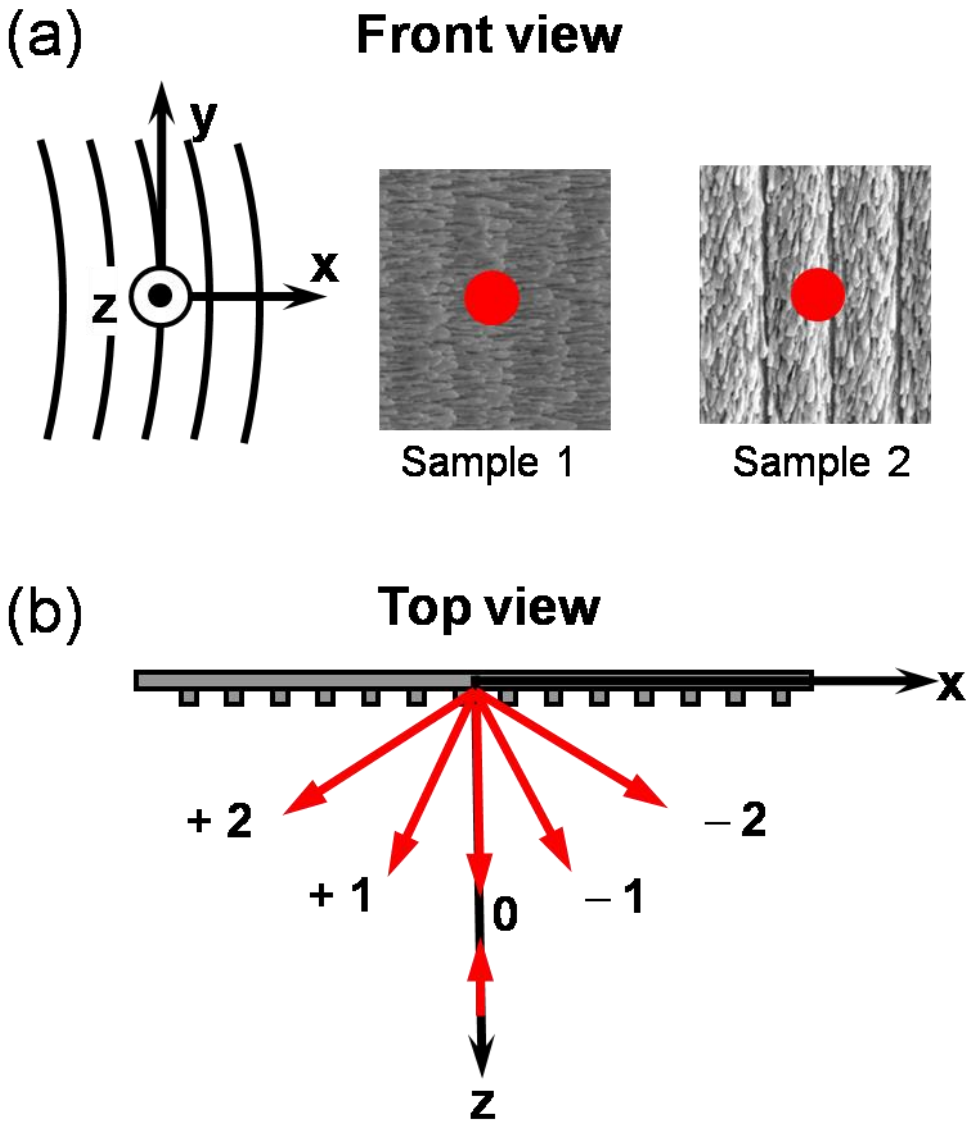

Figure 7.6 (a) Schematic of sample loading orientation: AgNRs tilting towards positive *x*-axis for Sample 1 and tilting towards negative *y*-axis for Sample 2. Incident beam is along the negative *z*-axis. TE (or TM) incidence corresponds to **E** or **H** being perpendicular to the POI (*x*-*z* plane). CD gratings are curved and along the *y*-axis; (b) The diffraction order is positive for negative *x*-axis and negative for positive *x*-axis. $m = 0$ diffraction peak is in the retroreflection direction.

The solid black lines in Fig. 7.6(a) depict the CD gratings along the *y*-axis. Since

the CD gratings have curvature, the black lines are intentionally slightly curved to illustrate this feature. The normal incidence beam, represented as a red dot in Fig. 7.6(a), is along negative *z*-axis. A TE or TM incident polarization corresponds to an incidence plane wave with the electric or magnetic field linearly polarized along the *y*-axis (i.e., perpendicular to the POI). The positive diffraction orders are defined for light diffracted towards the negative *x*-axis, as shown in Fig. 7.6(b). The relationship between diffraction angles and the grating period can be expressed by the backwards grating equation,

$$\sin\theta_m = \sin\theta_i + m\frac{\lambda}{\Lambda} \tag{7.3}$$

where λ is the incident wavelength in air, Λ is the grating period, m is the diffraction order, and θ_m is the diffraction angle (in radian), which is negative for $m < 0$. At normal incidence, the 0th order diffracted light is along the retroreflection direction, and during the TAAS measurements, the detector that collects the signal reflected from the sample blocks the incident beam. Hence, similar to the specular CNT measurement, we used the incidence angle of 4 degree to capture the 0th order diffracted power. At 635-nm normal incidence, five orders of diffraction beams can be observed as shown in Fig. 7.6(b). For $m = \pm 1$ and ± 2, the measured θ_m averaged over both positive and negative orders are approximately 25^o and 58^o. An average grating period calculated based on the measured diffraction angles and Eq. (7.3) is 1.495 μm, which is very close to that obtained from SEM images ($\Lambda = 1.5$ μm).

7.4.2 Beam Elongation Effect

Due to the curvature of CD gratings, the diffraction spot was elongated along the *y* axis and this elongation effect is more prominent for higher diffraction orders. Figure

7.7 depicts this effect with some representative photographs taken for the diffraction pattern of Sample 1. Photos of Sample 2 show similar features; hence are not presented here. These pictures were taken by placing a marked target plate in front of the sample detector holder; therefore these pictures were at equal distance from the sample center.

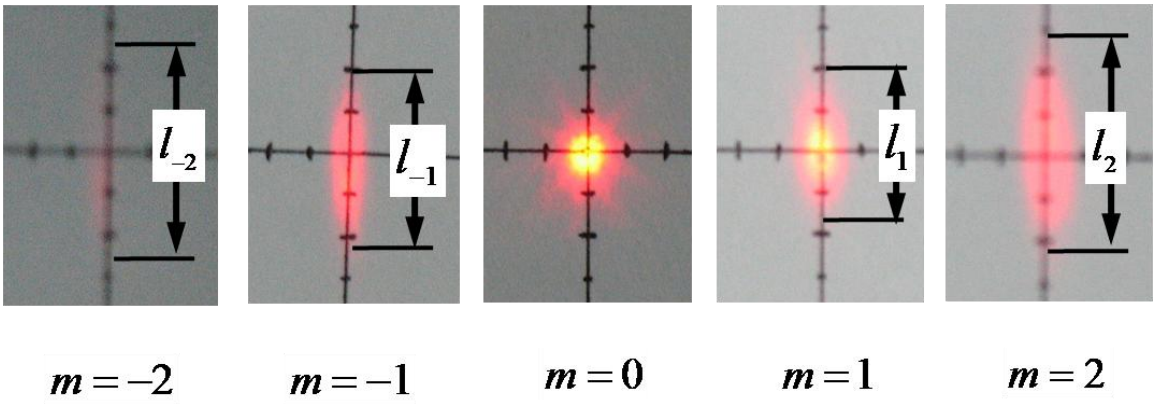

Figure 7.7 Photographs of diffraction peaks of Sample 1 with TM incidence indicating the elongation effect. The smallest dimension of the scale bar on the target plate is 5 mm.

This elongation effect may be explained by treating the illuminated area on the sample as discretized line sub-gratings rather than a continuous and curved grating. These line sub-gratings are slightly titled with respect to the *y*-axis due to the CD curvature, which is shown in Fig. 7.8(a). The different orientations of the sub-gratings result in the divergence of diffraction beam along the *y*-axis direction through propagation. The vertical dimension of the elongated diffraction beam spots (l_m for the m-th diffraction order) can be estimated by using a simple geometric relation as

$$\frac{d}{r_0} = \frac{l_m}{R_0 \theta_m} \quad \text{or} \quad l_m = \frac{dR_0}{r_0}\theta_m, \tag{7.4}$$

where d = 2.5 mm is the diameter of the laser spot on the sample, r_0 = 40 mm is the radius of the CD gratings at the center of the laser spot, and R_0 = 510 mm is the distance between the laser spot and the target plate located in front of the sample detector holder,

which is the radius of the dashed circle showing the sample detector movement in Figs. 3.1 and 7.8(b). For m = ±1 and ±2, the lengths of elongated diffraction beam spots estimated from Eq. (7.4) are 14 and 33 mm, respectively, which roughly agree with those observed from the photographs shown in Fig. 7.7, where the distance between two adjacent marks of the scale bar on the target plate is 5 mm.

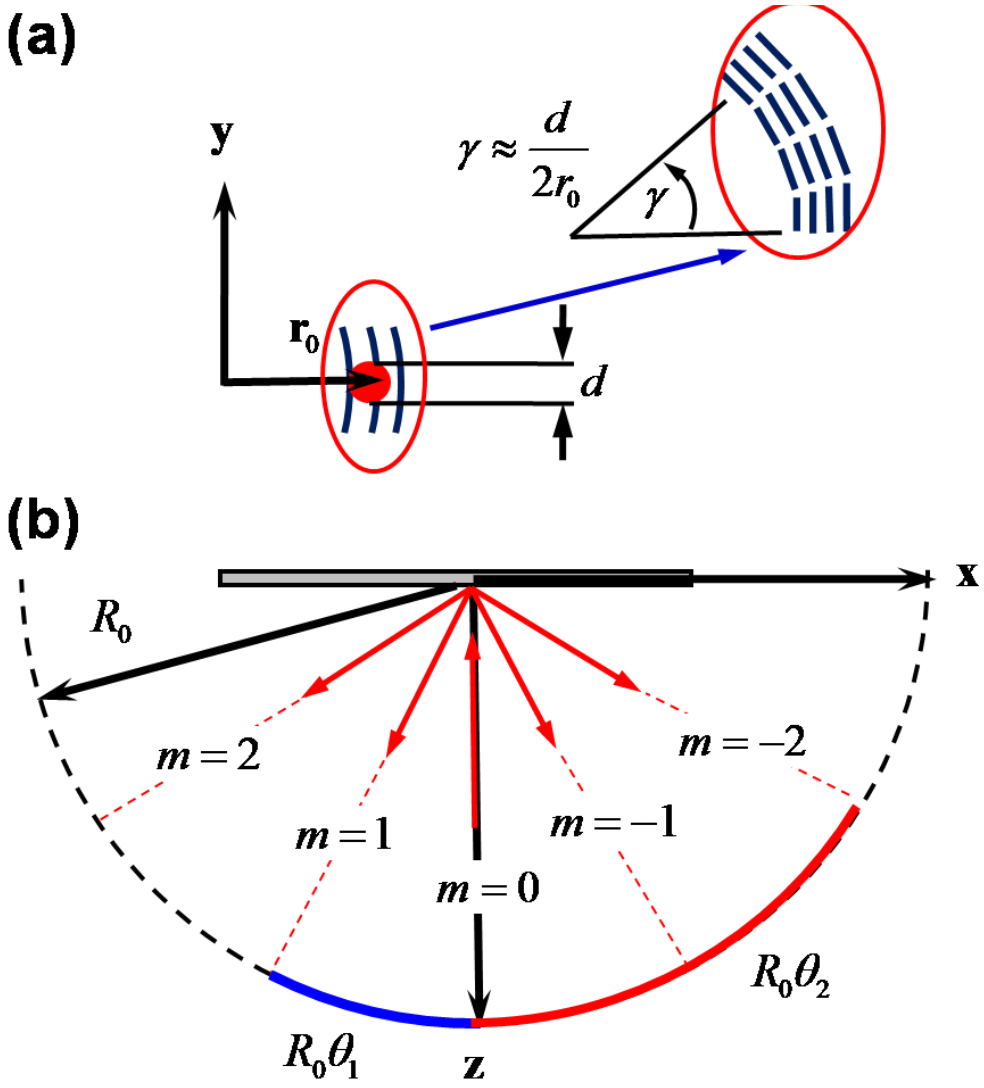

Figure 7.8 Schematic showing the beam elongation effect: (a) Approximation of curved and continuous CD gratings as discretized sub-gratings with different orientations; (b) Geometric parameters indicating the relationship between the vertical dimensions of diffraction beam spots and the diffraction angles.

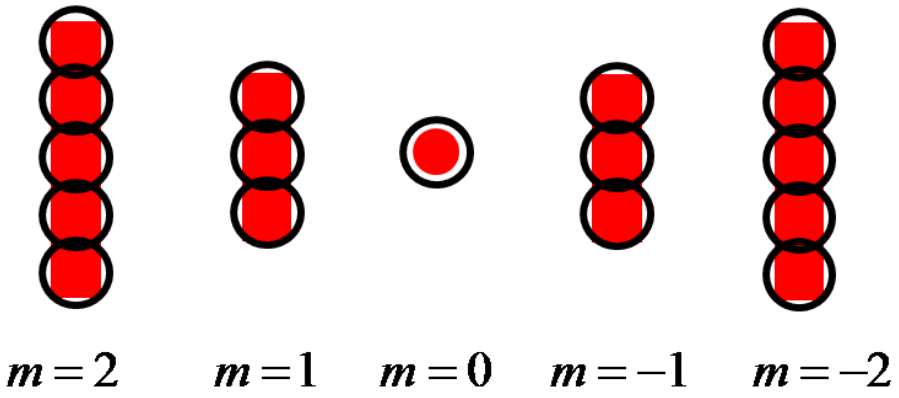

Figure 7.9 Illustration of the sample detector movement for the adding-up method.

Considering that the aperture of the sample detector is only 8 mm in diameter, which is smaller than the vertical dimensions of diffraction spots; we moved the sample detector up and down by 7.2 mm (90% of the aperture diameter) three times for $m = \pm 1$ and five times for $m = \pm 2$ to capture all the diffracted power for each diffraction order, as shown in Fig. 7.9. Because of the diffracted beam is an elongated cylinder with circular ends, the adding-up method described above should provide a good approximation of the total diffracted power. The diffraction efficiency or reflection of each diffraction peak R_{peak}, for each diffracted beam is the total diffracted power divided by the incident power.

7.4.3 Reflectance of Diffraction Peaks

Using this sample loading approach and neglecting the misalignment of nanorods, incidence of TE (or TM) polarization for Sample 1 and TM (or TE) polarization for Sample 2 should result in ordinary (or extraordinary) wave propagation inside of the AgNR array. Hence, we expect the reflectance of diffraction peaks (also called diffraction efficiency) will be higher for extraordinary waves than for ordinary waves. The reflectance results measured with the adding-up method for different orders of diffraction

(R_{peak}) at normal incidence and the wavelength of 635 nm are tabulated in Table 7.2 as well as graphed in Figs. 7.10 (Sample 1) and 7.11 (Sample 2). For ordinary waves (TE waves for Sample 1 and TM waves for Sample 2), the AgNR arrays behave as a dielectric with smaller values of R_{peak}; while for extraordinary waves (TM waves for Sample 1 and TE waves for Sample 2), the AgNR arrays are metal-like with a reflectance which is about one order of magnitude higher than that for ordinary waves. This observation agrees with previous studies of the dielectric-metal behaviors of inclined nanorods [120]. Due to the asymmetry of the combined grating profile consisting of a triangle and rectangle, the diffraction power distributions of Sample 1 for both polarizations are not symmetric with respect to $m = 0$. In general, it appears that more power is diffracted toward + orders than – orders. The trend seems to be captured by RCWA, although discrepancies exist, as can be seen from Fig. 7.10.

For Sample 2, the asymmetry of diffraction power distribution with respect to $m = 0$ is not as obvious as that of Sample 1. The measured result shows that R_{peak} values for $m = \pm 2$ of Sample 2 are fairly close: for example, $R_{peak}^{(-2)} = 0.017$ and $R_{peak}^{(+2)} = 0.015$ for TE incidence. Here, the subscript in parentheses indicates the diffraction order. Although a larger differences exist for $m = \pm 1$, such that $R_{peak}^{(-1)} = 0.23$ and $R_{peak}^{(+1)} = 0.11$, this difference is much smaller as compared to that of Sample 1, for which, $R_{peak}^{(-1)} = 0.0028$ and $R_{peak}^{(+1)} = 0.063$ for TE incidence. The larger difference for Sample 2 may be attributed to the sample non-uniformity, misalignment, and impurities.

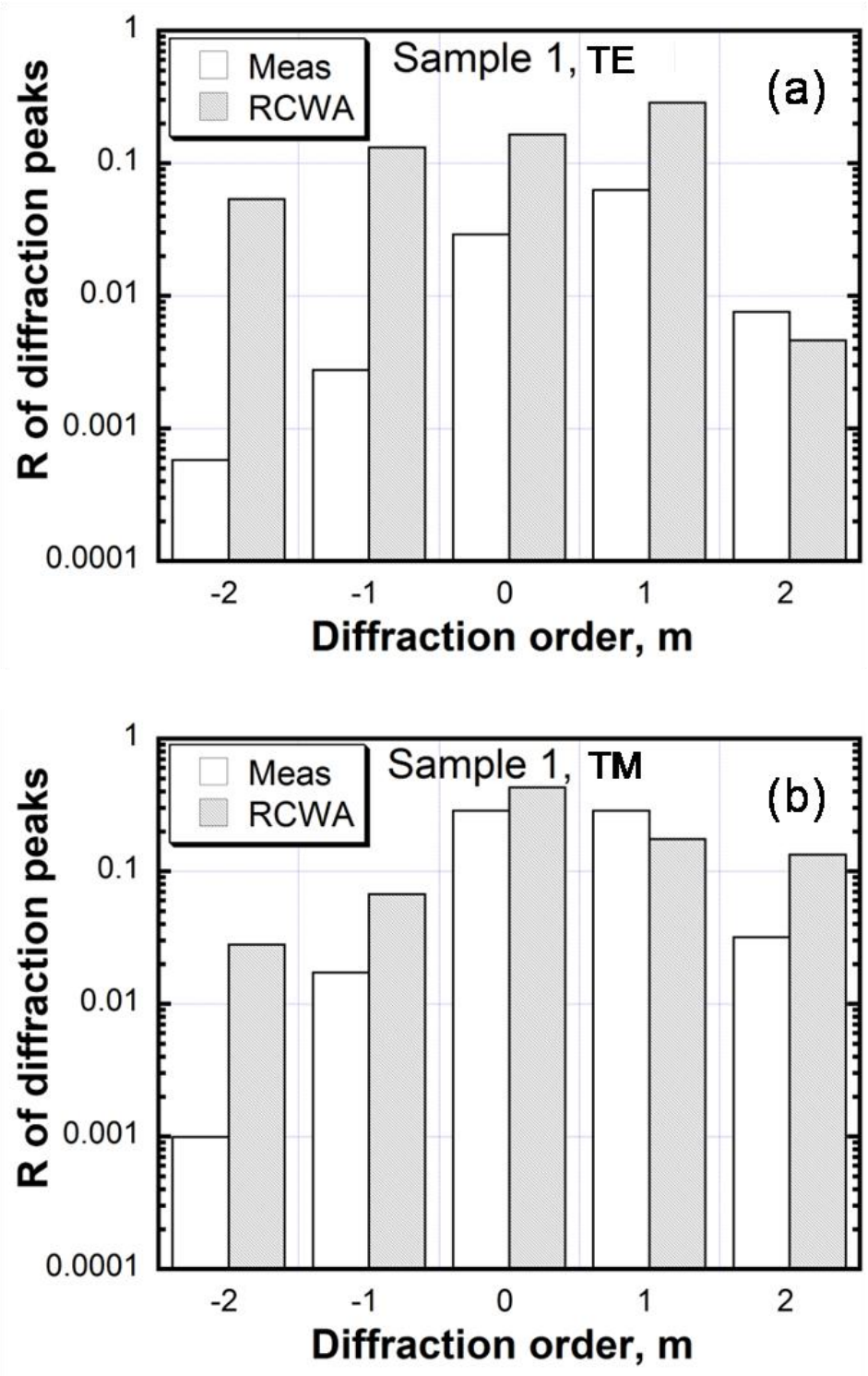

Figure 7.10 Plots of diffraction peak measurements and theoretical calculation using RCWA of Sample 1 at the 635-nm wavelength: (a) TE incidence; (b) TM incidence.

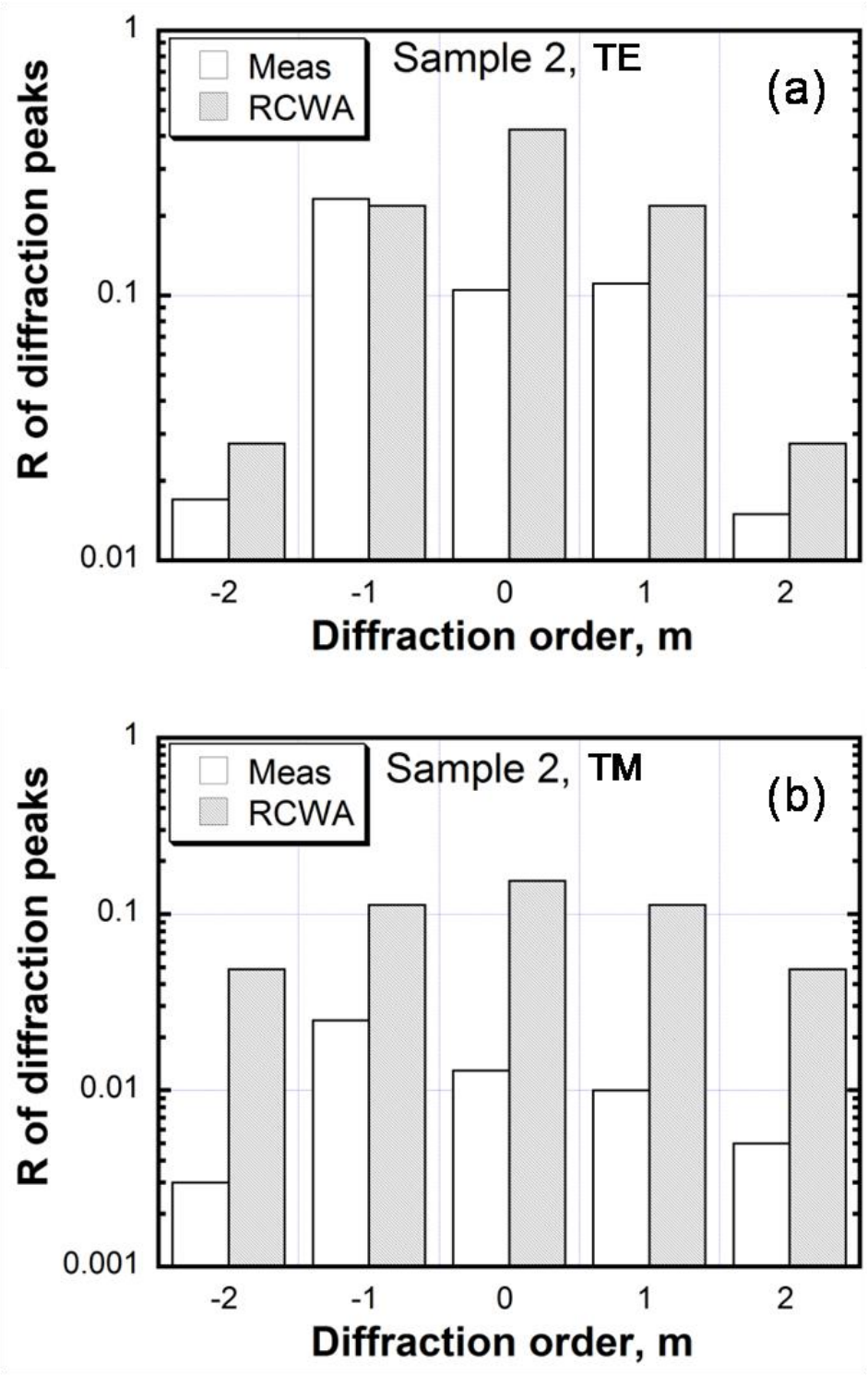

Figure 7.11 Plots of diffraction peak measurements and theoretical calculation using RCWA of Sample 2 at the 635-nm wavelength: (a) TE incidence; (b) TM incidence.

On the other hand, since the RCWA model for Sample 2 uses a rectangular geometry, the predicted diffraction efficiencies are symmetric as shown in Fig. 7.11. The trend of calculation results agrees reasonably well with that of the diffraction measurements by neglecting the asymmetries of measurement results caused by experimental uncertainties and sample non-uniformity as mentioned early. Further, the assumption of $\beta = 90^{o}$, used in the RCWA modeling for Sample 2 in order to decouple the polarizations, might cause the predicted trend to deviate more from the measurement. Detailed values of R_{peak} for both samples with individual orders are listed in Table 7.2 for direct comparisons.

Table 7.2 Reflectance of diffraction peaks from TAAS measurements for both Samples 1 and 2 with different polarizations and diffraction orders.

R_{peak}	Sample 1		Sample 2	
	TE	TM	TE	TM
$m = -2$	0.0006	0.001	0.017	0.003
$m = -1$	0.0028	0.017	0.232	0.025
$m = 0$	0.029	0.287	0.105	0.013
$m = +1$	0.063	0.287	0.111	0.010
$m = +2$	0.0076	0.032	0.015	0.005

Considering the assumptions and simplifications on both the geometric structures and the anisotropic optical constants obtained from the EMT, the overall agreement between the RCWA and the diffraction measurements seems to be satisfactory. Here, we are interested in the trends of diffracted power distribution rather than the absolute values of the magnitudes of individual diffraction orders. As discussed earlier, probably the best

agreement between the RCWA and the measurement should exist for Sample 1 with TE incidence. For all other cases, strictly speaking, the AgNR array cannot be treated as an isotropic medium. It may be interesting to consider the sum of all the diffracted power between the RCWA model and the diffraction measurements. However, the results show that the RCWA models always give a higher reflectance. This is because scattering is not considered in the RCWA model. Hence, the sum of all reflectance values for all five diffraction orders predicted by RCWA should represent the situation where scattering is neglected or the directional-hemispherical reflectance. This is verified by measuring R_{dh} as discussed in the following section.

7.4.4 DHR and the Scattering Effect

The values of R_{dh} measured with an IS incorporated with a monochromator at 635 nm are listed in Table 7.3 and compared with $R_{sum} = \sum_{m=0,\pm1,\pm2} R_{peak}^{(m)}$ which is defined as the summation of diffraction peak reflectance for all five orders and can be obtained from the RCWA modeling. It can be seen that the measured R_{dh} values agree well with those predicted by the RCWA modeling. Generally speaking, the measured R_{dh} is less than the calculated R_{sum}, except for Sample 1 with TM wave incidence. The lower IS measurement results may be caused by the signal loss from the entrance and back ports of the IS. While the reason for higher IS measurement results of Sample 1 with TM incidence might be due to the assumption used in the RCWA calculation which does not consider the sample anisotropy. From Table 7.3, the largest difference is less than 12% (TE wave incidence for Sample 1). This may be due to the dielectric nature and the difficulties in choosing proper scattering rate in the EMT. Considering the assumptions

used in the model which neglect the effects of geometry, anisotropy, and coupling, as well as the uncertainties in the IS measurement which is estimated to be 15% within 95% confidence level, the agreement is very good. Note again that the metallic behavior gives a much higher DHR than the dielectric behavior. The AgNR grating allows the switch between dielectric and metallic behaviors for individual polarizations by changing the orientations of the nanorods.

Table 7.3 Comparison of reflectance obtained from measurements and model prediction. The generalized specularity and effective roughness of Samples 1 and 2 are also listed.

	Sample 1		Sample 2	
	TE	TM	TE	TM
R_{sum} from RCWA	0.64	0.84	0.92	0.48
R_{dh} from IS	0.57	0.86	0.86	0.46
R_{sum} from TAAS	0.10	0.62	0.48	0.056
Generalized specularity	0.18	0.76	0.56	0.12
σ [nm]	66	29	38	73

The RCWA modeling is valid for smooth surfaces only since it does not take into account the scattering caused by surface roughness or volume inhomogeneity of the AgNR array. Note that R_{sum} measured with TAAS include only the diffracted component, while the R_{dh} measured with the IS include both the diffracted and diffuse components. Hence, the difference between R_{sum} and R_{dh} can be used to estimate the effective roughness factor σ, which approximates both surface scattering due to surface roughness and volume scattering due to inhomogeneous dielectric functions in the medium using the simple exponential relation [71,82]

$$R_{\text{sum}} / R_{\text{dh}} = \exp\left[-16\pi^2\sigma^2 \cos^2(\theta_{\text{i}}) / \lambda^2\right] \tag{7.5}$$

The ratio presented in Eq. (7.5) may be considered as a generalized specularity [76]. At 635-nm wavelength and normal incidence, σ calculated from Eq. (7.5) based on measured reflectance values is approximately 70 nm for ordinary and 33 nm for extraordinary (averaged over two samples). These values are on the same order of the average diameter of the nanorods and appear to be reasonable from the first-order approximation. For extraordinary waves when the AgNR array has a metallic behavior, the radiation penetration depth is very small and surface roughness may dominate the scattering. On the other hand, additional scattering may occur due to the bulk inhomogeneity, giving rise to an increase in σ and a reduction in the generalized specularity. Kassam and Hodgkinson [112] also pointed out the polarization-dependent roughness of a thin film consisting of columnar structures. The use of the generalized specularity model in Eq. (7.5) presents a simply way to separate the diffraction and diffuse components using an effective roughness. The R_{sum} values measured with TAAS are also presented in Table 7.3 along with the effective roughness and specularity parameters.

In order to better analyze the scattering feature, the diffuse components of both samples were further characterized with TAAS by measuring the out-of-plane BRDFs along various scattering directions [89]. The results are plotted in Fig. 7.12 at normal incidence for both samples and polarizations. The measurements were performed for five fixed azimuthal angles (φ = 0°, 45°, 90°, 135°, and 180°) and for θ_{r} from 5° to 80° at an increment of 5°. Here, φ = 0° and 180° correspond to in-plane measurements (solid black dots and hollow red diamonds), hence, the BRDF plots are discontinuous to exclude the

contribution from diffraction peaks. The removed BRDFs correspond to θ_r= 25°, 30°, and 35° which are affected by the ±1 diffraction orders and θ_r = 55°, 60°, and 65° which are affected by the ±2 diffraction orders. However, relatively larger BRDFs can still be observed when θ_r is close to θ_m due to the peak broadening effect. Overall, the diffuse components for both samples with different polarizations show a weak dependence on the azimuthal angle, as depicted by the nearly flat distributions of BRDFs in Fig. 7.12, which indicates the isotropic feature of scattering for both samples. Based on Fig. 7.12, Sample 2 tends to be more isotropic with the variation of BRDF magnitudes is from 0.5 to 0.15 sr^{-1}, which is smaller than that of Sample 1 from 0.5 to 0.25 sr^{-1}. The reason can be attributed to the asymmetric grating profile of Sample 1 which results in more light scattered to the direction with 90° < φ < 180°, as can be seen from Figs. 7.12(a) and 7.11(b) with higher BRDF magnitudes for cases of φ = 135° (hollow black circles) and 180° (hollow red diamonds). For samples studied in this work, the roughness is on the same order of magnitudes as the rod diameter, both of which are unconceivable to the incident wavelength. Therefore, the periodic distribution of scattering intensity due to diffraction from columnar rods (in nanometer scale) [112] were not observed for both AgNR-on-CD samples. Rather, the diffraction peaks captured in TAAS measurements were caused by the CD features (in micrometer scale). Some of the features in the diffuse component may be attributed to anisotropic diffraction and need to be further studied. However, challenges exist in how to quantitatively distinguish bulk scattering from surface scattering in this hybrid micro-nanostructured system [81,112].

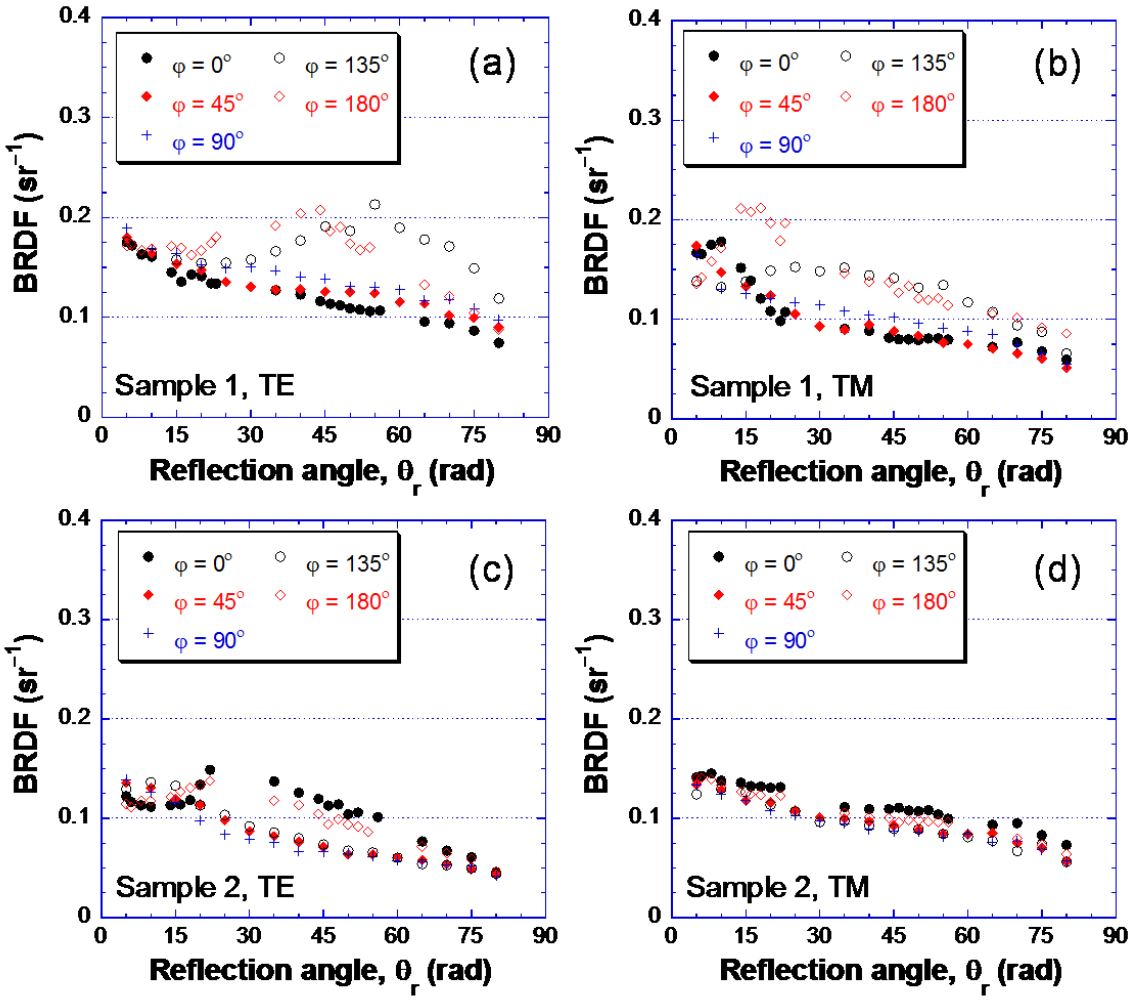

Figure 7.12 BRDF measurements with TAAS: (a) Sample 1, TE polarization; (b) Sample 1, TM polarization; (c) Sample 2, TE polarization; (d) Sample 2, TM polarization. Five azimuthal angles were measured with the polar angle varying from 3° to 80° for each φ value. Note the plots for $\varphi = 0°$ (black solid dots) and 180° (red hollow diamonds) are discontinuous at locations where θ_r is close to θ_m for $m = \pm 1$ and ± 2 due to the diffraction peaks. The measurements indicate a fairly isotropic distribution of the diffuse component (scattering).

7.5 Conclusion

In this chapter, AgNR arrays grown on CD grating templates have been fabricated using the OAD technique. These hybrid micro-nanoscale structures have inclined nanorods with high aspect ratios perpendicular or parallel to CD gratings. The AgNR

arrays are uniaxial with anisotropic responses to incident light polarizations. The sample anisotropy is demonstrated by the polarization-dependence R_{peak} and R_{dh} measured at the 635-nm wavelength. Both dielectric and metallic behaviors corresponding to ordinary and extraordinary waves are observed. The AgNR array can be considered as a homogeneous and uniaxial medium with effective ordinary and extraordinary optical constants estimated from the EMT. A simplified RCWA model is used to predict the diffraction behaviors of the hybrid gratings. Reasonable agreements on measurements and numerical modeling have been achieved. These hybrid AgNR-grating structures can be used to engineer anisotropic gratings, whose optical and radiative properties are adjustable by adapting the geometric dimensions of the nanorod array, for example, aspect ratio and volume filling fraction. Furthermore, the AgNR-grating structures can be used to control the dielectric or metallic behavior for each polarization by changing the orientations of the nanorod. This work opens up the possibilities of using AgNRs to better solutions to energy conservation and optical applications, and also provides directions to investigate the directional and polarization dependence on the optical and radiative properties of micro/nanostructures, which in turn can be used to tune the parameters of material fabrication.

CHAPTER 8

CONCLUSIONS AND FUTURE RECOMMENDATIONS

This dissertation provides an experimental and theoretical investigation of the radiative properties of nanostructured materials for potential applications in energy conversion, radiometry, optical systems, and photonic and plasmonic devices. Two types of typical 2D confined nanostructures, i.e., nano-arrays comprised of VACNTs or inclined AgNRs, were considered. Their radiative and optical properties, including the directional-hemispherical reflectance, BRDF, angle-resolved reflectance, absorptance, diffraction, and scattering, were experimentally investigated. On the other hand, arrays formed by nanorods or nanotubes have high aspect ratios, therefore effectively, they can be treated as homogenous and uniaxial media with optically anisotropic properties. The EMT and anisotropic thin-film optics modified with roughness effect are theoretically performed to elucidate the mechanisms of the radiative responses of the CNT and AgNR arrays and to determine their effective optical constants. The uniqueness and major conclusions of this dissertation are summarized below.

1. Very high absorption of VACNT samples, grown with two different growth mechanisms: tip growth and base growth, was experimentally demonstrated by measuring their BRDFs with TAAS at 635 nm and spectral DHR with an IS system from 400 to 1800 nm. The spectral peak at around 600 nm in the DHR measurements for Samples 4 to 6 is explained by the oxidation of iron catalyst particles induced by the tip-growth mechanism of the VACNT growth. The EMT calculation indicates the CNT samples are essentially opaque (i.e., the radiation penetration depth is much smaller than

the height of the VACNT) within the visible spectra and their high absorptance can be attributed to the high absorption of graphite and the low-density array configuration which results in a low refractive index close to that of air.

2. The radiative properties of three highly absorbing VACNT arrays with different surface roughnesses from specular to diffuse were investigated. The measured BRDFs of three samples exhibit specular peaks with varying magnitudes and widths, indicating the surface features are from nearly specular to highly diffuse. The comparison of BRDFs unveils that the most specular CNT array investigated in this dissertation has a higher absorptance than a commercially available specular black (Lord/Z302) while maintaining similar specularity. In addition, the near-unity (0.995–0.999) absorptance of all three CNT samples was determined by the DHR measurements in the spectral range from 400 to 1000 nm. The measured DHR of the most specular CNT sample shows some fringes due to the partially coherent interference, which also results in a colorful appearance of the specular CNT sample viewed at oblique angles. Furthermore, the specular surface allows the effective optical constants of the CNT array to be quantitatively determined by directly fitting the angle-resolved specular reflectance measured with TAAS. In addition, a Brewster angle of 44^{o} is observed from the angle-resolved reflectance measurements and further explained by the sample anisotropy. This study demonstrates that VACNT arrays can be a promising candidate for highly specular black surfaces with certain applications in blackbody cavities, absolute radiometry, and space-borne spectrometry.

3. The BRDF, DHR, angle-resolved reflectance, and scattering features of the AgNR-on-Ag film sample were experimentally characterized at both 635- and 977-nm wavelengths for both polarizations, through which, the anisotropic responses of the

AgNR samples were directly verified. Due to the large absorption of the Ag film, the three-layer anisotropic thin-film optics modified with the roughness effect is applied to the AgNR-on-Ag film sample. By fitting the specular reflectance calculated from the three-layer model with those measured using TAAS, the polarization-dependent optical constants are calculated to be n_O=1.41±0.04, κ_O=0.06±0.02, n_E=0.59±0.03, and κ_E=1.62±0.24 at 635-nm wavelength and n_O=1.58±0.05, κ_O=0.03±0.01, n_E=1.10±0.06, and κ_E=2.17±0.33 at the 977-nm wavelength. Furthermore, scattering due to both the surface roughness and bulk inhomogeneity of the inclined AgNR array exhibits somewhat polarization dependence. A simplified exponential model based on the first-order approximation is used to estimate the roughness effect, which indicates a larger roughness for ordinary waves. One possible explanation is that when ordinary wave propagates in the AgNR array, the dielectric behavior results in a larger penetration depth, hence, bulk scattering becomes more prominent for this case.

4. The anisotropic diffraction effect of a novel hybrid micro-nanoscale structure consisting of inclined AgNRs on top of CD gratings was explained by the ordinary versus extraordinary wave propagation in uniaxial media. Due to the shadowing effect induced by the OAD technique, AgNRs on two samples have different orientations with respect to the CD gratings: parallel or perpendicular, corresponding to either dielectric (ordinary) or metallic (extraordinary) behavior of the AgNR array, respectively. Hence, the dielectric or metallic behavior of the AgNR-grating structures can be easily controlled by interchanging the nanorod orientations and/or varying the incident polarizations. The anisotropic diffraction features is analyzed using a simplified RCWA model incorporated with the effective optical constants predicted by the EMT for both polarizations.

Reasonable agreements on measurements and numerical modeling have been achieved. These hybrid AgNR-grating structures hold promise in anisotropic gratings with tunable radiative properties by adapting the geometric dimensions of the nanorod array, which is superb to the bulk uniaxial media currently used for conventional anisotropic gratings.

The first step regarding the future work will be the direct implementation of the methods described in this dissertation for several on-going projects, such as the investigation of the effects from penetration depth and entanglement on the radiative properties of semitransparent CNT arrays and the potential applications of doped silicon nanowires for solar absorption.

Furthermore, it is desired to improve the scattering model. Due to the nano-array structure and bulk inhomogeneity, scattering plays a more important role for nano-arrays than the regular thin-film-like structures. A more comprehensive scattering model taking into account of both surface roughness and bulk inhomogeneity is especially critical for cases when the nano-arrays are semitransparent, such as nanorod arrays with short lengths, ordinary wave propagation, or long-wavelength incidence. Another aspect regarding the theoretical modeling would be the elevation of anisotropic thin-film optics to an advanced level including the polarization coupling. By doing so, more sample and polarization orientations can be adopted. The polarization-coupling cases may exhibit some interesting phenomena, which can be theoretically analyzed with the coupling model. In addition, the coupling model also provides a good approach to compensate the uncertainties caused by the sample and/or optical misalignment, i.e., for Orientation 1 in Chapter 6, the optical axis is slightly off from the POI due to the imperfect optical alignment. The next step will be incorporation of the anisotropic model to multilayer

thin-film optics formulation. This will produce a general model applicable for multilayer structures with one or several optically anisotropic layers.

The sample morphology and structure can significantly affect the measurement results. Hence, it will be interesting to look into the radiative properties of nanostructures with varying geometric parameters, such as length, diameter, tilting angle, shape, density (volume filling fraction), alignment, etc. In addition, sample preparation with well-controlled growth conditions and sample characterization are also important to improve the measurement repeatability and to provide accurate input parameters for theoretical modeling. Moreover, this study should be extended to include broader spectral ranges and various materials. Accurate knowledge of the optical and radiative properties of materials in the NIR and MIR spectra is crucial for understanding the physics of materials, for the control of material processing, and for thermal energy conversion. Hence, investigations on the radiative properties of CNT and AgNR arrays at longer wavelengths should be conducted in the future. In addition, nanowires/rods/tubes made of other materials, for example, doped silicon, zinc oxide, and gold, are also worthy of consideration for future research.

REFERENCES

1. Z.-P. Yang, L. Ci, J. A. Bur, S.-Y. Lin, and P. M. Ajayan, Experimental Observation of an Extremely Dark Material Made by a Low-Density Nanotube Array, *Nano Lett.*, **8**, pp. 446-451, 2008.

2. J. Lehman, A. Sanders, L. Hanssen, B. Wilthan, J. Zeng, and C. Jensen, Very Black Infrared Detector from Vertically Aligned Carbon Nanotubes and Electric-Field Poling of Lithium Tantalate, *Nano Lett.*, **10**, pp. 3261-3266, 2010.

3. R. E. Camacho, A. R. Morgan, M. C. Flores, T. A. McLeod, V. S. Kumsomboone, B. J. Mordecai, R. Bhattacharjea, W. Tong, B. K. Wagner, J. D. Flicker, S. P. Turano, and W. J. Ready, Carbon Nanotube Arrays for Photovoltaic Applications, *JOM-J. Min. Met. Mat. Soc.*, **59**, pp. 39-42, 2007.

4. K. Mizuno, J. Ishii, H. Kishida, Y. Hayamizu, S. Yasuda, D. N. Futaba, M. Yumura, and K. Hata, A Black Body Absorber from Vertically Aligned Single-Walled Carbon Nanotubes, *Proc. Natl. Acad. Sci.*, **106**, pp. 6044 - 6047, 2009.

5. B. Tian, X. Zheng, T. J. Kempa, Y. Fang, N. Yu, G. Yu, J. Huang, and C. M. Lieber, Coaxial Silicon Nanowires as Solar Cells and Nanoelectronic Power Sources, *Nature*, **449**, pp. 885-890, 2007.

6. H. Fang, X. Li, S. Song, Y. Xu, and J. Zhu, Fabrication of Slantingly-Aligned Silicon Nanowire Arrays for Solar Cell Applications, *Nanotechnology*, **19**, p. 255703, 2008.

7. L. Hu and G. Chen, Analysis of Optical Absorption in Silicon Nanowire Arrays for Photovoltaic Applications, *Nano Lett.*, **7**, pp. 3249-3252, 2007.

8. P. Avouris, M. Freitag, and V. Perebeinos, Carbon-Nanotube Photonics and Optoelectronics, *Nat. Photonics*, **2**, pp. 341-350, 2008.

9. R. Yan, D. Gargas, and P. Yang, Nanowire Photonics, *Nat. Photonics*, **3**, pp. 569-576, 2009.

10. J. Zhu, Z. Yu, G. F. Burkhard, C. M. Hsu, S. T. Connor, Y. Xu, Q. Wang, M. McGehee, S. Fan, and Y. Cui, Optical Absorption Enhancement in Amorphous Silicon Nanowire and Nanocone Arrays, *Nano Lett.*, **9**, pp. 279-282, 2009.

11. Y. Cui, Q. Wei, H. Park, and C. M. Lieber, Nanowire Nanosensors for Highly Sensitive and Selective Detection of Biological and Chemical Species, *Science*, **293**, pp. 1289-1292, 2001.

12. S. Y. Chu, Y. W. Huang, and Y. P. Zhao, Silver Nanorod Arrays as a Surface-Enhanced Raman Scattering Substrate for Foodborne Pathogenic Bacteria Detection, *Appl. Spectrosc.*, **62**, pp. 922-931, 2008.

13. X. Huang, I. H. El-Sayed, W. Qian, and M. A. El-Sayed, Cancer Cell Imaging and Photothermal Therapy in the Near-Infrared Region by Using Gold Nanorods, *J. Am. Chem. Soc.*, **128**, pp. 2115-2120, 2006.

14. E. Katz and I. Willner, Integrated Nanoparticle–Biomolecule Hybrid Systems: Synthesis, Properties, and Applications, *Angew. Chem. Int. Ed.*, **43**, pp. 6042-6108, 2004.

15. A. Ono, J. I. Kato, and S. Kawata, Subwavelength Optical Imaging through a Metallic Nanorod Array, *Phys. Rev. Lett.*, **95**, p. 267407, 2005.

16. C. J. Murphy, A. M. Gole, S. E. Hunyadi, J. W. Stone, P. N. Sisco, A. Alkilany, B. E. Kinard, and P. Hankins, Chemical Sensing and Imaging with Metallic Nanorods, *Chem. Commun.*, pp. 544-557, 2007.

17. X. Michalet, F. F. Pinaud, L. A. Bentolila, J. M. Tsay, S. Doose, J. J. Li, G. Sundaresan, A. M. Wu, S. S. Gambhir, and S. Weiss, Quantum Dots for Live Cells, in Vivo Imaging, and Diagnostics, *Science*, **307**, pp. 538-544, 2005.

18. C. W. Chen, C. H. Wang, C. C. Cheng, C. M. Wei, and Y. F. Chen, Suface Plasmon Induced Optical Anisotropy of CdSe Quantum Dots on Well-Aligned Gold Nanorods Grating, *J. Phys. Chem. C*, **115**, pp. 1520-1523, 2011.

19. X. Gao, Y. Cui, R. M. Levenson, L. W. K. Chung, and S. Nie, In Vivo Cancer Targeting and Imaging with Semiconductor Quantum Dots, *Nat. Biotechnol.*, **22**, pp. 969-976, 2004.

20. S. Link, M. B. Mohamed, and M. A. El-Sayed, Simulation of the Optical Absorption Spectra of Gold Nanorods as a Function of Their Aspect Ratio and the Effect of the Medium Dielectric Constant, *J. Phys. Chem. B*, **103**, pp. 3073-3077, 1999.

21. C. J. Orendorff, L. Gearheart, N. R. Jana, and C. J. Murphy, Aspect Ratio Dependence on Surface Enhanced Raman Scattering Using Silver and Gold Nanorod Substrates, *J. Phys. Chem.*, **8**, pp. 165-170, 2006.

22. M. J. Persky, Review of Black Surfaces for Space-Borne Infrared Systems, *Rev. Sci. Instrum.*, **70**, pp. 2193-2216, 1999.

23. K. A. Snail, D. P. Brown, J. Costantino, W. C. Shemano, C. W. Schmidt, W. F. Lynn, C. L. Seaman, and T. R. Knowles, *Optical Characterization of Black Appliques*, *Proc. SPIE*, Denver, CO, 1996.

24. D. B. Betts, F. J. J. Clarke, L. J. Cox, and J. A. Larkin, Infrared Reflection Properties of Five Types of Black Coating for Radiometric Detectors, *J. Phys. E*, **18**, pp. 689-696, 1985.

25. T. E. Wightman and F. Grum, Low-Reflectance Backing Materials for Use in Optical Radiation Measurements, *Color Res. Appl.*, **6**, pp. 139-142, 1981.

26. S. Iijima, Helical Microtubules of Graphitic Carbon, *Nature*, **354**, pp. 56-58, 1991.

27. M. Monthioux and V. L. Kuznetsov, Who Should Be Given the Credit for the Discovery of Carbon Nanotubes?, *Carbon*, **44**, pp. 1621-1623, 2006.

28. F. J. García-Vidal, J. M. Pitarke, and J. B. Pendry, Effective Medium Theory of the Optical Properties of Aligned Carbon Nanotubes, *Phys. Rev. Lett.*, **78**, pp. 4289-4292, 1997.

29. Z. M. Zhang, B. K. Tsai, and G. Machin, *Radiometric Temperature Measurements: I & II*, Academic Press, Amsterdam, 2010.

30. M. Tarasov, J. Svensson, L. Kuzmin, and E. E. B. Campbell, Carbon Nanotube Bolometers, *Appl. Phys. Lett.*, **90**, p. 163503, 2007.

31. J. H. Lehman, R. Deshpande, P. Rice, B. To, and A. C. Dillon, Carbon Multi-Walled Nanotubes Grown by HWCVD on a Pyroelectric Detector, *Infrared Phys. Technol.*, **47**, pp. 246-250, 2006.

32. J. H. Lehman, C. Engtrakul, T. Gennett, and A. C. Dillon, Single-Wall Carbon Nanotube Coating on a Pyroelectric Detector, *Appl. Opt.*, **44**, pp. 483-488, 2005.

33. Y. Murakami, E. Einarsson, T. Edamura, and S. Maruyama, Polarization Dependence of the Optical Absorption of Single-Walled Carbon Nanotubes, *Phys. Rev. Lett.*, **94**, p. 087402, 2005.

34. G. L. Peterson, S. C. Johnston, and J. Thomas, *Specular Baffles*, *Proc. SPIE*, San Diego, CA, 1992.

35. S. P. Turano, J. D. Flicker, and W. J. Ready, Nanoscale Coaxial Cables Produced from Vertically Aligned Carbon Nanotube Arrays Grown via Chemical Vapor Deposition and Coated with Indium Tin Oxide via Ion Assisted Deposition, *Carbon*, **46**, pp. 723-728, 2008.

36. S. Basu, Y.-B. Chen, and Z. M. Zhang, Microscale Radiation in Thermophotovoltaic Devices - A Review, *Int. J. Energy Res.*, **31**, pp. 689-716, 2007.

37. W. A. de Heer, W. S. Bacsa, A. Châtelain, T. Gerfin, R. Humphrey-Baker, L. Forro, and D. Ugarte, Aligned Carbon Nanotube Films: Production and Optical and Electronic Properties, *Science*, **268**, pp. 845-847, 1995.

38. T. de los Arcos, P. Oelhafen, and D. Mathys, Optical Characterization of Alignment and Effective Refractive Index in Carbon Nanotube Films, *Nanotechnology*, **18**, p. 265706, 2007.

39. Z. P. Yang, M. L. Hsieh, J. A. Bur, L. Ci, L. M. Hanssen, B. Wilthan, P. M. Ajayan, and S. Y. Lin, Experimental Observation of Extremely Weak Optical Scattering from an Interlocking Carbon Nanotube Array, *Appl. Opt.*, **50**, pp. 1850-1855, 2011.

40. F. J. García-Vidal and J. M. Pitarke, Optical Absorption and Energy-Loss Spectral of Aligned Carbon Nanotubes, *Eur. Phys. J. B*, **22**, pp. 257-265, 2001.

41. X. H. Wu, L. S. Pan, X. J. Fan, D. Xu, H. Li, and C. X. Zhang, A Semi-Analytic Method for Studying Optical Properties of Aligned Carbon Nanotubes, *Nanotechnology*, **14**, pp. 1180-1186, 2003.

42. S. B. Chaney, S. Shanmukh, R. A. Dluhy, and Y. P. Zhao, Aligned Silver Nanorod Arrays Produce High Sensitivity Surface-Enhanced Raman Spectroscopy Substrates, *Appl. Phys. Lett.*, **87**, p. 031908, 2005.

43. Y. J. Liu, H. Y. Chu, and Y. P. Zhao, Silver Nanorod Array Substrates Fabricated by Oblique Angle Deposition: Morphological, Optical, and SERS Characterizations, *J. Phys. Chem. C*, **114**, pp. 8176-8183, 2010.

44. Y. P. Zhao, S. B. Chaney, S. Shanmukh, and R. A. Dluhy, Polarized Surface Enhanced Raman and Absorbance Spectra of Aligned Silver Nanorod Arrays, *J. Phys. Chem. B*, **110**, pp. 3153-3157, 2006.

45. Z. Y. Zhang and Y. P. Zhao, Tuning the Optical Absorption Properties of Ag Nanorods by Their Topologic Shapes: A Discrete Dipole Approximation Calculation, *Appl. Phys. Lett.*, **89**, p. 023110, 2006.

46. C. Y. Lin, Y. H. Wang, J. Y. Huang, Y. J. Liu, and Y. P. Zhao, Impact of Electric Quadrupolar Coupling on the Optical Response of an Array of Nano-Objects, *J. Phys.: Condens. Matter*, **22**, p. 225301, 2010.

47. J. X. Fu, B. Park, and Y. P. Zhao, Nanorod-Mediated Surface Plasmon Resonance Sensor Based on Effective Medium Theory, *Appl. Opt.*, **48**, pp. 4637-4649, 2009.

48. G. Carr, R. Henry, N. Russell, J. Garland, and D. Tanner, Anomalous Far-Infrared Absorption in Random Small-Particle Composites, *Phys. Rev. B*, **24**, pp. 777-786, 1981.

49. G. B. Smith, Effective Medium Theory and Angular Dispersion of Optical Constants in Films with Oblique Columnar Structure, *Opt. Commun.*, **71**, pp. 279-284, 1989.

50. H. Bao and X. L. Ruan, Optical Absorption Enhancement in Disordered Vertical Silicon Nanowire Arrays for Photovoltaic Applications, *Opt. Lett.*, **35**, pp. 3378-3380, 2010.

51. G. B. Smith, Theory of Angular Selective Transmittance in Oblique Columnar Thin Films Containing Metal and Voids, *Appl. Opt.*, **29**, pp. 3685-3693, 1990.

52. A. Mendoza-Galván, G. Martinez, and J. L. Martinez, Effective Dielectric Function Modeling of Inhomogeneous and Anisotropic Silver Films, *Physica A*, **207**, pp. 365-371, 1994.

53. A. Knoesen, M. G. Moharam, and T. K. Gaylord, Electromagnetic Propagation at Interfaces and in Waveguides in Uniaxial Crystals, *Appl. Phys. B-Lasers O*, **38**, pp. 171-178, 1985.

54. J. Pendry, A. Holden, D. Robbins, and W. Stewart, Magnetism from Conductors and Enhanced Nonlinear Phenomena, *IEEE Trans. Microw. Theory Tech.*, **47**, pp. 2075-2084, 1999.

55. Y. J. Jen, C. H. Chen, and C. W. Yu, Deposited Metamaterial Thin Film with Negative Refractive Index and Permeability in the Visible Regime, *Opt. Lett.*, **36**, pp. 1014-1016, 2011.

56. Y. J. Jen, A. Lakhtakia, C. W. Yu, and C. T. Lin, Vapor-Deposited Thin Films with Negative Real Refractive Index in the Visible Regime, *Opt. Express,* **17**, pp. 7784-7789, 2009.

57. L. Menon, W. T. Lu, A. L. Friedman, S. P. Bennett, D. Heiman, and S. Sridhar, Negative Index Metamaterials Based on Metal-Dielectric Nanocomposites for Imaging Applications, *Appl. Phys. Lett.*, **93**, p. 123117, 2008.

58. K. S. Lee and M. A. El-Sayed, Gold and Silver Nanoparticles in Sensing and Imaging: Sensitivity of Plasmon Response to Size, Shape, and Metal Composition, *J. Phys. Chem. B*, **110**, pp. 19220-19225, 2006.

59. W. Ni, X. Kou, Z. Yang, and J. Wang, Tailoring Longitudinal Surface Plasmon Wavelengths, Scattering and Absorption Cross Sections of Gold Nanorods, *ACS Nano*, **2**, pp. 677-686, 2008.

60. B. Pietrobon, M. McEachran, and V. Kitaev, Synthesis of Size-Controlled Faceted Pentagonal Silver Nanorods with Tunable Plasmonic Properties and Self-Assembly of These Nanorods, *ACS Nano*, **3**, pp. 21-26, 2008.

61. A. L. Pyayt, B. Wiley, Y. Xia, A. Chen, and L. Dalton, Integration of Photonic and Silver Nanowire Plasmonic Waveguides, *Nat. Nanotechnol.*, **3**, pp. 660-665, 2008.

62. K. M. Byun, S. J. Kim, and D. Kim, Design Study of Highly Sensitive Nanowire-Enhanced Surface Plasmon Resonance Biosensors Using Rigorous Coupled Wave Analysis, *Opt. Express*, **13**, pp. 3737–3742, 2005.

63. K. M. Byun, S. J. Yoon, D. Kim, and S. J. Kim, Experimental Study of Sensitivity Enhancement in Surface Plasmon Resonance Biosensors by Use of Periodic Metallic Nanowires, *Opt. Lett.*, **32**, pp. 1902-1904, 2007.

64. T. Zentgraf, S. Zhang, R. F. Oulton, and X. Zhang, Ultranarrow Coupling-Induced Transparency Bands in Hybrid Plasmonic Systems, *Phys. Rev. B*, **80**, p. 195415, 2009.

65. X. Guo, M. Qiu, J. Bao, B. J. Wiley, Q. Yang, X. Zhang, Y. Ma, H. Yu, and L. Tong, Direct Coupling of Plasmonic and Photonic Nanowires for Hybrid Nanophotonic Components and Circuits, *Nano Lett.*, **9**, pp. 4515-4519, 2009.

66. V. A. Podolskiy, A. K. Sarychev, E. E. Narimanov, and V. M. Shalaev, Resonant Light Interaction with Plasmonic Nanowire Systems, *J. Opt. A: Pure Appl. Op.*, **7**, pp. S32-S37, 2005.

67. D. B. Geohegan, A. A. Puretzky, I. N. Ivanov, S. Jesse, G. Eres, and J. Y. Howe, In Situ Growth Rate Measurements and Length Control During Chemical Vapor Deposition of Vertically Aligned Multiwall Carbon Nanotubes, *Appl. Phys. Lett.*, **83**, pp. 1851-1853, 2003.

68. R. U. Datla, K. Stock, A. C. Parr, C. C. Hoyt, P. J. Miller, and P. V. Foukal, Characterization of an Absolute Cryogenic Radiometer as a Standard Detector for Radiant-Power Measurements, *Appl. Opt.*, **31**, pp. 7219-7225, 1992.

69. X. J. Wang, O. S. Adewuyi, L. P. Wang, B. A. Cola, and Z. M. Zhang, *Reflectance Measurements for Black Absorbers Made of Vertically Aligned Carbon Nanotubes*, *Proc. SPIE*, San Diego, CA, 2010.

70. X. J. Wang, J. D. Flicker, B. J. Lee, W. J. Ready, and Z. M. Zhang, Visible and Near-Infrared Radiative Properties of Vertically Aligned Multi-Walled Carbon Nanotubes, *Nanotechnology*, **20**, p. 215704, 2009.

71. X. J. Wang, L. P. Wang, O. S. Adewuyi, B. A. Cola, and Z. M. Zhang, Highly Specular Carbon Nanotube Absorbers, *Appl. Phys. Lett.*, **97**, p. 163116, 2010.

72. M. G. Moharam, E. B. Grann, D. A. Pommet, and T. K. Gaylord, Formulation for Stable and Efficient Implementation of the Rigorous Coupled-Wave Analysis of Binary Gratings, *J. Opt. Soc. Am. A*, **12**, pp. 1068-1076, 1995.

73. Y. B. Chen, B. J. Lee, and Z. M. Zhang, Infrared Radiative Properties of Submicron Metallic Slit Arrays, *J. Heat Transfer*, **130**, p. 082404, 2008.

74. B. Lee, Y. Chen, and Z. Zhang, Transmission Enhancement through Nanoscale Metallic Slit Arrays from the Visible to Mid-Infrared, *J. Comput. Theor. Nanos.*, **5**, pp. 201-213, 2008.

75. M. F. Modest, *Radiative Heat Transfer*, McGraw-Hill, New York, 1993.

76. Z. M. Zhang, *Nano/Microscale Heat Transfer*, McGraw-Hill, New York, 2007.

77. R. Siegel and J. R. Howell, *Thermal Radiation Heat Transfer* 4th ed, Taylor & Francis, New York, 2002.

78. M. Q. Brewster, *Thermal Radiative Transfer and Properties*, John Wiley & Sons, New York, 1992.

79. F. E. Nicodemus, Reflectance Nomenclature and Directional Reflectance and Emissivity, *Appl. Opt.*, **9**, pp. 1474-1475, 1970.

80. J. C. Stover, *Optical Scattering: Measurement and Analysis*, SPIE Optical Engineering Press, Bellingham, 1995.

81. C. Amra, C. Grezes-Besset, and L. Bruel, Comparison of Surface and Bulk Scattering in Optical Multilayers, *Appl. Opt.*, **32**, pp. 5492-5503, 1993.

82. Y. P. Zhao, G. C. Wang, and T. M. Lu, *Characterization of Amorphous and Crystalline Rough Surface: Principles and Applications*, Academic Press, San Diego, 2001.

83. C. F. Bohren and D. R. Huffman, *Absorption and Scattering of Light by Small Particles*, Wiley, New York, 1983.

84. G. L. Carr, S. Perkowitz, and D. B. Tanner, *Far-Infrared Properties of Inhomogeneous Materials*, in *Infrared and Millimeter Waves*, W. J. Button (ed.), Academic Press, Orlando, pp. 171-263, 1985.

85. D. A. G. Bruggeman, Dielectric Constant and Conductivity of Mixtures of Isotropic Materials, *Ann. Phys. (Leipzig)*, **24**, pp. 636-679, 1935.

86. J. C. Maxwell-Garnett, Colours in Metal Glasses and in Metallic Films, *Philos. Trans. R. Soc. Lond. A*, **203**, pp. 385-420, 1904.

87. E. D. Palik, *Handbook of Optical Constants of Solids*, Academic Press, San Diego, 1985.

88. R. Gaylord, Electromagnetic Transmission and Reflection Characteristics of Anisotropic Multilayered Structures, *J. Opt. Soc. Am. A*, **4**, pp. 1720-1740, 1987.

89. Y. J. Shen, Q. Z. Zhu, and Z. M. Zhang, A Scatterometer for Measuring the Bidirectional Reflectance and Transmittance of Semiconductor Wafers with Rough Surfaces, *Rev. Sci. Instrum.*, **74**, pp. 4885-4892, 2003.

90. H. J. Lee and Z. M. Zhang, Measurement and Modeling of the Bidirectional Reflectance of SiO_2 Coated Si Surfaces, *Int. J. Thermophys.*, **27**, pp. 820-839, 2006.

91. H. J. Lee, A. C. Bryson, and Z. M. Zhang, Measurement and Modeling of the Emittance of Silicon Wafers with Anisotropic Roughness, *Int. J. Thermophys.*, **28**, pp. 918-933, 2007.

92. L. M. Hanssen, Integrating-Sphere System and Method for Absolute Measurement of Transmittance, Reflectance, and Absorptance of Specular Samples, *Appl. Opt.*, **40**, pp. 3196-3204, 2001.

93. L. M. Hanssen and K. A. Snail, *Integrating Spheres for Mid-and Near-Infrared Reflection Spectroscopy*, in *Handbook of Vibrational Spectroscopy*, J. M. Chalmers and P. R. Griffiths (eds.), Wiley, New York, 2002.

94. L. M. Hanssen, Effects of Restricting the Detector Field of View when Using Integrating Spheres, *Appl. Opt.*, **28**, pp. 2097-2103, 1989.

95. B. J. Lee, Z. M. Zhang, E. A. Early, D. P. Dewitt, and B. K. Tsai, Modeling Radiative Properties of Silicon with Coatings and Comparison with Reflectance Measurements, *J. Thermophys. Heat Transfer*, **19**, pp. 558-565, 2005.

96. M. S. Dresselhaus, G. Dresselhaus, and P. Avouris, *Carbon Nanotubes: Synthesis, Structure, Properties, and Applications*, Springer-Verlag, New York, 2001.

97. P. M. Ajayan, Nanotubes from Carbon, *Chem. Rev.*, **99**, pp. 1787-1800, 1999.

98. P. M. Ajayan and T. W. Ebbesen, Nanometre-Size Tubes of Carbon, *Rep. Prog. Phys.*, **60**, pp. 1025-1062, 1997.

99. T. W. Ebbesen and P. M. Ajayan, Large-Scale Synthesis of Carbon Nanotubes, *Nature*, **358**, pp. 220-222, 1992.

100. S. P. Turano and J. Ready, Chemical Vapor Deposition Synthesis of Self-Aligned Carbon Nanotube Arrays, *J. Electron. Mater.*, **35**, pp. 192-194, 2006.

101. R. T. K. Baker, Catalytic Growth of Carbon Filaments, *Carbon*, **27**, pp. 315-323, 1989.

102. K. Liu, P. Liu, K. Jiang, and S. Fan, Effect of Carbon Deposits on the Reactor Wall during the Growth of Multi-Walled Carbon Nanotube Arrays, *Carbon*, **45**, pp. 2379-2387, 2007.

103. H. J. Lee, Y. B. Chen, and Z. M. Zhang, Directional Radiative Properties of Anisotropic Rough Silicon and Gold Surfaces, *Int. J. Heat Mass Transfer*, **49**, pp. 4482-4495, 2006.

104. Q. H. Li, B. J. Lee, Z. M. Zhang, and D. W. Allen, Light Scattering of Semitransparent Sintered Polytetrafluoroethylene Films, *J. Biomed. Opt.*, **13**, p. 054064, 2008.

105. J. Xu and T. S. Fisher, Enhancement of Thermal Interface Materials with Carbon Nanotube Arrays, *Int. J. Heat Mass Transfer*, **49**, pp. 1658-1666, 2006.

106. Z. M. Zhang, R. U. Datla, S. R. Lorentz, and H. C. Tang, Thermal Modeling of Absolute Cryogenic Radiometers, *J. Heat Transfer*, **116**, pp. 993-998, 1994.

107. M. Bedewy, E. R. Meshot, H. Guo, E. A. Verploegen, W. Lu, and A. J. Hart, Collective Mechanism for the Evolution and Self-Termination of Vertically Aligned Carbon Nanotube Growth, *J. Phys. Chem. C*, **113**, pp. 20576-20582, 2009.

108. P. Yeh, *Optical Waves in Layered Media*, Wiley, New York, 1988.

109. C. G. Malone, B. I. Choi, M. I. Flik, and E. G. Cravalho, Spectral Emissivity of Optically Anisotropic Solid Media, *J. Heat Transfer*, **115**, pp. 1021-1028, 1993.

110. H. Y. Chu, Y. W. Huang, and Y. P. Zhao, Silver Nanorod Arrays as a Surface-Enhanced Raman Scattering Substrate for Foodborne Pathogenic Bacteria Detection, *Appl. Spectrosc.*, **62**, pp. 922-931, 2008.

111. D. K. Gramotnev and S. I. Bozhevolnyi, Plasmonics Beyond the Diffraction Limit, *Nat. Photonics*, **4**, pp. 83-91, 2010.

112. S. Kassam, I. J. Hodgkinson, Q. H. Wu, and S. C. Cloughley, Light Scattering from Thin Films with an Oblique Columnar Structure and with Granular Inclusions, *J. Opt. Soc. Am. A*, **12**, pp. 2009-2021, 1995.

113. X. J. Wang, A. M. Haider, J. L. Abell, Y. P. Zhao, and Z. M. Zhang, Anisotropic Diffraction from Inclined Silver Nanorod Arrays on Grating Templates, *submitted to Nanoscale and Microscale Thermophys. Eng.*, 2011.

114. L. Abelmann and C. Lodder, Oblique Evaporation and Surface Diffusion, *Thin Solid Films*, **305**, pp. 1-21, 1997.

115. M. Bloemer, T. Ferrell, M. Buncick, and R. Warmack, Optical Properties of Submicrometer-Size Silver Needles, *Phys. Rev. B*, **37**, pp. 8015-8021, 1988.

116. Y. J. Shen, Z. M. Zhang, B. K. Tsai, and D. P. DeWitt, Bidirectional Reflectance Distribution Function of Rough Silicon Wafers, *Int. J. Thermophys.*, **22**, pp. 1311-1326, 2001.

117. D. E. Aspnes, E. Kinsbron, and D. D. Bacon, Optical Properties of Au: Sample Effects, *Phys. Rev. B*, **21**, pp. 3290-3299, 1980.

118. H. Cho, M. A. Parameswaran, and H. Z. Yu, Fabrication of Microsensors Using Unmodified Office Inkjet Printers, *Sensor Actuat. B-Chem*, **123**, pp. 749-756, 2007.

119. K. Min, Y. Huh, S. Kim, R. Wijk, G. Dubbledam, and N. Maaskant, New Recordable Optical Discs with Metal Thin Film and Organic Film on Polycarbonate, *Jpn. J. Appl. Phys.*, **37**, pp. 2089-2093, 1998.

120. Y. P. Zhao, S. B. Chaney, and Z. Y. Zhang, Absorbance Spectra of Aligned Ag Nanorod Arrays Prepared by Oblique Angle Deposition, *J. Appl. Phys.*, **100**, p. 063527, 2006.

121. L. B. Scaffardi and J. O. Tocho, Size Dependence of Refractive Index of Gold Nanoparticles, *Nanotechnology*, **17**, pp. 1309-1315, 2006.

122. A. M. Haider, *Application of Rigorous Coupled-Wave Theory for Studying Radiative Properties of Micro/Nanostrucures and Silver Nanorods on Gratings*, Master Thesis, School of Mechanical Engineering, Georgia Institute of Technology, Atlanta, GA, 2011.

123. H. R. Philipp, D. G. Legrand, H. S. Cole, and Y. S. Liu, The Optical Properties of Bisphenol-A Polycarbonate, *Polym. Eng. Sci.*, **27**, pp. 1148-1155, 1987.

VITA

XIAOJIA WANG

Xiaojia Wang attended Xi'an Jiaotong University in Xi'an, Shaanxi, the People's Republic of China, and received both her Bachelor's and Master's degrees in the School of Power and Energy Engineering in July 2000 and July 2004, respectively. She came to the United States of America in August 2007 to pursue her Doctoral degree in the George W. Woodruff School of Mechanical Engineering at the Georgia Institute of Technology. Her research interests include fundamentals of nano/microscale thermal radiation, radiative properties of nanostructured materials with high aspect ratios, and their applications in energy conversion, optical and plasmonic devices, and sensing. She is a member of the American Society of Mechanical Engineers and the Woodruff School Graduate Women's group.